4-2016

Characterization of pool boiling heat transfer from porous-coating-enhanced surfaces

Suchismita Sarangi
Purdue University

Graduate School Form
30 Updated 12/26/2015

PURDUE UNIVERSITY
GRADUATE SCHOOL
Thesis/Dissertation Acceptance

This is to certify that the thesis/dissertation prepared

By SUCHISMITA SARANGI

Entitled

CHARACTERIZATION OF POOL BOILING HEAT TRANSFER FROM POROUS-COATING-ENHANCED SURFACES

For the degree of Doctor of Philosophy

Is approved by the final examining committee:

SURESH V. GARIMELLA
Chair

ECKHARD GROLL

JAYATHI MURTHY

TAKASHI HIBIKI

To the best of my knowledge and as understood by the student in the Thesis/Dissertation Agreement, Publication Delay, and Certification Disclaimer (Graduate School Form 32), this thesis/dissertation adheres to the provisions of Purdue University's "Policy of Integrity in Research" and the use of copyright material.

Approved by Major Professor(s): SURESH V. GARIMELLA

Approved by: JAY P. GORE 04/25/2016

Head of the Departmental Graduate Program Date

CHARACTERIZATION OF POOL BOILING HEAT TRANSFER FROM POROUS-COATING-ENHANCED SURFACES

A Dissertation

Submitted to the Faculty

of

Purdue University

by

Suchismita Sarangi

In Partial Fulfillment of the

Requirements for the Degree

of

Doctor of Philosophy

May 2016

Purdue University

West Lafayette, Indiana

To my parents, Sreekantha and Minakshi, and my loving husband, Shashank,

for always believing in me

ACKNOWLEDGEMENTS

I would like to thank my advisor and mentor, Prof. Suresh V. Garimella, for his support and mentorship throughout the course of my graduate studies. His constant guidance, motivation and confidence in me have been invaluable to my education and professional development. He has always been a wonderful inspiration and I am grateful to have had the opportunity to learn from him during this important period in my life. I am thankful to my committee members, Prof. Jayathi Murthy, Prof. Eckhard Groll and Prof. Takashi Hibiki, for serving as my advisory committee and for their helpful comments and suggestions towards this dissertation work. I am grateful to Dr. Justin Weibel for his invaluable input over the years, which has immensely contributed to the success of this work.

This work could not have been completed without the fabrication of sintered samples by Steve Titolo at Thermophysical Properties Research Center, the micro-CT scans provided by James Williams at IUPUI and the useful input provided by Tom Spirka for Simpleware usage.

I extend my gratitude to my lab mates, past and present, for their assistance and insightful suggestions provided at all stages of this research. Special thanks are due to Dr. Xuemei Chen and Kevin Drummond for assistance with SEM images, and to Dr. Karthik Bodla and Dr. Susmita Dash for their help and support during this period.

I thank my friends, Susmita, Carolina, Aarti, Neha, Pratikash, Sugi, Prasoon, Romila, Gaurav, Parul, Vinod and my pet Googly, who made my stay at Purdue so memorable. I am deeply indebted to my parents, Sreekantha and Minakshi, and my husband, Shashank, for their unconditional love, support and blessings, without which I would never have achieved my dreams. I am thankful to my sister, brother and my in-laws for their loving support and blessings.

TABLE OF CONTENTS

Page

Page

LIST OF TABLES

Appendix Table Page

LIST OF FIGURES

Figure Page

Figure Page

Appendix Figure

Appendix Figure Page

Appendix Figure Page

NOMENCLATURE

a_i	coefficients in the gPC response function
b	temperature intercept, °C
A	area, m^2
B_i	polynomials in the gPC response function
c_0, c_1	thermocouple constants
C	geometric constant, shape factor
c_p	specific heat capacity, J/kg·K
C_p	specific heat, J/kgK
d	particle diameter, m
d_{part}	particle diameter after sintering, m
d_{pore}	pore diameter after sintering, m
D_c	depth of microchannel
D_h	hydraulic diameter of microchannel
D_m	depth of manifold
D_{sub}	depth of substrate
f	friction factor
F	force, N/m^2

F_b buoyancy force, N/m^2

F_i inertia force, N/m^2

h heat transfer coefficient, W/m^2K

h_{av} average heat transfer coefficient, W/m^2K

h_{fg} latent heat, kJ/kg

Ja^* Jakob number

k thermal conductivity, W/m·K

K permeability, m^2

L total length of coolant flow path, μm

L_{in} length of inlet path, μm

L_m length of manifold, μm

L_{out} length of outlet path, μm

m slope of linear fit

N number of data points

Nu Nusselt number

OF objective function

P pressure, Pa

P_{in} input power, W

ΔP pressure drop, Pa

q'' heat flux, kW/m^2

r manifold ratio

R response function

R_s shunt resistance, Ω

Re Reynolds number

$S_{int,tot}$ total interfacial area of unsegmented particles, mm^2

$S_{neck,tot}$ total neck area between connected particles, mm^2

S_{int} total interfacial area of unsegmented particles per unit volume, mm^{-1}

S_{neck} total neck area between connected particles per unit volume, mm^{-1}

T temperature, K or °C

T_s surface temperature, K or °C

u velocity, m/s

U uncertainty

U_{av} average fluid velocity, m/s

V voltage, V

V_h heater voltage, V

V_{part} volume of a particle, m^3

V_{por} volume of porous coating, cm^3

V_s shunt voltage, V

W_{por} weight of porous coating, gw_1, $w_2$weight functions

x distance from surface, m

W_c width of microchannel

Greek symbols

α_i coefficients in the response function

δ coating thickness, m

Δ difference

ε	porosity
ϕ	sphericity
θ	contact angle
μ	dynamic viscosity, Ns/m^2
ξ_i	random variable
ρ	density, kg/m^3
σ_s	standard deviation
σ	surface tension, N/m
σ_{dpore}	standard deviation in pore diameter, m
ψ_i	polynomials in the gPC response function

Subscripts

0	ice point reference junction
1-8	thermocouple locations
σ	surface tension
a, b	outer thermocouple rakes
b	bubble
bath	calibration bath
c	central thermocouple
Cu	copper
d	drag
det	deterministic mean value from outer loop
f	fluid

i	number
ice	ice point reference
in	inlet
int	interface
new	new assigned value
out	outlet
p	pressure
RTD	resistance temperature detector
s	solid
sat	saturation
TC	thermocouple
tot	total
w	bottom wall
z	coordinate direction

ABSTRACT

Sarangi, Suchismita. PhD, Purdue University, May, 2016. Characterization of Pool Boiling Heat Transfer from Porous-Coating-Enhanced Surfaces. Major Professor: Suresh V. Garimella, School of Mechanical Engineering.

Development of techniques for enhancement and optimization of thermal management technologies has been a highly active area of research in recent decades in response to the rapid emergence of compact, high-power electronic systems. Immersion cooling by boiling is one of the preferred methods for high power density applications, due to its passive nature and high heat transfer coefficients obtained. Pool boiling heat transfer has been extensively studied in recent decades to understand the inherent mechanisms yielding the high heat transfer rates, as well as to further enhance the heat transfer by simple modifications or additions to existing approaches. This thesis aims to provide detailed fundamental analysis of heat transfer enhancement by surface-coating-based boiling enhancement methods and to quantitatively analyze the dependence of heat transfer performance on coating properties.

For passive systems, which cannot afford active cooling due to either form factor or other application constraints, two-phase pool boiling heat transfer provides highly effective immersion cooling. Surface enhancement techniques, such as surface coatings, may further augment the cooling efficiency of such systems. The experimental study

presented in this thesis analyzes the effects of variation of particle size on the pool boiling performance of FC-72 obtained by free-particle and sintered-coating enhancement techniques. In the free-particle technique, loose copper particles are placed on a heated copper surface, whereas in the sintered-coating technique, copper particles are sintered to the copper surface. The particle coatings provide additional vapor nucleation sites in the cavities formed at particle-surface and particle-particle contact points, thereby enhancing boiling performance over a polished surface. The boiling performance enhancement is studied for particle sizes varying from 45 - 1000 μm at a constant coating layer thickness-to-particle diameter ratio (δ/d) of approximately 4 for both techniques. High-speed flow visualizations are performed to understand the boiling patterns and bubble departure parameters that provide explanations for the trends observed in the boiling curves. The measured wall superheat is observed to be significantly lower with a sintered coating compared to the free-particle layer for any given particle size and heat flux. Performance trends with respect to particle size, however, are remarkably similar for both enhancement techniques, and an optimum particle size of ~100 μm is identified for both free particles and sintered coatings. The free-particle technique is shown to offer a straightforward method to screen the boiling enhancement trends expected from different particulate layer compositions that are intended to be subsequently fabricated by sintering.

From the experimental investigation of pool boiling from coated surfaces, it was observed that for a given surface coating, several additional parameters might affect the heat transfer performance of the surface, and the coating porosity and particle morphology did not vary independent of each other. Hence, to further understand the

effects of coating properties, pool boiling heat transfer of FC-72 is studied from coatings with independently varying coating porosities with two different particle morphologies. Surfaces are fabricated with same size particles (90-106 μm) having different morphologies, *viz*., spherical and irregular, at a constant coating layer thickness-to-particle diameter ratio (δ/d) of approximately 4, with porosities varying over a wide range (~40% - 80 %). The morphology and size of the particles affect the pore geometry, porosity, permeability, thermal conductivity, and other characteristics of the sintered coating. In turn, these characteristics impact the heat transfer coefficient and critical heat flux (CHF) during boiling. The porous structure formed by sintering is quantitatively characterized using image analysis and numerical simulation based on micro-computed tomography (μ-CT) scans to study the geometric and effective thermophysical properties of the coatings. Critical coating properties affecting the boiling performance metrics are identified, and regression analysis is employed to observe the dependence of these metrics on the coating properties. Coatings with irregular particles or lower porosity are observed to yield higher heat transfer coefficients than those with spherical particles or higher porosities. The relative strength of dependence of the heat transfer coefficient and CHF on the coating porosity, pore diameter distribution, particle diameter distribution, particle sphericity distribution, necking and interfacial areas, permeability, and thermal conductivity of the coatings are determined. The importance of high-fidelity coating characterization to understand the heat transfer behavior of coatings is demonstrated.

Plans for future work are outlined based on the current findings. Proposed additional studies include investigation of the single bubble dynamics to further the understanding of bubble behavior that influences the heat transfer performance for free-particle and

sintered-coating techniques. The quantitative regression analysis from μ-CT scans may be further extended to include a more rigorous model that employs codependence of critical inputs, to determine a predictive correlation for the boiling heat transfer performance based on coating properties.

CHAPTER 1. INTRODUCTION

The rapid development of state-of-the-art electronics devices thrives on continued performance gains with reduced package sizes. High power density electronics require advanced thermal management of the heat generation, which if uncontrolled may lead to reduced reliability, increased power consumption, and reduced duty cycle at higher temperature operation, thereby hampering the overall efficiency of the devices. This thesis studies enhancement of one of the most widely used high-performance cooling technologies, *viz.*, passive immersion cooling by nucleate boiling. In particular, the study focuses on the effects of geometric and thermophysical properties governing the behavior of these enhancement techniques to optimize heat transfer efficiency. Forced convection cooling with liquids was also studied, and a numerical analysis on optimization of manifold microchannel heat sinks is presented in Appendix A.

1.1 Effect of Particle Size on Pool Boiling Heat Transfer Enhancement

Passive immersion cooling techniques achieve high heat transfer rates by means of nucleate boiling. The high heat transfer coefficients associated with nucleate boiling of fluids provides an efficient means of heat dissipation in thermal management of nuclear

fuel rods, high density electronics, and propulsion devices [1, 2]. Many researchers have explored various methods to enhance the heat transfer coefficients and/or maximum heat dissipation provided by pool boiling [3, 4]. Effort still remains to understand the intricate heat transfer mechanisms involved in pool boiling, and to develop surface enhancement techniques for further improvement in cooling efficiency. It is also essential to develop simple and inexpensive methods for predicting the heat transfer performance for different pool boiling enhancement techniques. Furthermore, to achieve the minimum wall superheats for a given enhancement technique, it is desirable to assess the effects of surface-coating parameters on the heat transfer coefficient and critical heat flux (CHF). The size of particles used to fabricate the coatings is one of the critical factors affecting the performance of sintered coatings [5, 6]. Hence, a systematic study of pool boiling from coatings fabricated with different particle sizes, with all other coating parameters fixed, is essential to obtain the individual effect of particle size on boiling heat transfer performance.

1.2 Quantitative Dependence of Pool boiling Performance on Coating Properties

Commercially available copper powders have various manufacturing processes, leading to widely differing geometric coating properties. Apart from the particle size, other characteristic properties of the sintered coatings such as particle morphology, coating porosity, *etc*., are also significant factors affecting the boiling heat transfer performance. The morphology of the particle has a direct effect on the effective thermal conductivity and permeability of sintered porous coatings ([7-9]). The coating porosity also has a

significant effect on the effective thermophysical coating properties [10], which in turn affect the heat transfer performance of the coatings [11]. Hence, to better understand the dependence of boiling heat transfer metrics on the coating properties, it is essential to perform a comprehensive quantitative characterization of the coatings, to obtain critical coating characteristics such as pore size distribution, interfacial area, necking area, particle size, sphericity of particles, and to study their effects on the boiling performance.

1.3 Objective of Thesis

The principal objective of the present work is to further understand the fundamental aspects of pool boiling heat transfer from enhanced surfaces. The study aims to analyze the parametric effects of coating properties on pool boiling heat transfer enhancement techniques by surface coating methods, and to aid in the design of these techniques. The primary objectives of this work are presented below.

1. Study the heat transfer enhancement obtained by free-particle and sintered-coating techniques, over plain surfaces.
2. Analyze the predominant heat transfer mechanisms for both techniques, by flow visualization.
3. Observe the effects of variation of particle size on the boiling curves and CHF for both techniques.
4. Observe the qualitative effects of particle morphology and coating porosity on the boiling curves and CHF for pool boiling from surfaces coated with sintered particles.

5. Characterize the coatings based on image analysis and numerical simulations from micro-CT scans, to obtain geometric and thermophysical properties of the coatings.
6. Perform quantitative analysis to obtain the critical coating properties, and analyze the dependence of the boiling heat transfer performance metrics on these properties.
7. To demonstrate the importance of high-fidelity characterization of coatings for understanding the pool boiling heat transfer behavior of sintered particle coatings, which cannot be otherwise explained simply from bulk coating characteristics.

1.4 Organization of Thesis

The work presented in this thesis is organized into five chapters. Chapter 1 introduces the heat transfer enhancement techniques investigated in the present work. Chapter 2 reviews the relevant literature for pool boiling heat transfer enhancement techniques. Chapter 3 includes an experimental investigation of pool boiling heat transfer enhancement by a free-particle technique and sintered particle coatings, for different sizes of spherical particles. Chapter 4 discusses the quantitative effects of coating characteristics on the pool boiling heat transfer enhancement, by varying the particle morphology and coating porosity. Chapter 5 provides primary conclusions and outlines proposed future work.

Eight appendices are also provided. Appendix A presents an overview of a numerical study on optimization of manifold microchannel heat sinks for forced convection cooling.

A detailed description of the estimation of porosity of free and sintered particle coatings, and a description of the electrical power circuit for the heaters in the pool boiling test facility is provided in Appendix B. Details about the fabrication method used for sintering the test samples are included in Appendix C. An uncertainty analysis for the temperature and heat flux measurements in pool boiling experiments is provided in Appendix D. Appendix E includes visualization images showing passive surface deformation during boiling from free-particle coatings. Appendix F provides a summary of additional results on effects of particle morphology on pool boiling heat transfer enhancement, obtained during the course of this study. Appendix G contains additional images of the coatings obtained from microscope, SEM and micro-CT scans. Appendix H provides a list of equipment and components used in the experimental test facility.

CHAPTER 2. LITERATURE REVIEW

This chapter presents a detailed literature review and discussion related to pool boiling heat transfer from enhanced surfaces and image-based characterization.

2.1 Pool Boiling Heat Transfer Enhancement Techniques

Immersion cooling using phase change heat transfer is highly effective in applications requiring high-density heat removal due to its simplicity, heat dissipation efficiency, and scalability. The mechanisms by which heat is dissipated from a surface during pool boiling consist of natural convection from the heated surface to the fluid, bulk convection induced by bubble growth and detachment, and latent heat transferred from the liquid phase to vapor bubbles formed at the surface [12]. With the advent of modern, high-performance electronic and electromechanical systems that have high-energy-density electrified components, there is need for enhancement of these heat transfer mechanisms to facilitate bubble nucleation at lower superheat temperatures and increase the critical heat flux (CHF).

The rich variety of boiling heat transfer enhancement techniques that have been demonstrated in the literature attempt to either modify the surface morphology or alter

the properties of the working fluid by addition of external agents. The use of suspended nanoparticles in fluids has been widely studied for boiling performance enhancement, but with conflicting conclusions as described by Barber *et al.* [13]. Some studies have found that seeding water with a small concentration of alumina, zirconia, or silica nanoparticles enhances the thermal conductivity of the fluid, while also altering the surface wettability by roughening, thereby nearly doubling CHF [14, 15]; however, the boiling heat transfer coefficient was reduced due to the deposition of an insulating nanoparticulate layer. Other studies report CHF values nearly triple those with pure water when alumina nanoparticles were included [16], and up to 60% higher than for pure water when silica nanoparticles were introduced [17], but with negligible change in the heat transfer coefficient. Conversely, boiling of water with cationic surfactants was shown by Hestroni *et al.* [18] to enhance the heat transfer coefficient at low surfactant concentration, while decreasing it at higher concentrations, due to the associated changes in the effective surface tension and kinematic viscosity of the fluid. White *et al.* [19] studied boiling of water with zinc oxide nanoparticles to explain these contrasting characteristics. The heat transfer coefficient increased initially due to enhanced thermal properties of the nanofluid; however, after deposition of a nanoparticle layer that completely covered the surface at higher concentrations, the heat transfer coefficient was decreased due to the suppression of bubble nucleation and release from the surface by the suspended nanoparticles (as in [14, 15]).

Boiling surface modification techniques can be classified into two categories: integral surface roughness or external surface coatings/attachments. Berenson [20] studied boiling of n-pentane from roughened surfaces of nickel, copper, and Inconel. The

nucleate boiling heat transfer coefficient was increased by as much as 600% by increasing surface roughness, while the CHF was independent of surface material, roughness, and cleanliness. Kang [21] investigated boiling performance of water from stainless steel tubes of varying diameters, lengths, orientations, and roughness (15.1 - 60.9 nm), and observed that the heat transfer coefficient increased with surface roughness; the enhancement was more pronounced for vertical (230% increase) than horizontal (71% increase) tubes. The effect of surface roughness (0.027 μm to 10 μm) on pool boiling heat transfer performance was studied by Jones *et al.* [22] for water and FC-77. For FC-77, an increase in surface roughness continually increased the heat transfer coefficient by up to 210% than a baseline polished surface, whereas for water, improvement was not monotonic beyond 1.08 μm. McHale and Garimella [23] performed a study of the quantitative bubble departure characteristics from smooth and rough aluminum surfaces (0.03 μm and 5.89 μm, respectively) by high-speed flow visualizations in FC-77. Bubble departure frequency and the number of active nucleation sites were higher for the rough surface than the polished surface. While roughening the surface to provide preferential nucleation sites is an easy surface treatment technique to implement for effective heat transfer enhancement, this technique does not provide repeatable and predictable results due to ageing effects [20, 21].

Enhancement of pool boiling heat transfer by the use of external coatings and attachments, such as sintered coatings and wire meshes, has also been extensively investigated. The change in local surface morphology, by the addition of external surface enhancements, increases the number of available nucleation sites, and thus enhances performance by reducing the incipient and nucleate boiling superheats. This has proven

to be a highly effective and reliable means of enhancing the heat transfer coefficient and critical heat flux in pool boiling. You *et al.* [24] spray-coated layers of 0.3-3 μm alumina particles over a surface and studied the boiling heat transfer performance of FC-72. Compared to a smooth surface, the particle-coated surface decreased the incipience wall superheat by ~44%, decreased wall superheat at a given heat flux by ~46%, and increased CHF by ~36%. In a subsequent study, O'Connor and You [25] painted a mixture of silver flakes and epoxy over an aluminum surface to form a coating with 1 μm cavities; the incipience superheat was reduced by ~85%, the wall superheat decreased by ~70-80% at a given heat flux, and CHF was increased by ~109%. Parker and El-Genk [26, 27] studied nucleate boiling of HFE-7100 and FC-72, respectively, from porous graphite layers containing randomly interconnected microscale pores (60% porosity). For saturated HFE-7100, the heat transfer coefficient from the porous graphite was observed to be 1700% higher than that of a smooth copper surface at 10 K superheat, with the enhancement decreasing to ~60% at CHF [26]. For FC-72, the critical heat flux was observed to increase by 63% at a 48% reduced surface superheat [27]. Bergles and Chyu [28] experimentally investigated the boiling characteristics of porous metallic coatings and found an increase in heat transfer coefficient of up to 250% for water and 800% for R-113. The boiling incipience superheat was drastically reduced due to the presence of corner cavities where the particles are attached to the surface. The porous coatings provided predictable and repeatable performance [29], as opposed to the ageing effects observed for roughened surfaces [30].

Many studies have been performed to study the parametric effects of sintered coating particle size, porosity, and thickness on pool boiling performance. Sintered copper wire

screens of varying thickness, porosity, and mesh size were investigated by Li and Peterson [31] to determine their effects on boiling performance. At low heat fluxes, the heat transfer coefficient increased with coating thickness, but an optimum layer thickness was observed at higher heat fluxes that yielded a maximum heat transfer coefficient; porous coatings with higher thermal conductivity were observed to have higher heat transfer coefficients. Furthermore, a decrease in pore size caused the boiling incipience superheat to decrease, and increased the heat transfer coefficient. Nishikawa *et al.* [5] studied the effects of refrigerant boiling from different sizes and thicknesses of copper and bronze sintered powders on copper tubes. The maximum heat transfer coefficient was obtained when the coating thickness was about 4 times that of the mean particle diameter ($\delta/d = 4$), with copper powder being more effective than bronze. These trends were reasonably well-predicted with a correlation, but it was concluded that a more rigorous formulation was necessary for application to a variety of sintered surfaces. Lu and Chang [32] studied the effect of thickness, particle size, porosity, pore size distribution, and fluid properties on boiling heat transfer from sintered porous beds. It was observed that an increase in porosity, decrease in coating thickness, or increase in particle size all enhanced the CHF. A maximum enhancement in heat transfer coefficient was observed at $\delta/d = 2$; as δ/d was further increased up to 10, the heat transfer coefficient was enhanced at low heat fluxes, but reduced at higher heat fluxes. Several additional studies of the performance of sintered porous coatings have identified the existence of an optimum layer thickness. Webb [6] reported an optimum coating thickness-to-particle diameter ratio of 4 for boiling of refrigerants from sintered copper surfaces. Chien and Chang [33] found a minimum thermal resistance for sintered copper

powder layers in boiling water at an optimum coating thickness-to-particle diameter ratio of 3.85. The prediction of the optimum coating thickness was studied by Chang and You [34], and compared against experiments for boiling of FC-72 from surfaces coated with diamond particles. Based on an analysis that assumed a transient superheated liquid boundary layer to be formed above each nucleation site between successive bubble departures [35], an optimum coating thickness equal to the superheated liquid layer thickness was predicted. Using this optimum thickness as a threshold, coatings were categorized into micro-porous (below optimum) and porous (above optimum) coatings for the purposes of developing theoretical models for each scenario. A conduction-based model formulated by Ranjan *et al*. [36] considered the porous structure as analogous to extended fins, and defined an optimum thickness as the point of diminishing returns on fin effectiveness with increasing thickness. The optimum coating thickness-to-particle diameter ratio was in the range of 4-5.

As distinct from the techniques discussed above, the placement of loose copper particles on a heated surface has been recently explored as a technique for pool boiling heat transfer enhancement by Kim *et al.* [37, 38]. This free-particle technique utilizes copper particles that are not attached to the heated surface to provide additional nucleation sites during pool boiling. High-speed flow visualization revealed that preferential bubble nucleation sites were formed at the corner cavities between the free particles and the heated surface, similar to sintered surfaces, causing enhancement of pool boiling heat transfer coefficient [37]. The effects of particle size, number of particles, and fluid properties were studied. For boiling of water with a single layer of free particles, it was found that particle sizes of 3 to 6 mm provided the largest heat transfer coefficients; a

mixture of 3 mm and 6 mm particles increased the heat transfer coefficient by 115% compared to that of a polished surface. The existence of an optimum particle size was explained by nucleation theory: while larger particle/pore sizes require lower superheat for bubble incipience, smaller particles localize superheating of the liquid near the substrate. For a low surface tension fluid, FC-72 [38], microscale particles provided the greatest enhancement in heat transfer coefficient and CHF, due to the smaller cavity size at which bubble departure occurs. Increasing the number of particles placed on the surface increased heat transfer coefficient due to a larger number of active nucleation sites, but an overly large number of particles reduced CHF due to hydraulic resistance to liquid replenishment at the surface. Free particles 10 μm in diameter, with an effective coating layer thickness of 67 μm, enhanced the heat transfer coefficient by 76%, and increased CHF by 10%, compared to a polished surface.

In summary, although pool boiling from sintered surfaces has been studied extensively, the influence of a wide range of particle sizes on pool boiling performance has not been clearly established. Fabrication of sintered surfaces is time-intensive, and hence, not ideal to be used for an exploratory or optimization study. The free-particle technique investigated in this study provides a low-cost, easier to implement enhancement approach. A detailed analysis of the performance trends of free particles versus sintered coatings, and supporting flow visualizations, enables us to propose the use of the free-particle technique to estimate the expected performance trends from sintered coatings. Owing to the similarity in boiling trends observed, this information can hence be used to screen particle sizes to be fabricated by sintering, thus reducing experimental cost and effort.

2.2 Quantitative Characterization of Effect of Coating Properties

The second part of the study is based on analysis of dependence of pool boiling performance on coating properties. The sintered coatings are obtained by individually varying the particle morphology or coating porosity, while keeping other parameters (such as particle size, coating thickness) fixed. Since the morphology of the individual particles affects the post-sintering pore shape, permeability, surface roughness, and effective conductivity and diffusivity of the coating, it can be expected to significantly influence the heat transfer coefficient and CHF during boiling. Prior studies on pool boiling have not explicitly investigated the effect of particle morphology; however, several studies have explored the effects of particle morphology on effective geometric and thermophysical properties for other heat transfer applications. Chi *et al*. [7] studied the effects of shape variations on the thermal properties of coatings. Various particle shapes such as angular/polyhedral, globular/rough-textured and hollow spheres were studied for powder-based yttria-stabilized zirconia (YSZ), molybdenum, and silicon thermal-spray coatings. Different initial particle shapes and sintering conditions were used for fabrication of the coating, resulting in different pore structure and porosities. The resulting thermal conductivity and diffusivity were shown to be more dependent on pore architecture than on the porosity of the coatings. The thermal conductivity of globular/irregular particles was found to be almost twice that of the hollow spherical powder coating. Dixon *et al.* [39] studied the effect of particle morphology on the convective heat transfer at varying flow rates through packed beds with spherical, cylindrical, and hollow cylindrical particles. The different particle shapes had a

significant effect on the effective conductivity and wall heat transfer coefficient of the packed beds. Cylindrical-particle beds showed higher thermal conductivity and heat transfer coefficient compared to spherical-particle beds, while minimal difference was observed between the full and hollow cylinders. The effect of particle shape and size on flow boiling performance of porous copper microchannel heat sinks constructed from spherical and irregular-shaped particles (50 to 150 μm effective diameter) was investigated by Deng *et al.* [40]. Irregular-shaped particles of the smallest size (50-75 μm) showed the highest heat transfer coefficient, while spherical particles of the smallest particle size showed the lowest heat transfer coefficient. Lin and Hwang [9] conducted experiments to study the effect of particle morphology and sintering conditions on the permeability of sintered powders for heat pipe applications. Three different particle shapes (irregular, dendritic and spherical) were evaluated with varying compacting pressure and temperature during sintering. It was observed that gas-atomized spherical particles had the lowest porosity but the highest permeability. Permeability may be estimated by the Kozeny-Carman equation [41]:

$$K = \frac{d^3 \varepsilon^3}{C(1-\varepsilon)^2} \tag{2.2.1}$$

where C is a geometric factor depending on the particle morphology and manufacturing process. While Eq (2.2.1) dictates that a higher coating porosity would result in a higher permeability, the morphology-dependent factor C can significantly alter the permeability. To determine the properties of porous media, several studies [42, 43] have used unit-cell models or simplified analytical/semi-empirical models to evaluate the pore-scale transport characteristics, which can then be used to solve macroscale governing equations

using effective properties. A review of these methods and their applications is provided in Ref. [44]. The accuracy of such modeling is limited for porous media with a high degree of randomness and irregularities, such as sintered particle coatings. An alternative modeling approach involves direct simulation of transport within the actual porous microstructure geometry obtained using imaging techniques such as micro-computed tomography (μ-CT) [45, 46]. Tabor *et al*. [47] demonstrated a voxel-based 3D reconstruction method for generating finite-volume meshes from μ-CT data to represent the complex structure of porous media. Bodla *et al*. used μ-CT scanning to simulate the thermal conductivity, permeability, and convective heat transport characteristics of open-celled aluminum foams [48] and sintered copper particle coatings [49]. A strong dependence of the coating characteristics on the sintering conditions was demonstrated.

The present study aims to investigate the effects of geometric properties (*viz.*, particle morphology, porosity, pore size, post-sintering particle size, particle sphericity, and interfacial and necking areas per unit volume) and effective thermophysical properties including permeability and thermal conductivity on the pool boiling performance of sintered particle coatings over a wide range of porosities. The surfaces are designed and fabricated to keep pre-sintering particle size, particle material, and coating thickness constant while varying particle morphology and coating porosity to evaluate these effects. A detailed μ-CT characterization of the coating is performed to obtain the geometric properties; numerical simulations are performed on the reconstructed porous domains to obtain the effective thermophysical properties. A regression analysis is used to quantitatively evaluate sensitivities of the pool boiling heat transfer coefficient and CHF to these coating characteristics.

CHAPTER 3. EFFECT OF PARTICLE SIZE ON SURFACE COATING-BASED ENHANCEMENT OF POOL BOILING HEAT TRANSFER

This chapter describes the experimental investigation of free-particle technique and sintered particle coatings for enhancement of pool boiling heat transfer. The free-particle enhancement technique is easily implemented and can provide insight into the expected boiling performance of sintered coatings; however, experimental results are not available for pool boiling from free and fixed (sintered) particulate layers of identical composition and under identical testing conditions (*e.g.*, fluid, surface finish/material, heater size/orientation/confinement), preventing a direct comparison. In the present work, the heat transfer enhancement (in terms of incipient wall superheat, heat transfer coefficient, and CHF) of both free particles and sintered powder coatings are experimentally explored under identical conditions. Informed by the known sensitivity to particle size, and the existence of an optimal coating thickness-to-particle diameter ratio, the heat transfer performance is studied for particle sizes ranging from 45 μm – 1000 μm at a constant δ/d = 4. A qualitative assessment of the boiling patterns and bubble departure size distributions is presented via high-speed visualizations of the entire heated surface to corroborate the trends observed in the boiling curves. The parametric trends in the boiling curves are found to be similar for both free-particle and sintered-particle coatings, although the heat transfer coefficient magnitudes differ significantly. The heat transfer

mechanisms causing these similarities in parametric trends, albeit with differences in absolute performance, are explained. The material presented in this chapter is published in *International Journal of Heat and Mass Transfer* [50].

3.1 Experimental Setup and Procedure

Figure 3.1 shows a schematic diagram and photograph of the pool boiling test facility. This setup is a modified version of the test facility used by Kim *et al.* [38] for pool boiling experiments. The chamber is constructed from four polycarbonate walls sealed flush together with RTV silicone that is cured under compression with screws. The chamber walls compress a PTFE gasket and 1.2 mm-thick polycarbonate plate that seals to the heater assembly with the test surface centered in the middle of the chamber below. A polycarbonate cover plate is sealed to the top of the chamber walls by compressing another PTFE gasket, forming a 30.48 mm × 30.48 mm × 93.9 mm sealed chamber confining the working fluid on the heated surface. The transparent walls of the polycarbonate housing allow flow visualization using a high-speed camera (Fastcam Ultima APX, Photron) at frame rates ranging from 1000 – 4000 fps.

The heater assembly consists of the copper heater block embedded in an insulation casing. The copper block has a smooth 25.4 mm × 25.4 mm top surface exposed to the working fluid. This surface finish is prepared using a consistent procedure of sanding with progressively finer diamond sanding sheets (9 microns, 3 microns, and 0.1 microns) followed by metal polishing (Simichrome, Happich). This procedure results in a mirror-finish surface with roughness R_{RMS} = 20 nm, as measured by a non-contact 3D scanning

white light interferometer (NewView 6200, Zygo Corp.). Eight 0.889 mm-diameter holes on the sides of the copper block allow insertion of T-type thermocouples for temperature measurements along 3 rakes, as shown in the inset in Figure 3.1 (c). The copper is heated by 12 cartridge heaters (100 W/60 V) inserted into holes in the bottom surface of the block. The electrical circuit for power supply to the test block is shown in Appendix B. For assembly, the upper half of the copper block is inserted into a block of PEEK, a machinable, low thermal conductivity (0.28 W/m·K) thermoplastic that can withstand temperatures up to 250 °C. The polished surface protrudes above the upper PEEK surface, and aligns flush with the top surface of the polycarbonate plate. An alumina silicate ceramic casing is placed around the bottom half of the copper block as insulation that can withstand higher temperatures than the PEEK. The ceramic placed under the copper block has 12 aligned holes so as to allow the cartridge heaters to pass through into the copper. A lower PEEK casing shrouds the ceramic blocks to provide further insulation and to affix all of the components in place.

A chamfer in the PEEK block around the outer edges of the test surface creates a groove surrounding the test surface with the 1.2 mm-thick polycarbonate plate sealed to the top of the PEEK block; this groove helps in sealing the seams in the heater assembly exposed to the fluid. As shown in Figure 3.1 (b), a layer of RTV silicone sealant is first carefully placed in the groove using a syringe, and is allowed to cure for 90 minutes in an oven at 75 °C. After the silicone is cured, a layer of epoxy (E 5302 Hi Temp, Epoxylite) is applied to fill in the remaining gap. The entire facility is placed in the oven at 80 °C for 20 hours to cure the epoxy layer. The RTV silicone prevents wicking of the epoxy into the gap between the test piece and insulation, easing removal of the test piece

between successive tests. The high-viscosity paste epoxy is chosen as a sealant so that it does not seep into the pores of sintered powder test surfaces. The polycarbonate plate helps to form a smooth meniscus in the epoxy layer around the edge of the test surface, and prevents premature activation of nucleation sites at the edge prior to incipience of boiling on the surface itself.

Within the test chamber, a T-type thermocouple is sealed through the polycarbonate cover plate to measure the pool temperature during testing. A 3.175 mm-diameter stainless steel condenser tube is wound in a coil in the vapor space. During testing, a chilled 50%-50% water-glycol mixture is cycled through the stainless steel tube at a flow rate of 0.5 l/min at 15°C using a chiller (ULT-80, Neslab) to condense vapor. A 6.35 mm-diameter polyurethane tube connects the liquid pool to a vapor trap. The chiller flow rate and set-point temperature were selected to ensure that no working fluid collects in the vapor trap during the experiment (to prevent fluid loss from the chamber over time). The vapor trap is open to ambient so as to maintain the chamber at atmospheric pressure during testing.

3.1.1 Fabrication of Test Surfaces

Two different boiling enhancement techniques are investigated, *viz.*, the free-particle technique and sintered powder coatings. Spherical air-atomized copper particles of various size ranges are obtained from Alfa Aesar (44-149 μm and 0.8-2 mm) and ACuPowder International (105-250 μm). The particles are sieved into size ranges of 45-53 μm, 90-106 μm, 180-212 μm, and 850-1000 μm. The layer thickness-to-particle

diameter ratio for free particles is fixed at $\delta/d = 4.8$ (reduced to approximately $\delta/d = 4$ after densification by sintering), which has been previously observed as optimum for boiling enhancement from sintered particle coatings [6, 36].

To prepare the samples, the particles are first cleaned by soaking in acetone followed by a methanol rinse. A high-accuracy electronic scale (Voyager, Ohaus) is used to measure the weight of the particles placed on the heated surface. To fabricate a sintered sample, loose copper powder is poured into a graphite mold and leveled off to the desired height with a straight edge. The copper substrate is then gently placed on top of the copper powder. The mold, with the copper substrate, is placed into a bell jar furnace that is evacuated down to $\sim 10^{-2}$ torr (~ 1.33 Pa) over 4 hours using a mechanical pump, after which a diffusion pump is turned on to pull a high vacuum of $\sim 10^{-6}$ torr ($\sim 1.33 \times 10^{-4}$ Pa) over approximately 12 hours. The temperature is steadily ramped for 2.5 hours up to 950 °C and held at this temperature for 60 minutes (an extended time of 120 minutes was required for the 850-1000 μm particle size sample) under vacuum conditions. The assembly is then allowed to cool gradually to room temperature under vacuum ($\sim 5 \times 10^{-5}$ torr) so as to avoid oxidation, and immediately placed in an airtight container until it is tested. Figure 3.2 shows photographs of the 180-212 μm and 850-1000 μm sintered particle coatings; the coating is uniform and not oxidized after sintering. Further details about the fabrication process are included in Appendix C.

The test matrix in Table 3.1 includes the particle size, weight, porosity, and layer thickness for each sample. The weight of the particles differs for free and sintered particles because the free particles cover a larger 30.48 mm × 30.48 mm area that includes coverage of the outer epoxy layer, while the sintered particles only coat the 25.4

mm × 25.4 mm copper block surface. The porosity of the free particles is estimated by measuring the volume occupied by a known weight of copper powder, using a graduated cylinder. For the sintered coatings, a known weight of particles is sintered, and the height is measured after sintering to obtain the volume of the coating. The porosity is calculated based on the volume occupied by the known weight of particles, as described in Appendix B. Figure 3.3 shows a side view of the sintered particle coatings used for this estimate, and a top view of the free particle layer.

3.1.2 Experimental Procedure

In order to perform a test, the pool is filled with 40 ml of fluorinert liquid FC-72, which has the following thermophysical properties: T_{sat} = 56 °C, ρ = 1594 kg/m^3, $\mu = 4.3\times10^{-4}$ kg/m s, k = 0.054 W/m·K, h_{fg} = 88 kJ/kg, c_p = 1101 J/kg K, and σ = 0.010 N/m [51]. The working fluid is aggressively boiled for 2 hours prior to beginning the experiment, so as to degas the fluid and cavities on the surface. For testing using free particles, the cover plate is removed briefly, and a pre-determined quantity of the desired copper particles is introduced into the test chamber with caution to avoid scratching the test surface. The cover plate is then sealed, and the heat flux is increased in steps to obtain the boiling curve using the cartridge heaters. The pre-determined increments were small (3-4 kW/m^2) at low heat fluxes until boiling incipience, followed by larger increments (10-12 kW/m^2) during nucleate boiling, and finally reduced again (7-10 kW/m^2) when approaching CHF. The input voltage is measured across all the heaters connected in parallel. The power supplied to the heater block is monitored using a 0.01 Ω shunt resistor connected in series

with the system. Thermocouple temperature data are logged using a data acquisition system (34970A, Agilent) at 3 s intervals. Steady-state conditions are assumed to have been reached when the change in temperature versus time is less than 0.02 °C/s over 30 minutes. Once this steady-state criterion is satisfied, the temperature data collected over 120 s are time-averaged for subsequent post-processing of the actual surface heat flux and corresponding surface temperature, as described below.

To determine the heat flux and wall superheat, the temperature gradients along the three thermocouple rakes are first calculated. The temperature gradient for the central rake is calculated by linear regression of temperature measurements at junctions j_1, j_2, j_3 and j_4, and for the outer rakes by a temperature differential. The local wall temperatures are then calculated as follows:

$$\left(T_w\right)_a = T_7 + x_7\left(\frac{dT}{dx}\right)_a \;;\quad \left(T_w\right)_b = T_5 + x_5\left(\frac{dT}{dx}\right)_b \;;\quad \left(T_w\right)_c = T_1 + x_1\left(\frac{dT}{dx}\right)_c \tag{3.1.1}$$

Here, T_i denotes temperature at thermocouple location j_i as shown in Figure 3.1 (c), and x_i denotes the distance from the top surface at this thermocouple location. Assuming uniform heat transfer from the top surface of the heater block, the area-average surface temperature is calculated using the areas shown schematically in the top view in Figure 3.1 (c).

$$T_w = \frac{\left(T_w\right)_a A_a + \left(T_w\right)_b A_b + \left(T_w\right)_c A_c}{\left(A_a + A_b + A_c\right)} \tag{3.1.2}$$

The area-averaged heat flux is calculated similarly as follows:

$$q''_{tot} = -k \frac{\left(\frac{dT}{dx}\right)_a A_a + \left(\frac{dT}{dx}\right)_b A_b + \left(\frac{dT}{dx}\right)_c A_c}{\left(A_a + A_b + A_c\right)} \tag{3.1.3}$$

3.1.3 Uncertainty Analysis

The reference temperature for all thermocouple measurements is maintained by a dry-block ice-point (TRC-III, Omega). A resistance temperature detector (RTD) is used to measure the actual block temperature throughout testing, which provides higher accuracy than the thermocouples. The thermocouples are calibrated over the range of operating temperatures (40 °C to 110 °C at intervals of 10 °C) using a stable temperature bath (7103 Microbath, Fluke) that is also monitored using an RTD. A least-squares linear regression fit, offset from the NIST ITS-90 [52] higher-order polynomial T-type thermocouple standard calibration curve, was used to obtain a new calibration for the thermocouples, where any offset from 0 °C in the ice-point reference junction temperature is measured and accounted for. Uncertainties in the linear-fit parameters are obtain according to Brown *et al.* [53], and absolute temperature uncertainties are specified by the equipment manufacturers ($U_{T,ice}$ = ±0.1 °C, $U_{T,RTD}$ = ±0.1 °C and $U_{T,bath}$ = ±0.05 °C).

The uncertainties in the measured quantities may be obtained by a standard deviation-based error propagation method. This results in an absolute temperature uncertainty of ±0.23 °C. For differential temperature measurements, on account of simultaneous calibration of all thermocouples, the reduced propagated uncertainty is ±0.06 °C per the uncertainty in calibration slope, as described in [54]. At steady state, the temperature is

averaged over 40 readings; since the thermocouple locations are fixed, the random uncertainty in the axial location is assumed to be zero, while the systematic uncertainty is taken as the maximum clearance between the thermocouple bead diameter and the diameter of the tapped holes in the copper block, 40 μm. The heat flux is obtained from a linear fit to the temperature rake data; the uncertainties in the linear fit by a least-squares regression are obtained as described in [53]. The respective area-averaged surface temperature and heat flux uncertainties are approximately ±0.1 °C and ±4.5 kW/m^2 over the range of heat fluxes investigated. The detailed uncertainty analysis is presented in Appendix D.

3.2 Results and Discussion

3.2.1 Free-Particle Coating

The mechanism by which heat transfer is enhanced upon the addition of free particles during pool boiling is by creation of surface cavity geometries that are favorable for vapor nucleation [37, 38], as with other fixed enhancement coatings. However, the interactions of the particles with the surrounding liquid and departing vapor are distinct. At the initiation of boiling, individual vapor bubbles are formed within the layer of stacked free particles, which coalesce to form stable vapor columns as the heat flux is increased gradually. The actively deformable particles are displaced by the release of trapped vapor from the surface [55], as described in Appendix E. Depending on the size of particles used, as the vapor bubbles are carried upward by buoyant forces, some particles may become temporarily suspended in the liquid. Larger particles quickly settle

back into the bed, while smaller particles have a longer residence time in the fluid, giving the appearance of a more uniform suspension. It may be noted here that despite the chaotic motion of free particles during boiling, the temporal averages of the surface temperature and heat flux still reach repeatable steady-state values per the criteria established in Section 3.1.2.

The parametric effects of free-particle size on pool boiling performance are investigated with particle diameters ranging from 45 μm to 1000 μm and compared against the polished surface baseline case; layer thickness is maintained at a constant value of 4.8 particle diameters for all cases. The boiling curves obtained are shown in Figure 3.4. In comparison to the polished surface, the free particles are observed to generally enhance performance in terms of the heat transfer coefficient (*i.e.*, wall superheat is reduced at a given heat flux). A trade-off is observed between the magnitude of nucleate boiling heat transfer coefficient enhancement at low heat fluxes and the rate of increase of heat transfer coefficient with increasing heat flux as the particle size is decreased from 850-1000 μm to 45-53 μm. At low heat fluxes, larger particles create nucleation cavity geometries that allow for bubble incipience and departure at lower superheat with larger bubble diameter. As particle size decreases, the theoretical number of active nucleation sites over the same heated area increases; however, smaller particles are more easily drawn into suspension in the fluid, reducing the nucleation site density and heat transfer coefficient at the lowest heat fluxes following boiling incipience. Conversely, a decrease in particle size and dimensional coating thickness supports a higher CHF, as vapor clogging and resistance to liquid replenishment at the surface are reduced compared to the larger sizes. The trends observed in the boiling curves are a

result of these counteracting mechanisms. Figure 3.5 provides additional visual evidence of these mechanisms using images taken from high-speed flow visualizations (2000 fps) of the particulate layer for the different free particle sizes with increasing heat flux, as described below.

For the largest particle size (850-1000 μm, Figure 3.5 (a)), the particles remain settled on the surface for the entire range of heat fluxes. Due to the consistent number of nucleation sites, the boiling curve slope is constant, and the heat transfer performance is enhanced relative to the polished surface up to 30 kW/m^2. As the heat flux increases, the vapor bubbles coalesce in the static layer, impeding vapor departure and ultimately causing a crossover with the polished baseline boiling curve and a commensurately reduced CHF.

For the next lower particle size (180-212 μm, Figure 3.5 (b)), the layer is actively displaced during boiling and particles migrate along the surface due to the surrounding fluid flow patterns. Nucleate boiling performance is similar to the 850-1000 μm particle size at low heat fluxes up to the point where the boiling curves intersect with the polished surface baseline. At this heat flux, where vapor clogging had caused CHF for the 850-1000 μm particles, the deformable 180-212 μm layer does not restrict vapor departure from the surface. At this intermediate particle size, the particles are too heavy to become easily entrained into the fluid, and instead tend to build up along the chamber side walls, exposing large areas of polished copper. Over the areas where the underlying polished surface is exposed, nucleation is suppressed, and the boiling curve follows the polished surface closely. This behavior is unique to the particle size range of 180-212 μm; larger

particles tend to form a uniform static layer and smaller particles are more uniformly redistributed over the surface when entrained into the fluid.

As particle size decreases further to 90-106 μm, a trade-off is observed between lower incipience wall superheat at the onset of nucleate boiling and lower wall superheats at higher heat fluxes relative to the larger particle sizes. The onset of nucleate boiling occurs at a higher wall superheat (9.5 K for 90-106 μm particles compared to 6.8 K for 180-212 μm), and the wall superheat remains larger than that of the 180-212 μm particles for heat fluxes up to 25 kW/m^2, due to the smaller bubble departure diameter, as observed from Figure 3.5 (a-c). At higher heat fluxes the boiling curves cross, and enhanced heat transfer performance is measured for the 90-106 μm free particles. At higher heat fluxes, when the vapor bubbles begin to coalesce, smaller particle sizes give rise to smaller coalesced bubbles. These bubbles have less difficulty in displacing – and departing from – the particulate layer, leading to lower wall superheat as compared to the larger particle sizes. The difference compared to larger particles starts at heat fluxes higher than 25 kW/m^2, as similarly observed for sintered coatings by Chang and You [34]. As the boiling process becomes more vigorous at these higher heat fluxes, visualization of the smaller 90-106 μm particles (Figure 3.5 (c)) shows that nucleation sites remain active and uniform over the surface due to intermittent settling of particles, whereas nucleation was non-uniform and vapor was forced to depart through thick particulate layers for the comparatively larger 180-212 μm particles.

This trend continues as the particle size is further decreased to 45-53 μm. The nucleate boiling performance deteriorates further because the smallest particles are so easily entrained into the fluid that few remain on the surface to provide active nucleation sites.

There is not a layer of particles continually covering and impeding liquid replenishment to the surface (Figure 3.5 (d)); therefore, this smaller particle size sustains a much higher CHF of 161 kW/m^2. It may be noted here that the CHF reached by this smallest particle size considered is higher than that for the polished surface (112 kW/ m^2). This may be attributed to alteration of the surface wettability or additional capillarity effects provided by some deposition of the small particles on the surface, as is observed in the case of nanofluids [56], or to some roughening of the surface due to erosion by the motion of the suspended particles.

In summary, free particles in the size range of 90-106 μm are observed to show the best nucleate boiling performance, with a 32% reduction in the surface superheat compared to the polished surface at 112 kW/m^2 (the flux at which the polished surface reaches CHF). Free particles in the diameter range of 45-53 μm yield the maximum CHF (161 kW/m^2), 44% higher than that of a polished surface.

Comparison with previous studies on the free-particle enhancement technique using FC-72 [38] shows similar trends as observed in the present study, although quantitative differences are observed in the boiling curves due to the different coating thickness and particle size ranges considered in this study. As in the current study, the larger particles were reported to enhance the heat transfer coefficient compared to a polished surface at low heat fluxes, but with an accompanying reduction in CHF. While this occurred at a particle diameter range of 850-1000 μm in the current study, premature CHF was not observed until much larger, millimeter-sized particles in [38] due to the smaller monolayer coating thicknesses used, with commensurately lower hydraulic resistance. In both studies, a significant improvement in heat transfer coefficients throughout the

boiling curves was observed as compared to a polished surface once the free particle diameter was decreased to less than ~150 μm, and critical heat flux enhancement was observed for free particles on the order of 10s of microns in diameter (44% for 45-53 μm particles in the current study, 10% for 10 μm particles in [38]).

3.2.2 Sintered-Particle Coating

The parametric effects of sintered particle size on pool boiling enhancement are investigated with particle diameters ranging from 45 μm to 1000 μm as compared against the polished surface baseline case. The sintered coatings are prepared with a thickness of approximately 4 particle layers, as shown in Table 3.1. The boiling curves for the sintered surface are shown in Figure 3.6. All of the particle sizes investigated are observed to enhance performance compared to a polished surface, due to an increase in the number of active nucleation sites. Figure 3.7 provides visual evidence of the mechanisms affecting the parametric trends in the boiling curves using images taken from high-speed flow visualization at 2000 fps, as described below.

For the largest particle size (850-1000 μm, Figure 3.7 (a)), the wall superheat at incipience as well as nucleate boiling over the entire range of heat fluxes are reduced significantly as compared to a polished surface (shown in Figure 3.6), due to the increased number of active nucleation sites formed by the porous surface; however, coalescence and clogging of vapor bubbles in the relatively thick layer hinders bubble departure, leading to reduced CHF. For the next smaller particle size (180-212 μm, Figure 3.7 (b)), the heat transfer coefficient is enhanced, and CHF is increased. The

enhancement in heat transfer coefficient is due to the larger number of nucleation sites available at any heat flux over the same area for the smaller particles. Since smaller particles have smaller coating thickness (δ/d constant), they are able to support a higher CHF. As particle size decreases further to 90-106 μm, (Figure 3.7 (c)), the heat transfer coefficient is further enhanced due to the larger number of nucleation sites; however, the CHF is reduced. A possible reasoning for this anomalous decrease in CHF may be due to a reduction in the effective heat transfer area having a more dominant effect than reduced hydraulic resistance with a reduction in coating thickness. This is a similar mechanism of CHF reduction as found in previous studies [57], wherein for a fixed particle size, a decrease in coating thickness was observed to cause a decrease in CHF, due to a reduction in effective heat transfer area. As the particle size reduces further (45-53 μm, Figure 3.7 (d)), CHF is restored to an expected value, and the heat transfer coefficient decreases. Although the available nucleation site density increases, the small pore sizes less favorable for bubble incipience reduce the number of active nucleation sites. It should be noted that the wall superheat values are very low (< 2K) for the sintered surfaces with particle sizes from 45-212 μm, and hence the performance differences observed between these cases are small compared to the experimental uncertainty, and show less contrast than between cases for the free particles. The 90-106 μm particles show the maximum decrease in wall superheat compared to a polished surface at ~72 kW/m^2 (20.4 K to 1.3 K).

Several studies in the literature have similarly shown the effect of particle size on boiling heat transfer enhancement with sintered coatings. Chang and You [34] investigated boiling of FC-72 from a non-conductive epoxy-based porous surface, where the coating

thickness increased with particle size. The heat transfer coefficient increased with an increase in particle size from 2 μm to 20 μm, but decreased with further increases in particle size. The coating thickness for this optimum 20 μm particle case corresponded to the liquid layer thickness that was predicted to become superheated between successive bubble departures; any further increase in thickness added hydraulic resistance without any fin-effect benefit. In the present study, a similar trade-off in heat transfer coefficient with particle diameter is observed; however, the optimum particle size of 90-106 μm (at a layer thickness of 402 μm) is larger for the sintered copper particles. A similar increase compared to the predicted value was also observed by Scurlock [58], where the optimum coating thickness was 250 μm compared to the calculated superheated liquid layer thickness of 100 μm for liquid nitrogen. Chang and You [34] attributed this increased optimum thickness to the higher thermal conductivity of the plasma-sprayed aluminum particle coating. Following a similar analysis as proposed by Hsu [35], the superheated liquid layer thickness for FC-72 was estimated to be 100 μm (as in [34]); however, due to the high thermal conductivity of the current sintered copper coating as compared to the epoxy-based porous coating in [34], the observed optimum coating thickness was higher for the present coating (~400 μm).

Figure 3.8 shows a direct comparison between the boiling curves obtained for the free-particle and sintered-coating enhancement techniques. It is observed that sintered surfaces significantly outperform the free particles at any given particle size, even for the cases (850-1000 μm) where the free particles exhibit minimal particle motion during boiling. This can only be attributed to the primary morphological difference between the structures, which is the sintered neck formed between particles. This improves the

conductivity of the sintered particles, allowing the layer to enhance the effective heat transfer area (whereas the point-contact between spherical free particles limits the conductivity of the free-particle layer). Also, the fixed structure may provide additional capillary wicking of liquid to the surface. While the free particles actively deform during boiling, the sintered particles provide a stable capillary column that provides a continuous path for replenishment of bulk liquid to the heated surface. For smaller particles (approximately less that 200 μm), the free particles become suspended in the fluid during boiling, which reduces the temporal average number of particles in contact with the surface at all times and thereby decreases the number of active nucleation sites. While the absolute boiling performance of both techniques shows significant differences, the trends observed with particle size are remarkably similar. For both techniques, the maximum heat transfer coefficient is observed at a particle size of 90-106 μm, and the maximum CHF is attained for 45-53 μm-diameter particles.

3.3 Conclusions

Free particles and sintered particle coatings are explored for enhancement of pool boiling heat transfer of FC-72 from a heated copper surface, and the effects of particle size are studied for a constant coating layer thickness-to-particle diameter ratio of ~4. With free particles, the 90-106 μm particles exhibit the best boiling heat transfer at higher heat fluxes, with a 32% reduction in the surface superheat compared to the polished surface at 112 kW/m^2; however, the maximum critical heat flux (161 kW/m^2) is attained with the 45-53 μm particles, 44% higher than that for a polished surface. While free

particles provide an actively deformable layer that allows the escape of trapped vapor from the surface (and thereby does not diminish CHF for most particle sizes), entrainment of free particles into the liquid reduces the number of active nucleation sites available for pool boiling at any given time instant. Hence, the fixed sintered particles exhibit significantly higher heat transfer enhancement over a polished surface as compared to free particles of similar size and layer thickness. Nonetheless, the trends observed with particle size are similar between the free-particle and sintered-coating techniques. The best-performing sintered coating, in terms of heat transfer coefficient, has the same 90-106 μm particle range as the free particles, and provides a 95% decrease in wall superheat, albeit at a critical heat flux that is 33% lower than that for the polished surface. The 45-53 μm sintered coating has a CHF approximately the same as that of the polished surface. As the free-particle technique is significantly easier to implement, it may serve as an efficient gauge of expected parametric trends in boiling performance from sintered surfaces.

Table 3.1. Test matrix showing weight, thickness, and porosity of the free and sintered particle layers investigated at each particle size.

Particle size [μm]	Free particles			Sintered particles		
	Weight [g]	δ/d	Porosity [%]	Weight [g]	δ/d	Porosity [%]
850-1000	22.44	4.8	40.2 ± 0.5	15.03	4.2	32.9 ± 0.5
180-212	4.47	4.8	39.9 ± 0.4	3.03	4.2	36.3 ± 1.5
90-106	2.41	4.8	43.1 ± 0.5	1.68	4.1	27.3 ± 1.5
45-53	1.18	4.8	44.4 ± 0.5	0.84	4.1	27.3 ± 3.0

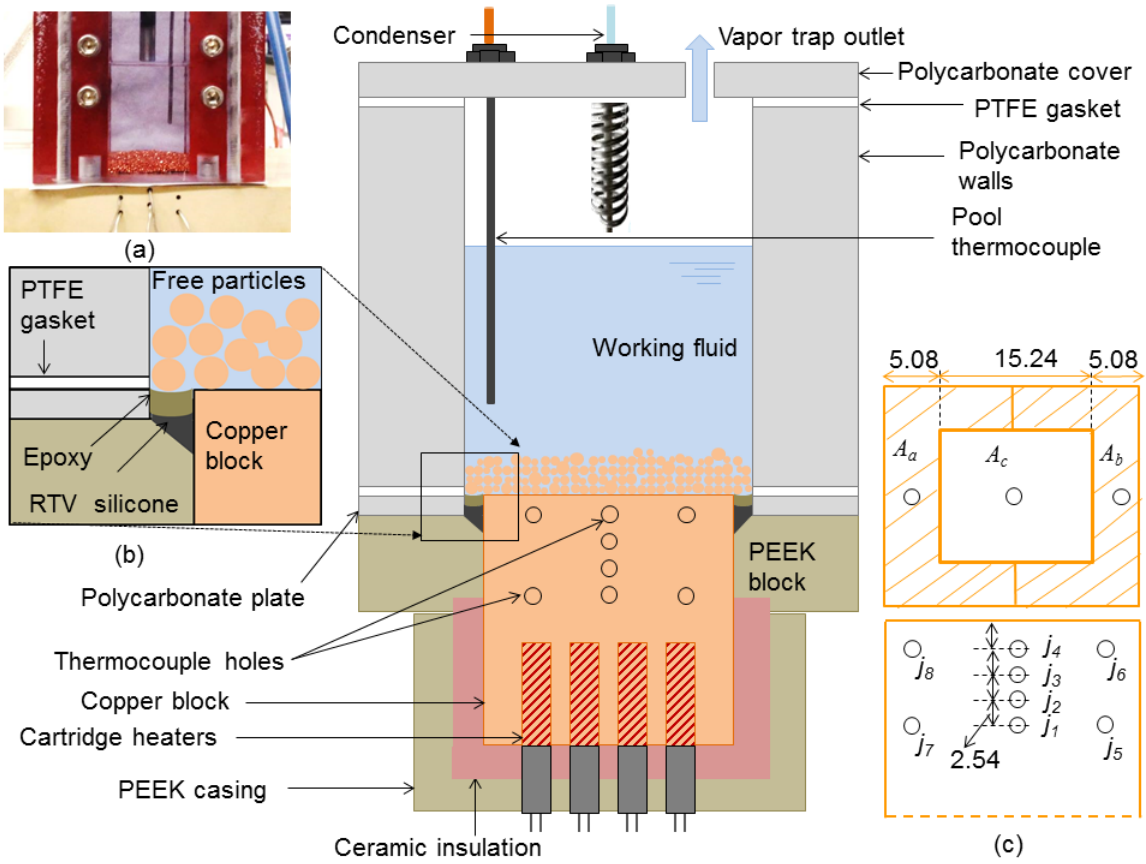

Figure 3.1. Schematic diagram of test facility with insets showing (a) a photograph of the test chamber, (b) a magnified diagram of the sealed seam around the outer edge of the copper test surface, and (c) the schematic top and side views of the copper block showing thermocouple locations and surface area designations (dimensions in mm).

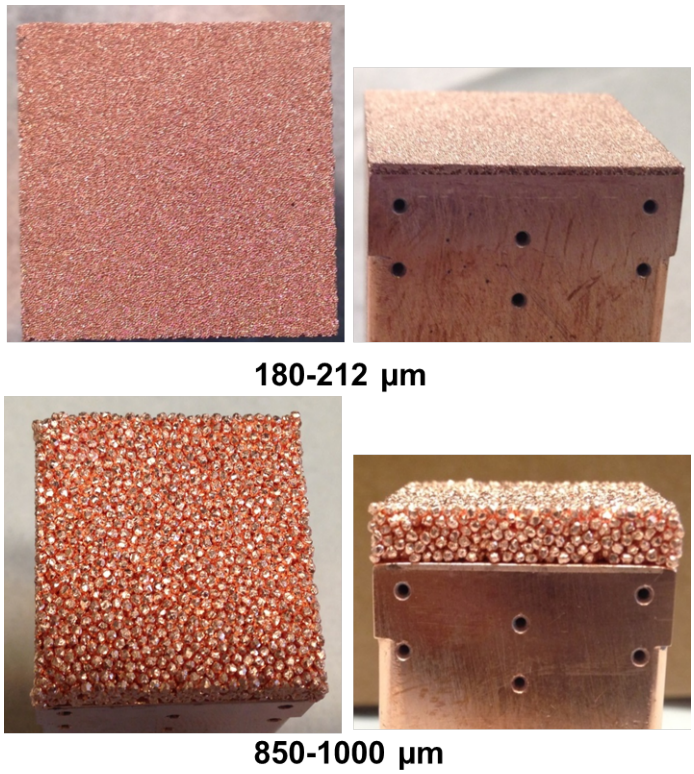

Figure 3.2. Photographs of the 180–212 µm and 850–1000 µm diameter sintered particle coatings from top (left) and side (right) views.

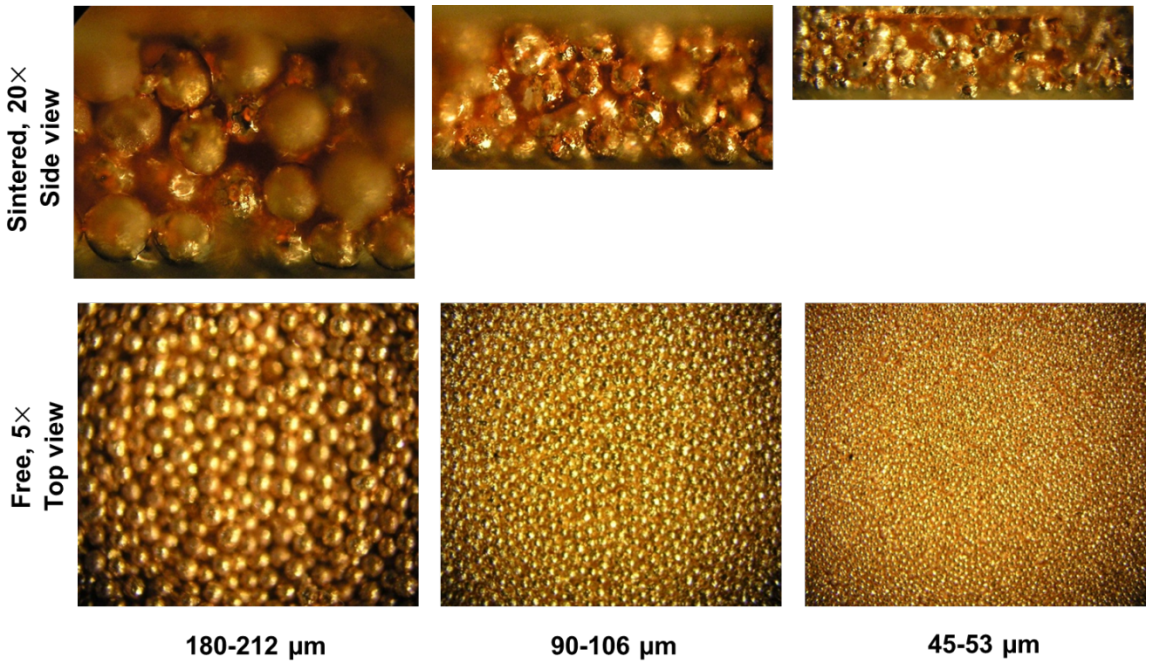

Figure 3.3. Side view of the sintered coatings at 20× magnification (top row), and top view of the free particle layer at 5× magnification (bottom row), for various particles sizes from 45 µm to 212 µm.

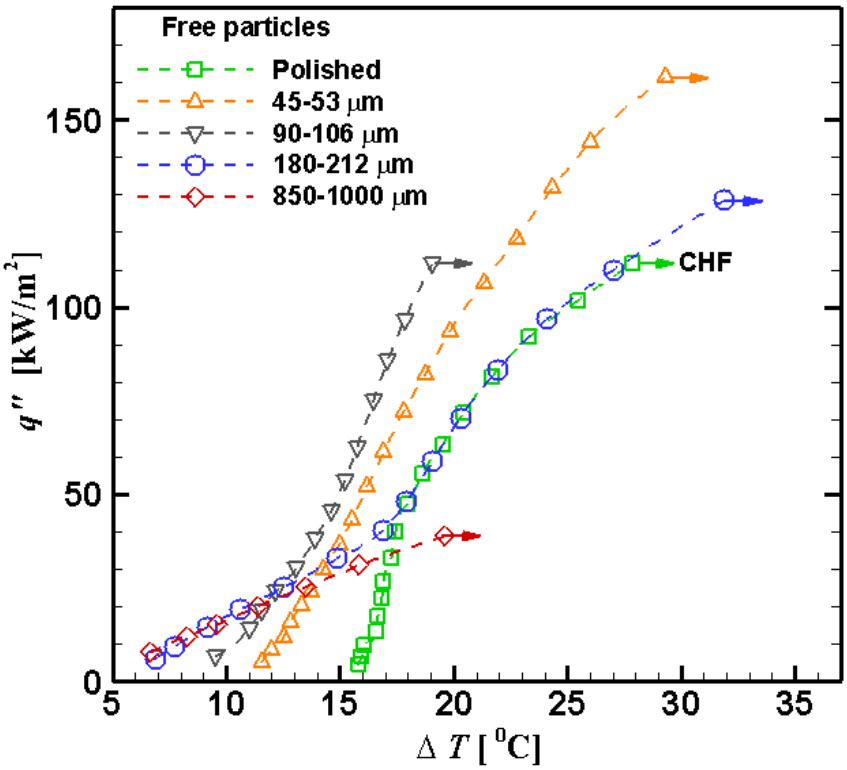

Figure 3.4. Boiling curves of area-averaged heat flux (q'') versus wall superheat (ΔT) for a polished surface baseline compared against enhancement using free spherical copper particles 45 μm to 1000 μm in diameter (δ/d = 4.8; porosity = 40-45%). Critical heat flux is indicated with a horizontal arrow.

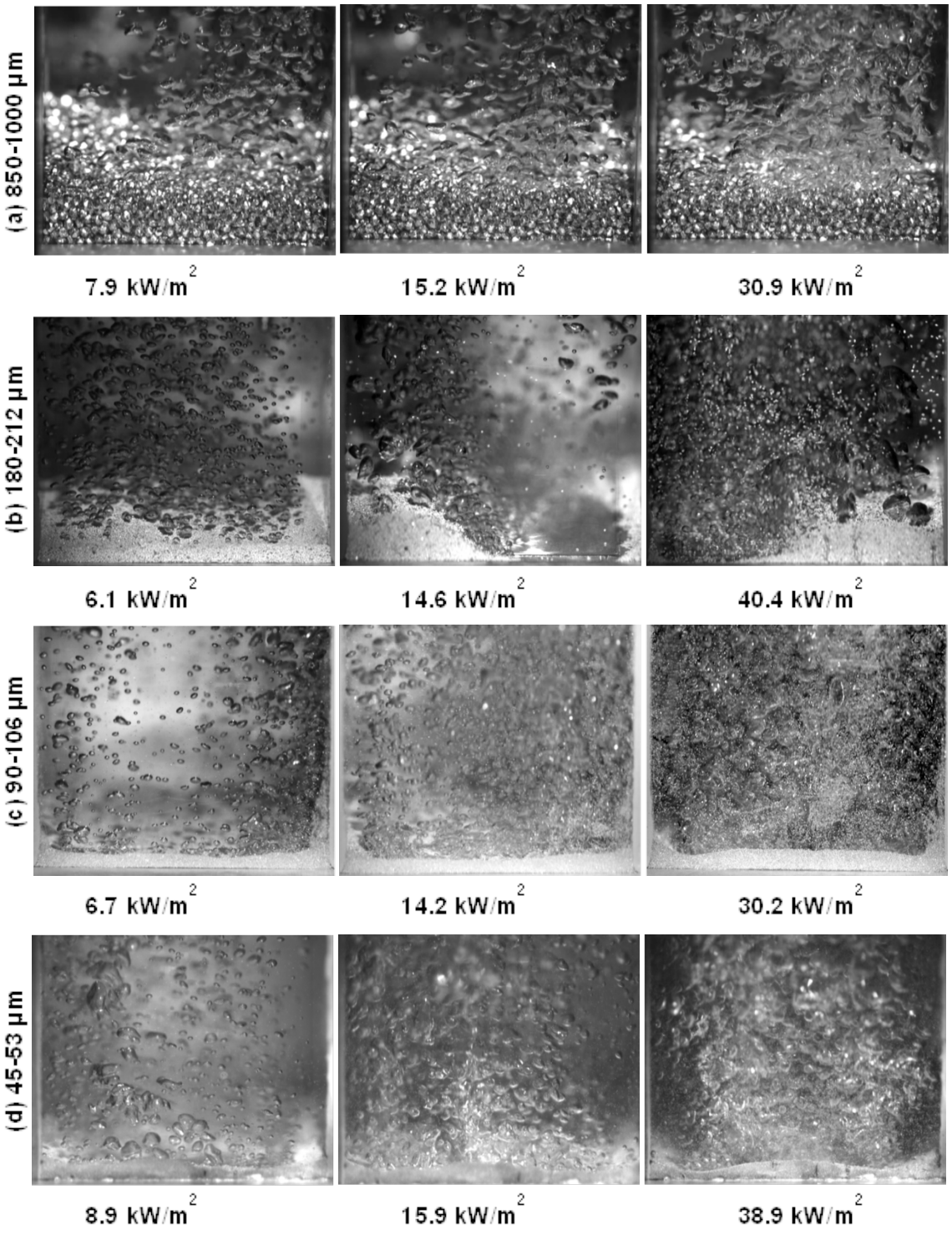

Figure 3.5. Images taken from high-speed visualization at 2000 fps for (a) 850-1000 µm, (b) 180-212 µm, (c) 90-106 µm, and (d) 45-53 µm free particle diameters at similar heat fluxes throughout the boiling curve.

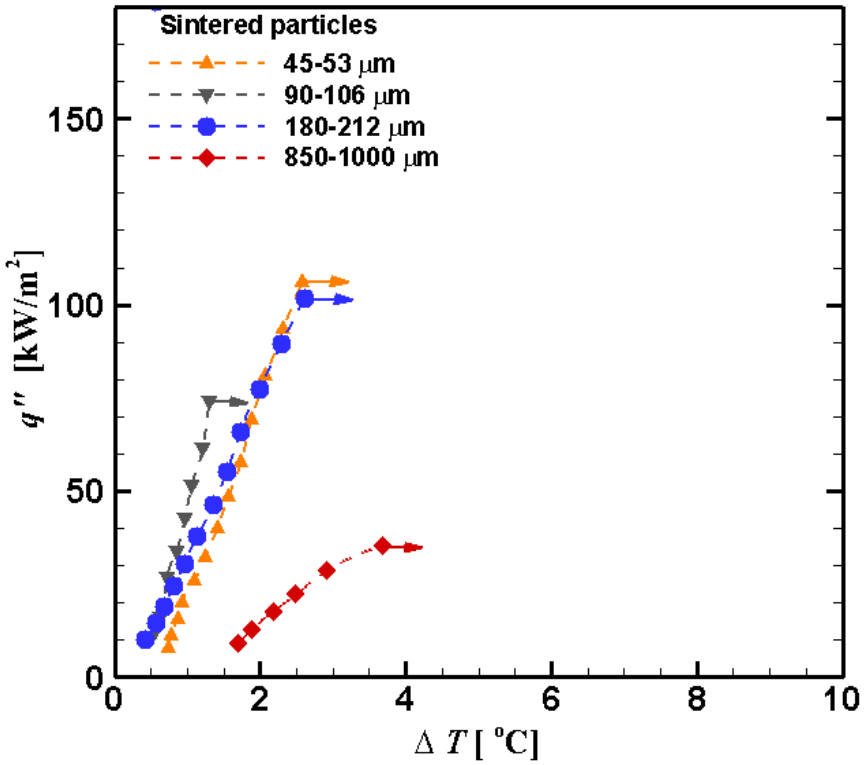

Figure 3.6. Boiling curves of area-averaged heat flux (q'') versus wall superheat (ΔT) for surfaces with sintered spherical copper particles 45 μm to 1000 μm in diameter ($\delta/d \approx 4$ after sintering; porosity = 28-40 %). Critical heat flux is indicated with a horizontal arrow.

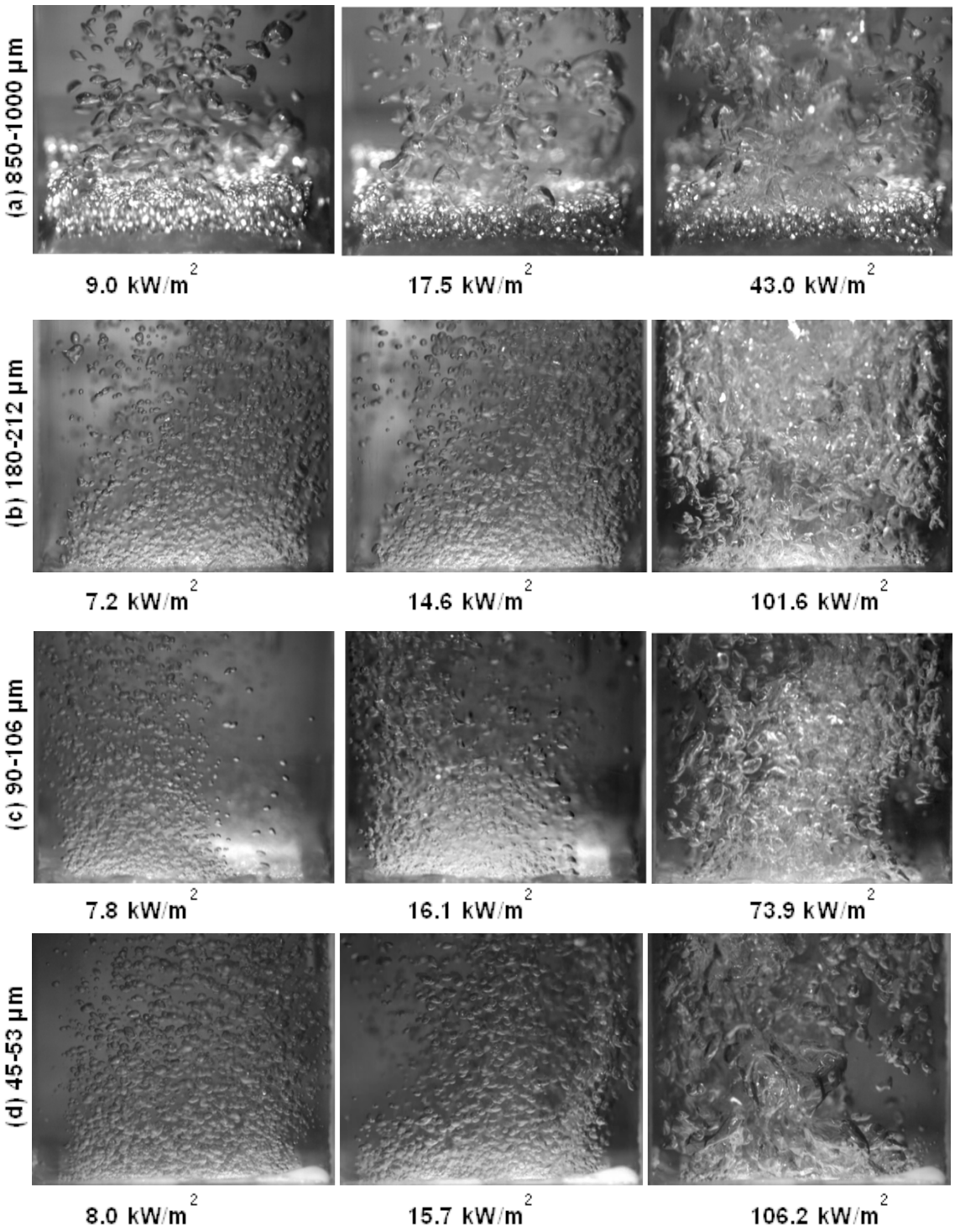

Figure 3.7. Images taken from high-speed visualization at 2000 fps for (a) 850-1000 µm, (b) 180-212 µm, (c) 90-106 µm, and (d) 45-53 µm sintered particle diameters at similar heat fluxes throughout the boiling curve.

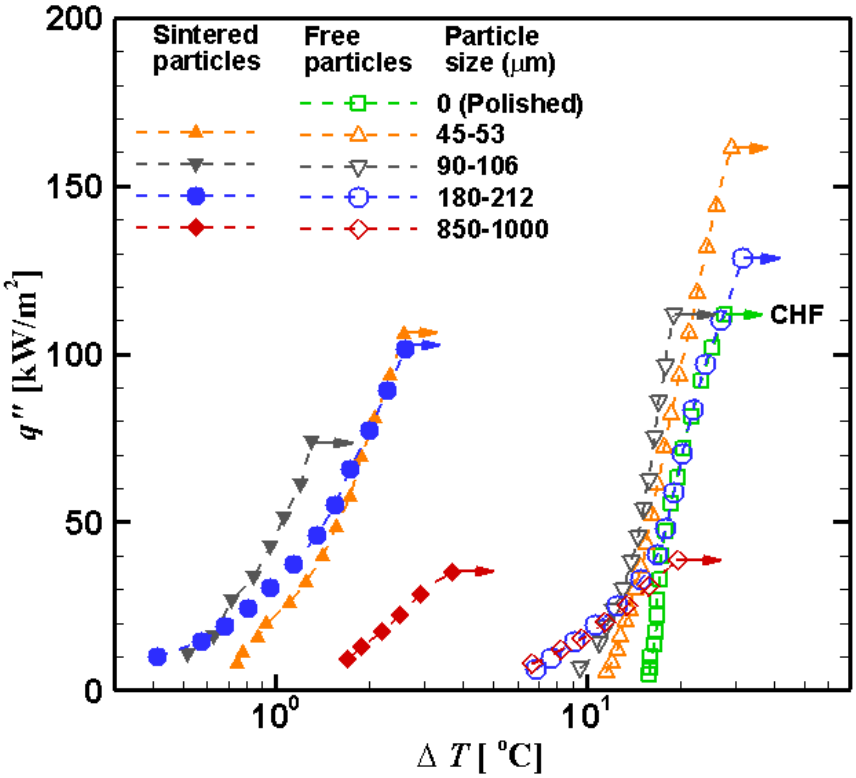

Figure 3.8. Comparison of trends in boiling curves of area-averaged heat flux (q'') versus wall superheat (ΔT) for free and sintered particles with diameters ranging from 45 μm to 1000 μm.

CHAPTER 4. QUANTITATIVE EVALUATION OF THE DEPENDENCE OF POOL BOILING HEAT TRANSFER ENHANCEMENT ON SINTERED-PARTICLE COATING CHARACTERISTICS

This chapter describes the characterization of sintered coatings, and the effects of the coating properties on pool boiling heat transfer performance of the coatings. The morphology and size of the particles affect the pore geometry, permeability, thermal conductivity, and other characteristics of the sintered coating. In turn, these characteristics impact the heat transfer coefficient and CHF during boiling. In this study, pool boiling of FC-72 is experimentally investigated using copper surfaces coated with a layer of sintered copper particles of irregular and spherical morphologies for a range of porosities (~40% to 80%). Particles of the same effective diameter (90-106 μm) are sintered to yield identical coating thicknesses (~4 particle diameters). The porous structure formed by sintering is characterized using micro-computed tomography (μ-CT) scanning to study the geometric and effective thermophysical properties of the coatings. The boiling performance of the porous coatings is analyzed. Coating characteristics that influence the boiling heat transfer coefficient and CHF are identified and their relative strength of dependence analyzed using regression analysis. Irregular particles yield higher heat transfer coefficients compared to spherical particles at similar porosity. The coating porosity, pore diameter, unit necking area, unit interfacial area, effective thermal conductivity, and effective permeability are observed to be the most critical coating

properties affecting the boiling heat transfer coefficient and CHF. The material presented in this chapter is submitted for review in *Journal of Heat Transfer* [59]. Additional experimental results from investigation of effects of particle morphology on pool boiling heat transfer performance are included in Appendix F.

4.1 Experimental Methods

4.1.1 Pool Boiling Test Facility

Figure 4.1 shows a schematic diagram of the pool boiling test facility. An abbreviated description is provided here for this modified version of the facility used by Sarangi *et al.* [50]. The base heater assembly consists of a copper heater block embedded in an insulation casing. The copper block has a 25.4 mm × 25.4 mm top surface coated with sintered particles. The heat input is provided by 12 cartridge heaters (100 W each) inserted into holes in the bottom surface of the block. Block temperatures are measured using T-type thermocouples inserted into tapped holes along three rakes, as shown in Figure 4.1. The copper block is inserted into a block of PEEK, a machinable, low thermal conductivity (0.28 W/m·K) thermoplastic that can withstand temperatures up to 250 °C. A 0.8 mm-thick polycarbonate plate is attached to the top of the PEEK block; the copper block is aligned such that it protrudes just above the polycarbonate plate as shown. The vertical location of the thermocouple rake and the thickness of polycarbonate plate have been slightly altered from the original design [50]. The lower part of the copper block is insulated as described in [50].

The pool boiling chamber is comprised of four polycarbonate walls sealed together with RTV silicone that is cured under compression with screws. The chamber is sealed to the base heater assembly with a compressed PTFE gasket. An aluminum cover plate seals the top of the chamber walls by compressing another PTFE gasket, forming a 30.48 mm × 30.48 mm × 93.9 mm sealed chamber enclosing the working fluid on the heated surface. A T-type thermocouple routed through the cover plate is used to measure the pool temperature during testing. A chilled 50%-50% water-glycol mixture is cycled through the condenser at a flow rate of 0.5 l/min at 15°C using a chiller (ULT-80, Neslab) to condense vapor during testing. A 6.35 mm-diameter polyurethane tube connects the liquid pool to a vapor trap that is open to the ambient during testing and maintains the pool at atmospheric pressure. The chiller flow rate and set-point temperature were selected to ensure that no working fluid collects in the vapor trap during the experiment (to prevent fluid loss from the chamber over time).

4.1.2 Fabrication of Test Surfaces

Copper particles having two different morphologies – irregular and spherical – were used to fabricate the test surfaces. The differences in morphology are brought about by the particle fabrication method. As described in [60, 61], irregular particles are produced by water atomization and spherical particles by air atomization. Irregular particles appear as roughened spheroidal shapes, while spherical particles are smooth. Figure 4.2 shows representative images of the particle shapes observed using a scanning electron microscope (SEM). The SEM images are taken after testing. Due to the different

morphology of the particles, the native packing porosity before sintering is different (48% for spherical particles and 60% for irregular particles). The sintered-coating fabrication method is adjusted to achieve a range of porosities for each particle shape. This requires either reducing or increasing the native packing density of the powder. The porosity of the coating can be reduced by controlling the sintering time and temperature to achieve the desired porosity [50]. In order to increase the porosity beyond the native packing density, the most commonly used method is lost-carbonate sintering (LCS) [62]. A mixture of spherical metal particles, carbonate, and a binder are sintered at high temperature under pressure until the carbonate decomposes or melts, leaving behind a porous metal coating. The carbonate particle size and percentage, as well as the sintering temperature and time, can be controlled to produce porous coatings with the desired porosity and pore diameter

The top surface of the copper heater block is prepared for sintering by sanding with progressively finer diamond sanding sheets (9 μm, 3 μm, and 0.1 μm) followed by metal polishing (Simichrome, Happich). The irregular particles (ACuPowder International) and the spherical particles (Alfa Aesar) are first sieved into the desired size range of 90-106 μm. The range is selected based on the particle size that yielded the best pool boiling heat transfer performance for spherical sintered coatings at ~40% porosity in a prior study [50]. The particles are cleaned by soaking in acetone and rinsing with methanol. To sinter the porous layers with a reduced porosity, loose copper powder is first poured into a graphite mold and leveled off to the desired height. The initial layer thickness of particles is varied, as required, to obtain a final layer thickness-to-particle diameter ratio, δ/d, of ~4, which has been shown to have the maximum heat transfer coefficient in

previous studies [5, 6]. The copper block is then gently placed face-down on top of the powder and the assembly is placed in an evacuated furnace. The temperature is steadily ramped up to 950 °C and held at this temperature under vacuum for the desired time as described in Appendix C. The assembly is then allowed to gradually cool to room temperature under vacuum, and inspected under an optical microscope at multiple locations to ensure a uniform coating thickness.

For the cases where the porosity needs to be increased, an LCS method is used. The copper particles are mixed with spherical potassium carbonate particles (90-150 μm), with a weight fraction as shown in Table 4.1 to achieve the desired porosity. A small amount of ethanol is added to act as a binder in the mold, and the particles are mechanically stirred to ensure uniform mixing. This mixture is then poured into the mold to the desired height, and placed in the evacuated furnace. The temperature of the furnace is steadily ramped up to 850 °C and then held for ~2 h to initiate the sintering process. The temperature is then ramped up further to 950 °C for ~30 min to decompose the carbonate particles (melting point of 891 °C), leaving behind open pores. The assembly is then allowed to cool gradually. This sintering recipe was selected because it has been shown to produce a clean and well-bonded porous structure for the desired porosity range, and does not require any post-processing to remove the potassium carbonate from the sintered matrix [62].

Table 4.1 shows the coating porosity and thickness after the sintering procedure for all the samples fabricated. The height and weight of the copper block are measured before and after sintering to obtain the height and weight of the coated layer. The porosity of the sample is calculated based on the volume occupied by the layer and the

weight of the particles, as described in Appendix B. Figure 4.2 shows representative images of the pore structures observed using a scanning electron microscope (SEM).

4.1.3 Experimental Procedure

To conduct an experiment, the sintered copper block is first assembled into the test facility. The 0.8 mm-thick polycarbonate plate is mounted on the PEEK block to surround the test surface. A chamfer in the PEEK block creates a groove around the outer edges of the test block, which assists in sealing at this location. A layer of RTV silicone sealant is first filled in the groove and cured in an oven for 90 min at 75 °C, followed by the application of a topping layer of epoxy (E 5302 High Temp Epoxylite). The silicone prevents the wicking of epoxy into the gap between the test piece and insulation, thereby facilitating easier removal of test pieces between tests; the high-viscosity paste epoxy, on the other hand, seals out the working fluid, without itself seeping into the pores of the sintered surfaces. The test chamber walls are then secured onto the base and the assembly is cured in the oven for ~20 h at 80 °C.

The assembled test chamber is mounted onto a support stand and filled with 40 ml of FC-72 (T_{sat} = 56 °C, ρ = 1594 kg/m^3, $\mu = 4.3\times10^{-4}$ kg/m s, k = 0.054 W/m·K, h_{fg} = 88 kJ/kg, c_p = 1101 J/kg K, and σ = 0.010 N/m [51]). The cover plate is then secured. The fluid is first degassed by boiling aggressively for 2 h. After degassing, the heat flux is increased in pre-determined steps using the cartridge heaters embedded in the copper block to obtain a boiling curve. Steady-state conditions are assumed to have been reached when the change in calculated surface temperature versus time at each heat flux

setting is less than 0.02 °C/s over 30 min. Once this steady-state criterion is satisfied, the temperature data collected over 120 s are time-averaged for subsequent post-processing of the surface heat flux and temperature. The procedure is continued until CHF is reached, which is marked by a sudden rapid rise in temperature, following which, the power to the heaters is shut off and the system is allowed to cool down. Tests were also conducted with the heat flux being decreased in steps from the maximum value to evaluate if significant hysteresis is observed in the system. As described in Sarangi *et al.* [50], area-averaged wall temperature and heat flux are calculated from the temperature gradients along the three thermocouple rakes. Following the uncertainty analysis procedure described in [50], the respective area-averaged surface temperature and heat flux uncertainties are calculated as ±0.23 °C and ±4.5 kW/m^2 over the range of heat fluxes investigated.

4.2 Coating Characterization

4.2.1 Sample Preparation and Imaging

For sintered particle coatings such as those used in the present work, the high degree of randomness and irregularity make it difficult to use simplified analytical or representative unit-cell models to accurately predict the coating properties. In the present work, micro-computed tomography (μ-CT) is used to resolve the exact three-dimensional (3D) structure of the porous coatings for subsequent characterization.

After the pool boiling test is completed, samples are carefully excised from the copper block surface over a 5 mm × 5 mm footprint area, preserving the original

thickness of the coating. The samples are lightly pressed between two smooth surfaces to flatten out any warping of the samples. The prepared samples are then imaged (Skyscan 1172) at a resolution of 4 μm using a 100 kV X-ray source voltage. The scans were performed in the Department of Anatomy and Cell Biology, Indiana University School of Medicine. The scanner software generates a 2D stack of images corresponding to the 3D object. Appendix G shows example images of single 2D slices obtained form the μ-CT scans, for all the coatings investigated.

4.2.2 Image Processing

The stack of 2D images generated from the μ-CT scans is imported into the commercial software package Simpleware [63] for image processing (ScanIP module) and mesh generation (+FE module). The details of the image processing steps are briefly described here and a more detailed description may be found in Ref. [49]. Example images at each processing step are shown in Figure 4.3 for a reduced portion of the domain. The image processing steps in Figure 4.3 are shown for a single 2D slice for clarity, but all the steps are performed on a 3D volume. Each 2D image of unit-pixel thickness from the stack is 'stitched' with adjacent image slices to generate a 3D volume as shown in Figure 4.3 (b). Copper has much higher X-ray absorptivity than air that fills the surrounding pore region during scanning; hence, the brighter regions correspond to copper and darker regions correspond to the pore space in the image. The transition between these regions is not discrete in the images. In order to accurately differentiate the two regions, a grayscale threshold value is selected such that the porosity of the reconstructed 3D volume matches

the measured porosity of the sample. Figure 4.3 (c) shows an image slice after thresholding. The domains are then inspected for unphysical unconnected regions or islands, which are removed (typically less than four particles or pores over the entire volume scanned). Figure 4.4 shows the 3D solid volumes generated for several of the spherical and irregular particle coatings over the range of porosities investigated. Additional images for all coatings investigated are included in Appendix G.

4.2.3 Evaluation of Geometric Coating Properties

The microscale particles fuse together during the process of sintering, forming one connected 3D volume. It is necessary to identify individual particles and pores to characterize the geometric properties of the coating. This is achieved by using the watershed algorithm available in the Simplware ScanIP module [63]. After segmentation of the individual particles and pores, as shown in Figure 4.3 (d-f), the statistical distribution of particle diameter (d_{part}) and pore diameter (d_{pore}) are obtained for each coating, based on the equivalent spherical volume of each segmented particle/pore. The sphericity (ϕ) is defined as

$$\phi = \frac{\pi^{1/3}\left(6V_{part}\right)^{2/3}}{A} \tag{4.2.1}$$

where V_{part} is the volume of the particle and A is the surface area of a particle. The sphericity (and statistical distribution throughout the sample) indicates the extent to which the constituent particles are spherical (after sintering). The total interfacial area ($S_{int,tot}$) is obtained from the total surface area of the unsegmented copper domain. The

segmentation process identifies the necking areas where particles are adjoined, shown as red lines in the 2D images in Figure 4.3 (e). The total necking area ($S_{neck,tot}$) is obtained by subtracting the total surface area of unsegmented copper domain from that of the segmented copper domain (equivalent to the area of the segmented necks shown in red in Figure 4.3 (e)). The unit interfacial area (S_{int}) and unit necking area (S_{neck}) are obtained by normalizing the total interfacial area and total necking area by the total volume of the sample, respectively.

4.2.4 Mesh Generation

The Simpleware +FE module is used for generating meshes of discretized volumes. The number of particles/pores in the scanned 3D volume is computationally intractable for mesh generation and subsequent numerical simulation processes. Hence, a reduced domain size is carefully chosen such that the geometric properties are maintained and the volumetric porosity matches that of the scanned sample; the length and width of each sample are cropped to 7 pore lengths. A mesh size of 0.1 million cells per pore is selected based on a mesh-independence study performed on a reduced domain size, which shows a 1.6% deviation in effective permeability for 0.1 million cells per pore compared to a refined mesh size of 0.3 million cells per pore. The resulting domain sizes and number of mesh elements for each sample are shown in Table 4.2. The processed 3D volume used for generating meshes consists of 3D voxels, which would generate a stair-stepped mesh if used directly. Hence, the data are smoothed (as recommended by Ref. [63]) to generate high-quality conformal meshes with tetrahedral elements, ensuring the

volume skew limit to be lower than 0.01. Figure 4.5 shows the mesh generated for the spherical particle coating at 39% porosity.

4.2.5 Numerical Modeling

In order to obtain the effective thermophysical properties of the sintered coatings, *viz*., permeability and thermal conductivity, the physics modules available in Simpleware are employed. The primary direction of heat transfer through the sintered coating is in the *z*-direction. Similarly, during boiling, the departure of vapor bubbles and subsequent replenishment of liquid also occurs primarily in this direction. Hence, the effective permeability and conductivity are calculated along the *z*-direction.

The Simpleware +FLOW module is used to calculate the effective permeability of the pore domain. The governing mass and momentum conservation equations are solved using a minimum residual-based homogenization solver and linear pressure variation boundary condition. This boundary condition fixes the pressure on the inlet and outlet faces of the domain, such that the pressure drop per unit length between the inlet and outlet faces is one unit. Linear pressure variation is imposed across the lateral faces, which mimics the more conventionally used symmetry boundary condition [63]. These boundary conditions are shown in Figure 4.6 (a). The effective permeability in the flow direction (*z*-direction) is obtained using Darcy's law

$$U_{av} = -\frac{K_z}{\mu}\nabla P \tag{4.2.2}$$

where ∇P is the applied pressure gradient and K_z is the effective permeability of the medium in the *z*-direction.

The Simpleware +LAPLACE module is used to calculate the effective thermal conductivity of the liquid-saturated porous medium. The governing Laplace equations for diffusion are solved using the conjugate gradient method for the pore and copper domains individually. For the pore domain, fluid properties of FC-72 at room temperature are used while for the solid domain, properties of copper at room temperature are used. A mixed boundary condition is employed that assumes symmetry boundary conditions along the lateral faces and a fixed-temperature boundary at the top and bottom faces, such that the temperature difference per unit length between the top and bottom faces is one unit. Continuity of temperature and heat flux is imposed at the pore-solid interface. The boundary conditions are shown in Figure 4.6 (b). The effective thermal conductivity is computed from

$$q'' = -k_z \frac{\partial T}{\partial z} \tag{4.2.3}$$

where q'' is the heat flux on the bottom wall, $\partial T/\partial z$ is the temperature gradient along the z-direction, and k_z is the effective thermal conductivity of the medium along the z-direction.

The physics modules in the software use a finite element-based homogenization solver. The pressure and velocity components are discretized with continuous linear nodal elements. Further details about the solution methods and boundary conditions may be found in [63].

4.2.6 Quantitative Regression Analysis

The statistical relationship between the coating characteristics and the boiling performance is analyzed in order to identify critical sensitivities. This is achieved by performing a stepwise regression analysis with multiple inputs in MATLAB [64], tailored to represent the input-output relationship in the present study. The data obtained from the boiling experiments and the coating characterization are divided into three primary categories, *viz.*, geometric coating properties, effective thermophysical coating properties, and boiling performance characteristics. First, the dependence of the effective thermophysical properties on the geometric properties is evaluated (*i.e.*, each effective thermophysical property is treated as an output and the geometric properties are treated as inputs). Subsequently, the dependence of the boiling characteristics on the individual geometric and thermophysical properties is determined (*i.e.*, each boiling characteristic is treated as an output, while the geometric and thermophysical properties are treated as inputs).

A stepwise regression is performed using the *stepwiselm* function in MATLAB for each input-output pair, using a quadratic polynomial fit. For the quadratic polynomial fit chosen, there can be either a linear or quadratic dependence between each input and output. The stepwise regression uses forward and backward regression to add or remove terms from the model, based on the p-value of a term, thus determining whether the dependence for each input-output pair is linear or quadratic. The R^2 value of the polynomial fit indicates how well the model fits the actual data (better fit as R^2

approaches unity), while a lower p-value indicates a more significant input parameter term [65, 66].

In order to study the combined effect of multiple input geometric properties, the most critical input geometric parameters are then selected based on the lowest p-values for each output considered. The number of samples tested experimentally limits the number of critical input parameters that can be assessed in combination (maximum of 3). A direct regression is then performed using the *fitlm* function in MATLAB with only the significant terms for each input parameter. The p-value and R^2 value of the resulting dependence are checked for goodness of fit of the significant terms identified. This approach is taken because using a stepwise regression for the final dependence of the combined variable could only identify a smaller number of critical coating parameters, which may not be unique, given the limited number of experimental data points. Hence, after identifying the critical input terms for each output based on the number of experimental data points available (*i.e.,* 3 critical inputs), a direct regression forces the final model to include all these critical input parameters so as to obtain a combined dependence. It is noted that the p-value of the final model should therefore not be compared to that of the individual input-output pairs, but simply used as a stand-alone indicator of the significance of the terms in the final model.

4.3 Results and Discussion

4.3.1 Boiling Curves

For porous coatings formed from particles of the same size (90-106 μm), each distinct particle morphology and porosity creates pores of unique shapes, thereby leading to differences in the boiling heat transfer performance. Figure 4.7 shows the boiling curves obtained for the irregular and spherical particle coatings described in Table 4.1.

Compared to a polished surface [50], these sintered surfaces show boiling incipience wall superheat that is 16-80 times lower, heat transfer coefficients that are 8-25 times higher, and CHF that is higher by a factor of 1.2-2. The increased density of active nucleation sites and enhancement of heat transfer area are the primary contributors to the heat transfer coefficient enhancement for such sintered surfaces. The overall trend of the boiling curves is similar to that of typical sintered surfaces. At very low heat fluxes (below ~4 kW/m^2, not shown on the graph), natural convection heat transfer occurs. As the heat flux is increased, nucleate boiling incipience occurs at very low wall superheat (<1 K). With further increase in heat flux, the wall superheat consistently increases. The heat transfer coefficient, as shown in Figure 4.8, is a function of the wall superheat at any given heat flux as is typically observed for pool boiling studies, although the exact variation depends on the individual coating characteristics.

Comparing the boiling curves for the different coating geometries, it is observed that boiling incipience occurs for all of the different coatings at a low superheat (0.2 K to 1 K) and a heat flux of ~5-9 kW/m^2. As the heat flux is increased beyond incipience, the wall superheat continues to increase. For both spherical and irregular particle coatings, it is

observed that the heat transfer coefficient generally decreases with increase of coating porosity throughout the range of porosities investigated (~40%-80%). For the low-porosity coatings (up to 55% for spherical and 51% for irregular), the heat transfer coefficient increases at a rapid rate after incipience, reaches a maximum value and then decreases at higher heat fluxes (indicated by the increasing and then decreasing slope of the boiling curve). However, increasing the porosity above these porosities alters the nature of the boiling curve. For these higher porosities, heat transfer coefficient increases monotonically as the heat flux increases, as has been previously observed for sintered spherical coatings [50, 67]. The irregular particle coatings show better heat transfer performance (*i.e.*, a lower superheat at a given heat flux, implying a higher heat transfer coefficient) compared to the spherical coatings at similar porosities throughout the boiling curve.

The coating characteristics also have an effect on the CHF. Low-porosity particle coatings generally have a lower CHF than higher-porosity coatings; *e.g.*, irregular particle coatings with porosity ≤58% reach CHF at ~135±2 kW/m^2 and spherical particle coatings with porosity ≤55% reach CHF at ~159±4 kW/m^2. Above these coating porosities, a sudden jump in CHF is observed (to 226±5 kW/m^2 for irregular particle coatings and 236±0.4 kW/m^2 for spherical particle coatings).

This drastic change in the behavior of the boiling curve heat transfer coefficient and CHF at a critical porosity value suggests the presence of a corresponding change in some governing coating characteristics at this porosity. The general trends in boiling performance are first qualitatively analyzed in light of the morphology of the sintered particle coatings revealed by the SEM images in Figure 4.2, followed by a quantitative

analysis of the boiling characteristics in terms of the coating properties evaluated from μ-CT scans.

4.3.2 Qualitative Image Analysis

It is observed from Figure 4.2 that the structure of the open pores and the particle packing arrangement in the sintered coatings depend on the particle morphology and coating porosity. The pores in the irregular particle coatings qualitatively appear smaller and more tortuous than in the case of the spherical particles. Larger pores at similar porosity, as seen in the spherical particle coatings, may be indicative of lesser interfacial area between the liquid in the pores and the copper particles, as well as reduced contact between individual copper particles, thereby reducing the effective thermal conductivity of the coating. It is also clear from the images that the spherical particles have a notably smoother surface compared to the roughness displayed by the irregular particles. This inherent surface roughness likely leads to an enhancement of the interstitial surface area available for heat transport during boiling with the irregular particles at the same porosity. For a fixed particle type, Figure 4.2 shows that pore diameters increase with porosity. The heat transfer performance of the coatings is consistent with these qualitative observations regarding the pore size and surface roughness; irregular particles have a higher heat transfer coefficient than spherical particles, and higher-porosity coatings have lower heat transfer coefficients.

The pore size also has an effect on the CHF reached by the coatings. Larger pores allow more efficient vapor escape at higher heat fluxes, thereby leading to higher CHF for

coatings with higher porosities, consistent with findings from previous studies [11, 68]. Between the two particle types, spherical particle coatings have slightly higher CHF at the same porosity compared to irregular particle coatings, which is consistent with the larger pore size observed in the images.

The pore structure may also explain the observed change in slope of the boiling curve for the different coating porosities. As the heat flux is increased, the heat transfer coefficient initially increases for all samples. However, as noted in the previous section, further increases in heat flux reduce the heat transfer coefficient for coating porosities below 55% (Figure 4.8). This behavior may be attributed to inefficient vapor escape and liquid replenishment through these coatings, compared to the behavior with the larger pores at higher coating porosities.

While the SEM images provide qualitative visualization of the pore structure of the coatings, the quantitative characterization presented in the following sections is essential to establishing the geometric differences between the coatings, identifying critical parameters that affect the boiling heat transfer performance of sintered particle coatings, and allowing firm conclusions to be drawn about the boiling curve trends on the basis of significant coating characteristics.

4.3.3 Geometric and Effective Thermophysical Properties of the Coating

The geometric properties of the coatings are obtained from the μ-CT reconstructions as described in Section 4.2.3. Table 4.3 shows the geometric coating parameters for each particle morphology and porosity investigated, *viz.*, coating porosity (ε), particle diameter

(d_{part}) distribution, pore diameter (d_{pore}) distribution, sphericity (ϕ) distribution, unit interfacial area (S_{int}) and unit necking area (S_{neck}). The numerically simulated values of effective permeability (K_z) and effective thermal conductivity (k_z) along the z-direction are also shown. The arrows at the bottom of each column indicate whether the property increases or decreases with an increase of coating porosity. Figure 4.9 shows representative temperature and pressure contours obtained from the numerical simulations for a spherical particle coating at 39% porosity and an irregular particle coating at 66%. The temperature and pressure are observed to be stratified along the z-direction, as with past observations in the literature [49]. The heat transfer coefficient and CHF for the boiling curves are also shown in Table 4.3. The heat transfer coefficient (h_{av}) is an average value computed over the range of heat fluxes varying from 25% to 75% of CHF. This average heat transfer coefficient is merely an indicative representation of the heat transfer coefficient provided by the coating across much of the boiling curve. Figure G.8 shows the Nusselt number for all the samples, calculated based on three representative length scales, *i.e.* d_{pore}, (1/ S_{int}) and (1/ S_{neck}).

It may be noted here that while all coatings were fabricated using loose particles sieved to the same size range (90-106 μm), the average particle diameters are reduced upon sintering, and are observed to be of the same order, of ~70-85 μm. The sphericity of the coatings is also observed to be fairly constant over the range of porosities investigated. The irregular particle coatings show a slightly smaller average sphericity compared to the spherical particle coatings. The sphericity is indicative of the qualitative morphological differences between the two types of coatings formed by spherical and irregular particles.

For both spherical and irregular coatings, the average pore diameter increases with an increase in the coating porosity (from ~50 μm to ~100 μm over the porosity rage), as was observed qualitatively from the SEM images. The average pore size (as well as the standard deviation) shows a gradual increase with porosity up to an intermediate value (55% for spherical and 58% for irregular particle coatings), followed by a sharp increase. This quantitative characterization is consistent with the drastic change in the trends of the boiling heat transfer coefficient and CHF noted at this intermediate porosity, as was described in Section 4.3.1. This sharp increase may be attributed to the large increase in the percentage of carbonate particles from 10% to 45% that was necessary to achieve the desired higher porosity. While for low carbonate percentages (~0-10%) the pore size may be dominated by the size of copper particles, the pores formed at higher carbonate percentages may be determined by both the carbonate and the copper particle sizes, and hence show a wider size distribution. Coatings with higher porosity and pore sizes are also shown to have higher permeability values in Table 4.3. Since permeability indicates the ease with which fluid can pass through the coating, higher permeability leads to more efficient vapor escape, resulting in a higher CHF. This is in accordance with the observations above, where coatings with a higher porosity or pore size show a drastic increase in CHF due to the associated higher permeability. Irregular particle coatings which have smaller pore sizes also have lower permeability, and hence, lower CHF than spherical particle coatings at similar porosity. While measuring the bulk coating characteristics such as porosity may provide insight into the general trends of the boiling performance, it is insufficient to explain the finer differences such as the drastic change in CHF, which is more clearly explained from the pore structure analysis. Hence, a high-

fidelity characterization of the pore statistics is essential to interpreting the boiling performance of the coatings, as is performed herein.

The unit interfacial area (S_{int}) of the sintered particle coatings denotes the surface area available for heat transfer between the solid and fluid domains during boiling, while the unit necking area (S_{neck}) indicates the contact area available for solid-solid conduction between individual copper particles. For both spherical and irregular particle coatings, an increase in porosity is associated with a reduction in S_{int} as well as S_{neck}, as shown in Table 4.3. At similar porosities, spherical particle coatings have smaller S_{int} compared to irregular particle coatings, owing to the smoother particle surfaces, as seen from an observation of the SEM images in Section 4.3.2. Spherical particle coatings also have smaller S_{neck}, compared to irregular particle coatings. A larger interfacial area within the coating layer can be more efficiently utilized when the necking area is large; this combination leads to a higher effective thermal conductivity and heat transfer coefficient. Across all the samples considered, coatings with a lower porosity or with irregular particles definitively exhibit higher heat transfer coefficients than those with a higher porosity or with spherical particles (as also observed in Section 4.3.1), due to the larger interfacial and necking areas (and higher thermal conductivities) associated.

4.3.4 Quantitative Analysis of the Dependence of Boiling Curves on Coating Properties

Section 4.3.3 described trends in the boiling heat transfer coefficient and critical heat flux with the geometric and effective thermophysical coating properties. While the trends with respect to each property have been qualitatively identified, a modified stepwise

regression analysis is now performed to quantify the relative dependence of the boiling performance on each property, and to identify the critical coating properties to which the boiling performance is most sensitive.

To analyze the effect of geometric properties on the effective thermophysical properties (permeability K_z and thermal conductivity k_z) of the coatings, each geometric parameter is first treated as a single input with the thermophysical property as an output. The standard deviation of pore size differs significantly across the coatings; hence, it is treated as an individual input parameter (σ_{dpore}) that could affect the coating performance independent of the pore size itself. Based on the stepwise regression analysis described in Section 4.2.6, the best-match relationship (*i.e.,* linear or quadratic) between the inputs and output is identified, as are the critical input parameters with lowest p-values (indicated in bold in Table 4.4). For K_z, the lowest p-values are observed for porosity, pore size, and standard deviation of pore size, deemed to be the most significant factors in determining the effective permeability. This is in accordance with the literature, which shows a strong dependence of permeability on coating porosity from the classical Kozeny-Carman relation, Eq (2.2.1), and several variations on this equation [69-71] that identify the pore structure characteristics (such as pore size distribution) as a critical factor affecting permeability. The permeability K_z in the present work is observed to show quadratic variation with ε and d_{pore}, and linear variation with σ_{dpore} for both particle types. To determine the final dependence of the combined variables, a direct regression is then performed using only the critical input terms ε^2, d_{pore}^2 and σ_{dpore}, which results in a low p-value and high R^2 value as shown in Table 4.4. Following the same analysis, the most significant factors in determining the effective thermal conductivity are observed to be ε

and S_{neck} (linear relationship), as well as S_{int} (quadratic relationship). The thermal conductivity of coatings would be expected to vary with coating porosity [72-74] as well as the unit necking area [49], thus supporting the validity of the method used in the present study. The p-value and R^2 value of the resulting functions are shown in Table 4.4 and are indicative of the goodness of fit of the significant terms. It is important to note that, while the p-value demonstrates the relative significance of the inputs within one dataset, the exact magnitudes cannot be compared between two statistically different datasets, *i.e.*, spherical and irregular particle coatings.

The dependence of effective permeability K_z and thermal conductivity k_z on the geometric coating properties are fairly well established in the literature. However, there are no unified models depicting the dependence of boiling performance metrics on the geometric and thermophysical coating properties. The regression analysis approach is extended to quantitatively establish this dependence of the heat transfer coefficient and CHF on the coating properties, as shown in Table 4.5, with critical inputs shown in bold. The variation of h_{av} with the normalized critical input properties is shown in Figure 4.10. Each input property is normalized based on its maximum value for each type of coating. It is demonstrated that h_{av} is most significantly affected by the geometric properties ε, d_{pore}, and S_{neck} (all linear-dependence relationships), as also observed qualitatively in Section 4.3.3 and indicated in bold in Table 4.5. The effective thermal conductivity $k_{z,}$ which is directly dependent on these geometric properties as discussed in Section 4.3.3, is shown to be the most significant thermophysical property affecting the average heat transfer coefficient linearly.

As shown in Table 4.5, CHF is observed to vary linearly with the key parameters ε, d_{pore} and S_{int}. This agrees with the discussion in Section 4.3.3, where ε and d_{pore} were observed to affect the effective permeability K_z (also shown to be the most significant thermophysical property affecting CHF of the coatings), which likely determines vapor escape and hence CHF of the coatings. While the effect of S_{int} on CHF may not be intuitive, all the geometric parameters are not truly independent. The value of S_{int} is dependent on both ε and d_{pore} as observed qualitatively, and hence, the cumulative effect likely enhances its influence on CHF. Figure G.9 shows the relationship between unit interfacial area and pore diameter.

4.4 Conclusion

The effects of coating characteristics on pool boiling heat transfer performance are investigated for porous coatings formed by sintering copper particles of two different morphologies, *viz.,* irregular and spherical, for particle sizes of 90-106 μm over a wide range of coating porosities (40%-80%). Image analysis of the coatings is performed using SEM images and μ-CT scans to obtain qualitative and quantitative characteristics of the coating geometry. Numerical simulation of transport in the reconstructed 3D coatings is performed to obtain the effective thermophysical properties of the coatings. The dependence of the heat transfer coefficient and CHF on the geometric and thermophysical coating properties is quantitatively determined using a modified stepwise regression analysis.

The boiling heat transfer performance for the coatings is observed to be strongly dependent on the observed differences in the structure of the interstitial pores formed in each coating. The coating porosity, pore diameter, unit necking area, effective thermal conductivity, and effective permeability are observed to be the most critical coating properties affecting the boiling heat transfer coefficient of the coatings. The CHF of the coatings is most strongly affected by the coating porosity, pore diameter, unit interfacial area, effective permeability, and effective conductivity. The coatings with lower porosities or irregular particles show larger heat transfer coefficients along the boiling curve compared to coatings with higher porosities or spherical particles. A sharp shift in the nature of the boiling curve and CHF is observed at an intermediate porosity. The boiling curve characteristics depend strongly on the particle morphology, coating pore structure, and effective thermophysical properties of the coated layer, which can vary widely even for coatings having similar porosity. The bulk coating porosity is inadequate to explain this sharp change in boiling curve behavior, but this trend is clearly explained in terms of the coating pore size distribution, interfacial area, necking area, effective permeability and effective thermal conductivity obtained from high-fidelity characterization of the pore statistics using μ-CT image analysis. This characterization approach is demonstrated to provide essential insight into the dependence of boiling curve metrics on critical coating properties.

Table 4.1. Sintering conditions and resulting porosity of the spherical and irregular sintered particle coatings fabricated.

Particle shape	Carbonate weight fraction [%]	δ/d [-]	ε [%]
Spherical	0	3.9	39
	0	3.9	45
	10	4.4	55
	45	4.1	68
	60	3.7	72
	80	4.2	79
Irregular	0	3.8	51
	10	4.2	58
	45	3.5	66
	60	3.5	71
	80	3.9	74

Table 4.2. Numerical mesh and domain size.

Particle shape	ε [%]	Domain size $x \times y \times z$ [μm × μm × μm]	Number of cells ($\times 10^6$)
Spherical	39	$340 \times 340 \times 207$	15.7
	45	$480 \times 480 \times 163$	10.3
	55	$520 \times 520 \times 219$	15.4
	68	$700 \times 700 \times 219$	14.2
	72	$720 \times 720 \times 219$	14.5
	79	$760 \times 760 \times 203$	14.0
Irregular	51	$340 \times 340 \times 195$	20.2
	58	$420 \times 420 \times 199$	18.6
	66	$540 \times 540 \times 199$	16.4
	71	$620 \times 620 \times 203$	15.5
	74	$680 \times 680 \times 219$	16.0

Table 4.3. Geometric properties, effective thermophysical properties, and boiling performance of the sintered particle coatings investigated. The arrows at the bottom of each column indicate whether the property increases (upward arrow) or decreases (downward arrow) with increase of porosity, for each type of coating.

Particle shape	Geometric Properties						Effective Thermophysical Properties		Boiling Performance	
	ε [%]	d_{pore} [μm]	d_{part} [μm]	ϕ	S_{int} [mm^{-1}]	S_{neck} [mm^{-1}]	K_z [$\times 10^{-5}$ mm^2]	k_z [W/ m.K]	h_{av} [kW/ m^2.K]	CHF [kW/ m^2]
Spherical	39	48±24	85±18	0.79±0.11	74	12.4	1.6	129	66.6	162
	45	65±27	80±17	0.73±0.16	72	9.5	3.5	105	56.9	154
	55	73±31	84±17	0.70±0.09	63	8.1	7.7	78.3	41.3	160
	68	96±52	77±15	0.75±0.1	34	5.4	31.2	40.3	36.9	235
	72	104±50	79±22	0.79±0.12	30	2.8	33.1	29.3	34.3	236
	79	107±59	77±15	0.79±0.11	27	2.2	41.8	16.9	28.0	235
	↑	↑	—	—	↓	↓	↑	↓	↓	↑
Irregular	51	52±19	75±17	0.57±0.09	84	12.9	1.6	141	78.2	137
	58	61±24	73±16	0.60±0.22	73	8.3	1.8	86.6	63.5	134
	66	78±32	71±14	0.70±0.10	54	5.5	6.9	54.1	59.4	223
	71	85±39	69±14	0.74±0.15	47	4.3	11.1	42.7	55.9	223
	74	94±42	70±14	0.71±0.10	43	3.9	17.6	37.5	48.9	233
	↑	↑	—	—	↓	↓	↑	↓	↓	↑

Table 4.4. Analysis of the relationship between geometric coating properties and the effective thermophysical properties. The critical input properties affecting each output are shown underlined and bold.

Effective thermo-physical property	Input geometric property	Spherical particle coating			Irregular particle coating		
		Variable dependence	R^2	p-value ($\times 10^{-3}$)	Variable dependence	R^2	p-value ($\times 10^{-3}$)
Permeability, K_z [mm^2]	**$\underline{\varepsilon}$**	$f(\varepsilon^2)$	0.96	0.34	$f(\varepsilon^2)$	0.98	12.7
	$\underline{d_{pore}}$	$f(d^2_{pore})$	0.95	0.55	$f(d^2_{pore})$	1	5.4
	S_{int}	$f(S^2_{int})$	0.99	0.86	$f(S^2_{int})$	0.94	30.3
	S_{neck}	$f(S_{neck})$	0.88	3.5	$f(S_{neck})$	0.56	90.7
	d_{part}	$f(d_{part})$	0.63	37	$f(d_{part})$	0.56	89.8
	$\underline{\sigma_{dpore}}$	$f(\sigma_{dpore})$	0.99	0.02	$f(\sigma_{dpore})$	0.87	12.9
	ϕ	$f(\phi)$	0.04	333	$f(\phi)$	0.55	92.5
	$\underline{\varepsilon, d_{pore}, \sigma_{dpore}}$	$f(\varepsilon^2, d^2_{pore}, \sigma_{dpore})$	0.99	8.6	$f(\varepsilon^2, d^2_{pore}, \sigma_{dpore})$	0.96	120
Thermal Conductivity, k_z [W/m.K]	**$\underline{\varepsilon}$**	$f(\varepsilon)$	0.99	0.02	$f(\varepsilon)$	0.91	6.5
	d_{pore}	$f(d^2_{pore})$	0.98	0.91	$f(d^2_{pore})$	0.96	19.2
	$\underline{S_{int}}$	$f(S^2_{int})$	0.95	0.54	$f(S^2_{int})$	0.95	2.8
	$\underline{S_{neck}}$	$f(S_{neck})$	0.97	0.22	$f(S_{neck})$	1	0.01
	d_{part}	$f(d_{part})$	0.57	52	$f(d_{part})$	0.90	8.6
	σ_{dpore}	$f(\sigma_{dpore})$	0.92	1.4	$f(\sigma_{dpore})$	0.84	18.6
	ϕ	$f(\phi)$	0.16	599	$f(\phi)$	0.83	20.8
	$\underline{\varepsilon, S_{neck}, S_{int}}$	$f(\varepsilon, S_{neck}, S^2_{int})$	0.99	5.8	$f(\varepsilon, S_{neck}, S^2_{int})$	1	24.5

Table 4.5. Analysis of the relationship between the geometric and effective thermophysical properties on boiling performance characteristics. The critical input properties affecting each output are shown underlined and bold.

Boiling performance	Input variable type	Input geometric parameter	Spherical particle coating			Irregular particle coating		
			Variable dependence	R^2	p-value ($\times 10^{-3}$)	Variable dependence	R^2	p-value ($\times 10^{-3}$)
Average heat transfer coefficient, h_{av} [kW/m^2.K]	Geometric property	**$\underline{\varepsilon}$**	$f(\varepsilon)$	0.96	0.31	$f(\varepsilon)$	0.96	2.6
		$\underline{d_{pore}}$	$f(d_{pore})$	0.94	0.79	$f(d_{pore})$	0.91	7.6
		S_{int}	$f(S^2_{int})$	0.92	9.9	$f(S^2_{int})$	0.92	42.5
		$\underline{S_{neck}}$	$f(S_{neck})$	0.92	1.5	$f(S_{neck})$	0.98	1.0
		d_{part}	$f(d_{part})$	0.56	88.4	$f(d_{part})$	0.87	13.1
		σ_{dpore}	$f(\sigma_{dpore})$	0.85	5.3	$f(\sigma_{dpore})$	0.90	9.3
		ϕ	$f(\phi)$	0.21	738	$f(\phi)$	0.77	32.4
		$\underline{\varepsilon, d_{pore}, S_{neck}}$	$f(\varepsilon, d_{pore}, S_{neck})$	0.93	39.5	$f(\varepsilon, d_{pore}, S_{neck})$	0.96	114
	Effective thermo-physical property	K_z	$f(K_z)$	0.84	6.8	$f(K_z)$	0.67	56.2
		$\underline{k_z}$	$f(k_z)$	0.98	0.13	$f(k_z)$	0.97	1.20
Critical heat flux, CHF [kW/m^2]	Geometric property	**$\underline{\varepsilon}$**	$f(\varepsilon)$	0.80	10.1	$f(\varepsilon)$	0.81	23.6
		$\underline{d_{pore}}$	$f(d_{pore})$	0.80	9.8	$f(d_{pore})$	0.85	16.5
		$\underline{S_{int}}$	$f(S_{int})$	0.95	0.59	$f(S_{int})$	0.88	11.4
		S_{neck}	$f(S_{neck})$	0.74	18.2	$f(S_{neck})$	0.71	47.6
		d_{part}	$f(d_{part})$	0.58	48.6	$f(d_{part})$	0.75	37.4
		σ_{dpore}	$f(\sigma_{dpore})$	0.91	1.9	$f(\sigma_{dpore})$	0.81	25
		ϕ	$f(\phi^2)$	0.10	539	$f(\phi^2)$	0.86	71.8
		$\underline{\varepsilon, d_{pore}, S_{int}}$	$f(\varepsilon, d_{pore}, S_{int})$	0.99	2.4	$f(\varepsilon, d_{pore}, S_{int})$	0.99	55.6
	Effective thermo-physical property	**$\underline{K_z}$**	$f(K_z^2)$	0.93	8.8	$f(K_z^2)$	0.91	46
		k_z	$f(k_z)$	0.79	10.8	$f(k_z)$	0.70	49.2

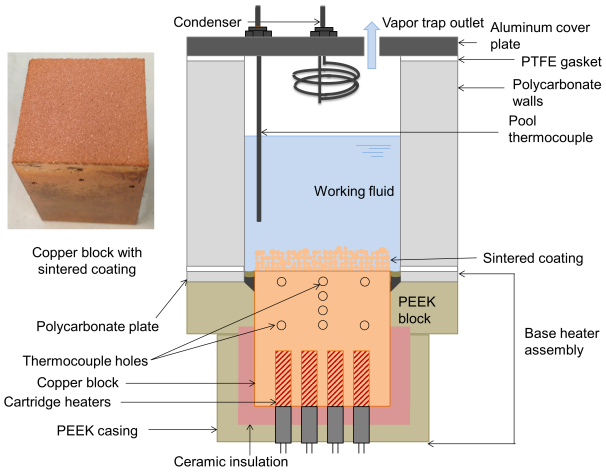

Figure 4.1. Schematic diagram of test facility with inset showing a photograph of a copper block coated with spherical sintered particles.

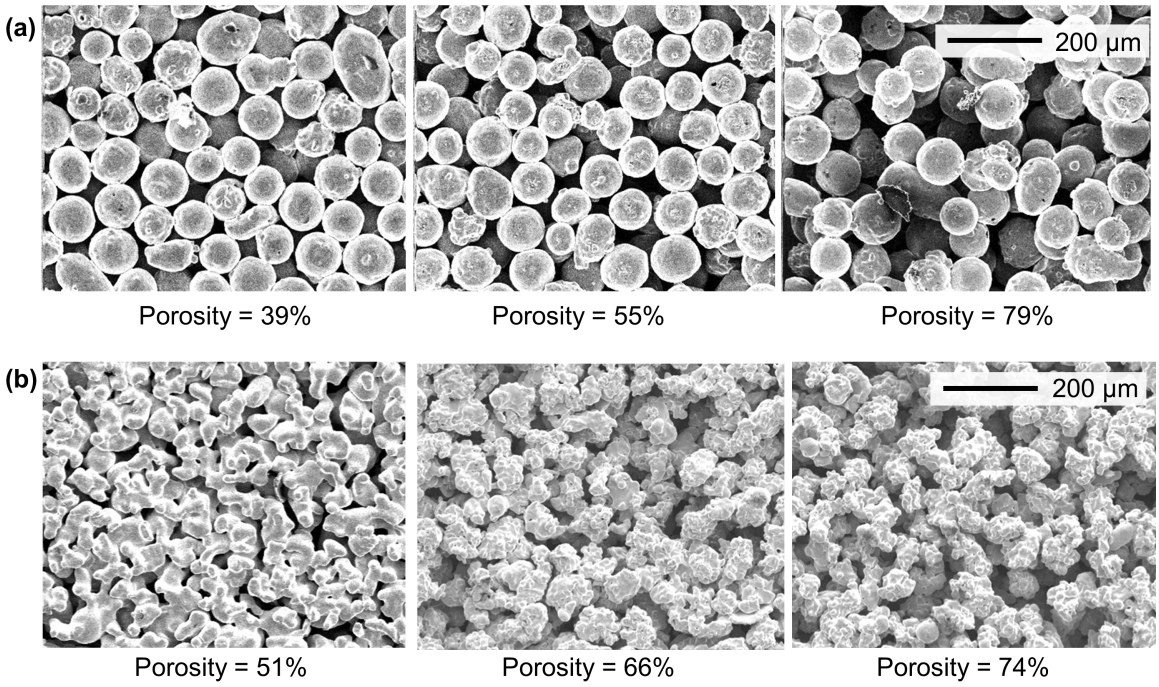

Figure 4.2. SEM images of (a) spherical and (b) irregular coatings at a low, intermediate, and high porosity, showing the pore structure of the coatings.

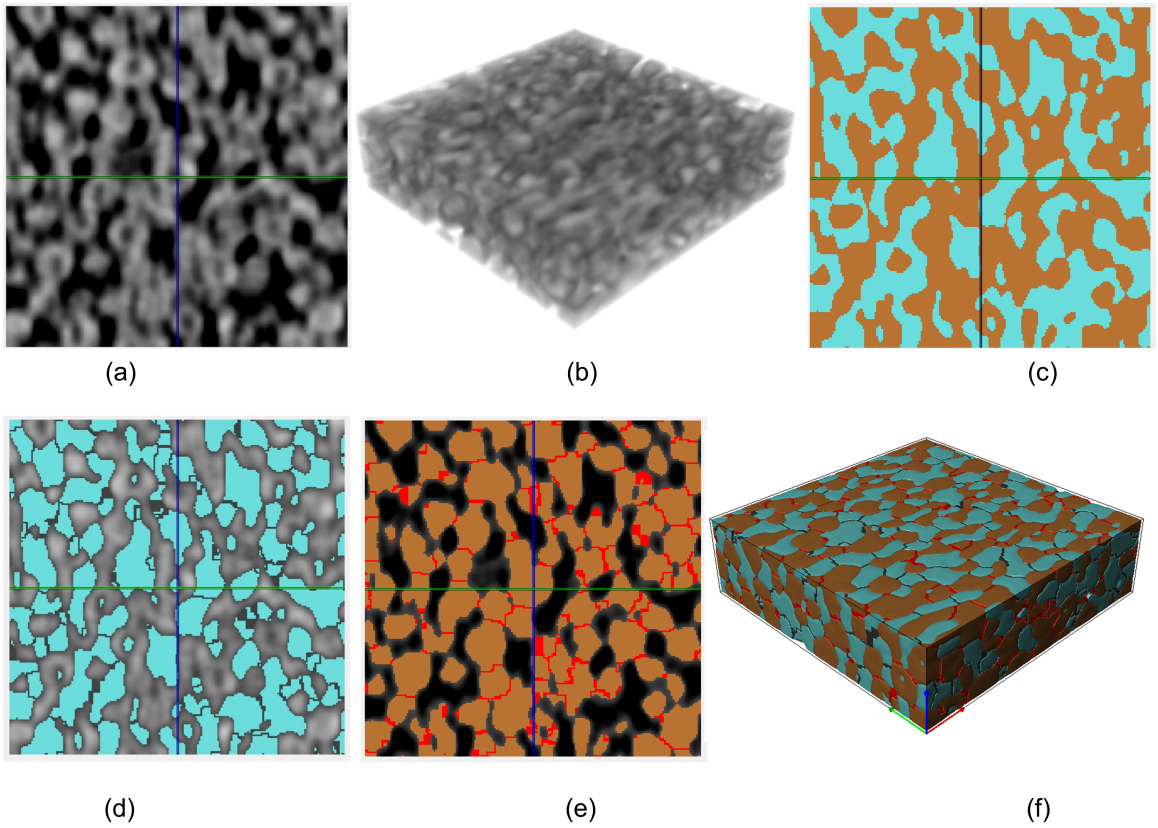

Figure 4.3. Image processing steps showing (a) raw 2D slice from μ-CT scan, (b) 3D reconstructed volume, (c) 2D slice showing pore domain (light blue) and copper regions after thresholding, (d) segmented pore domain, (e) segmented copper domain, and (f) 3D reconstructed volume segmentation in both pore and copper domains. An overall domain size of 800 µm × 800 µm × 207 µm for the spherical particle coating at 39% porosity is shown.

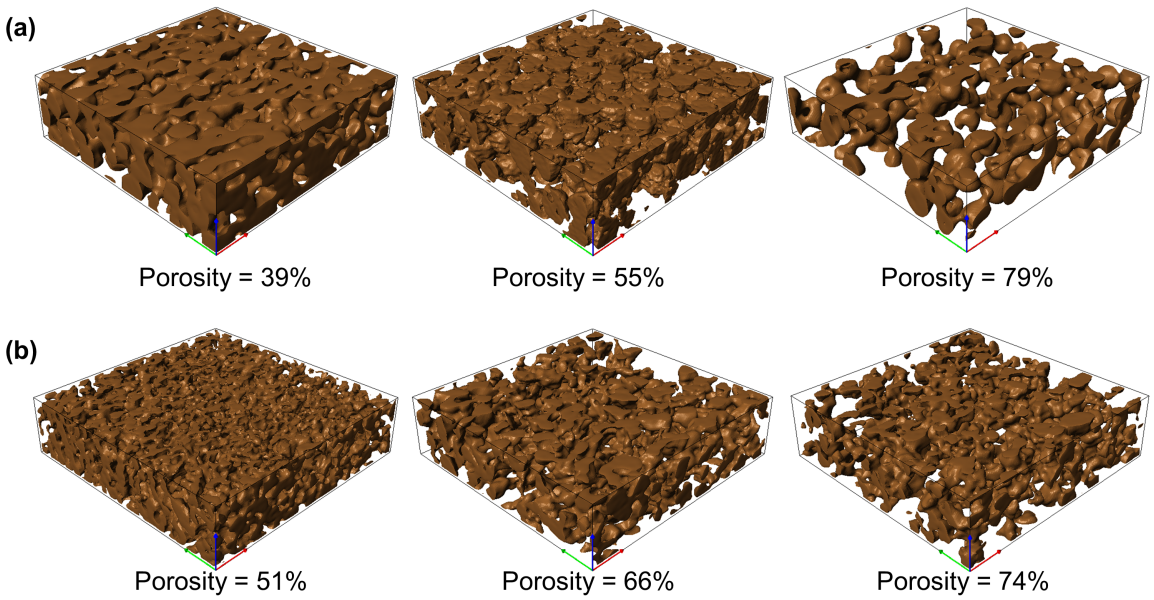

Figure 4.4. 3D reconstructed solid domain (after thresholding) for (a) spherical and (b) irregular coatings at a low, intermediate, and high porosity.

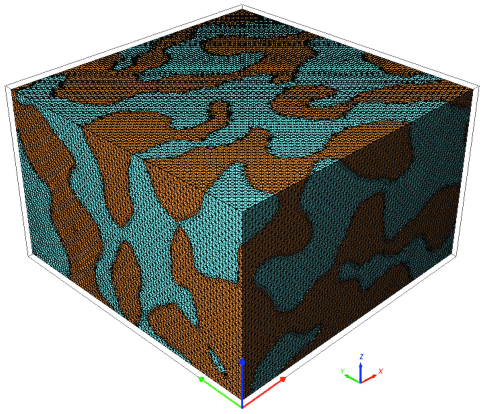

Figure 4.5. Meshed domain (340 µm × 340 µm × 207 µm) for the spherical particle coating at 39% porosity is shown.

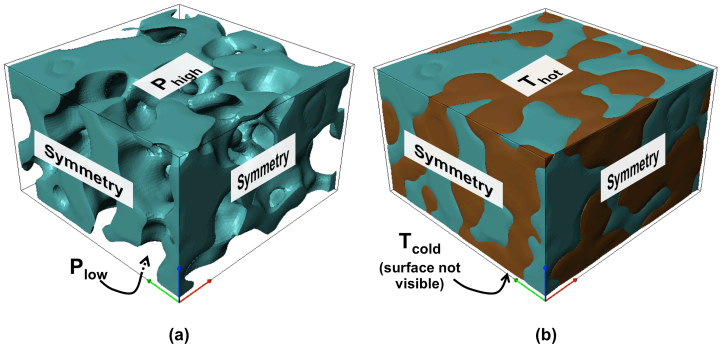

Figure 4.6. Boundary conditions for (a) flow through the pore domain and (b) conduction through copper domain, used to obtain the effective conductivity and effective permeability, respectively.

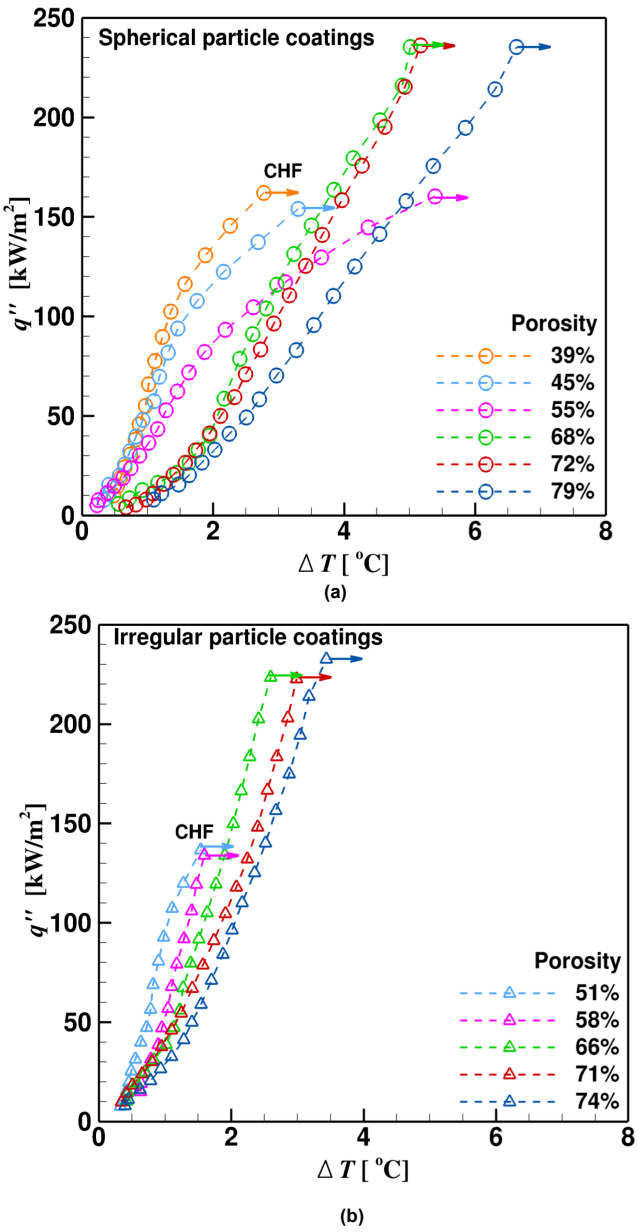

Figure 4.7. Boiling curves of area-averaged heat flux versus wall superheat, ΔT (T_s-T_{sat}), for (a) spherical and (b) irregular particle coatings. Occurrence of CHF is indicated by horizontal arrows.

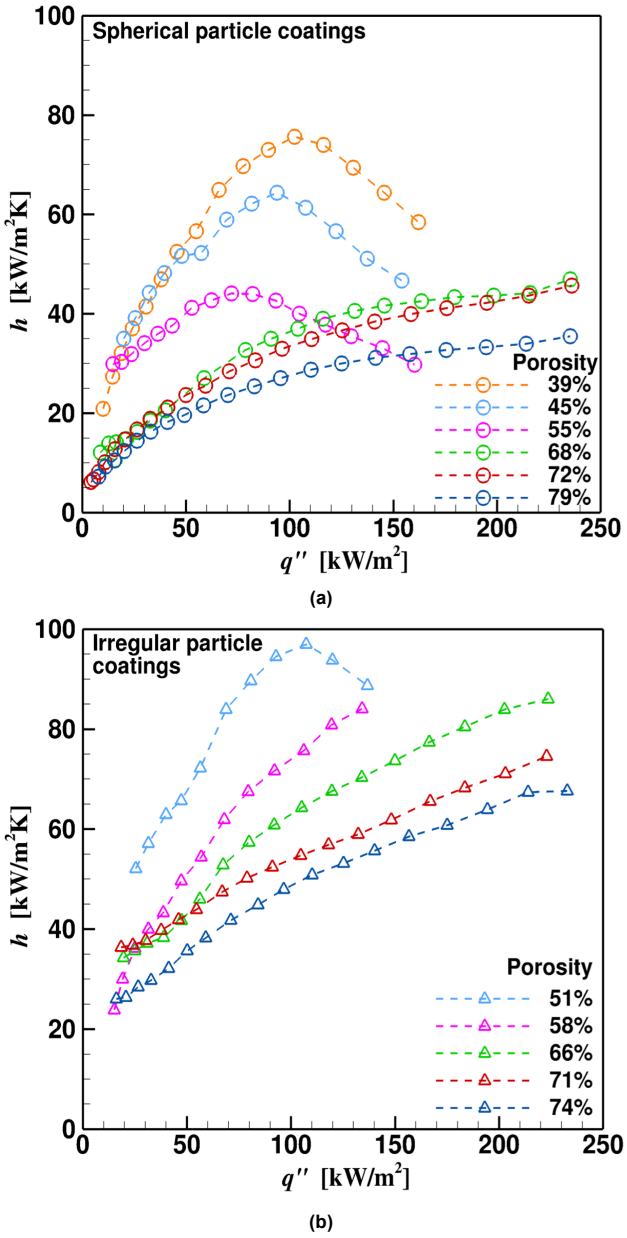

Figure 4.8. Heat transfer coefficient versus area-averaged heat flux for (a) spherical and (b) irregular particle coatings.

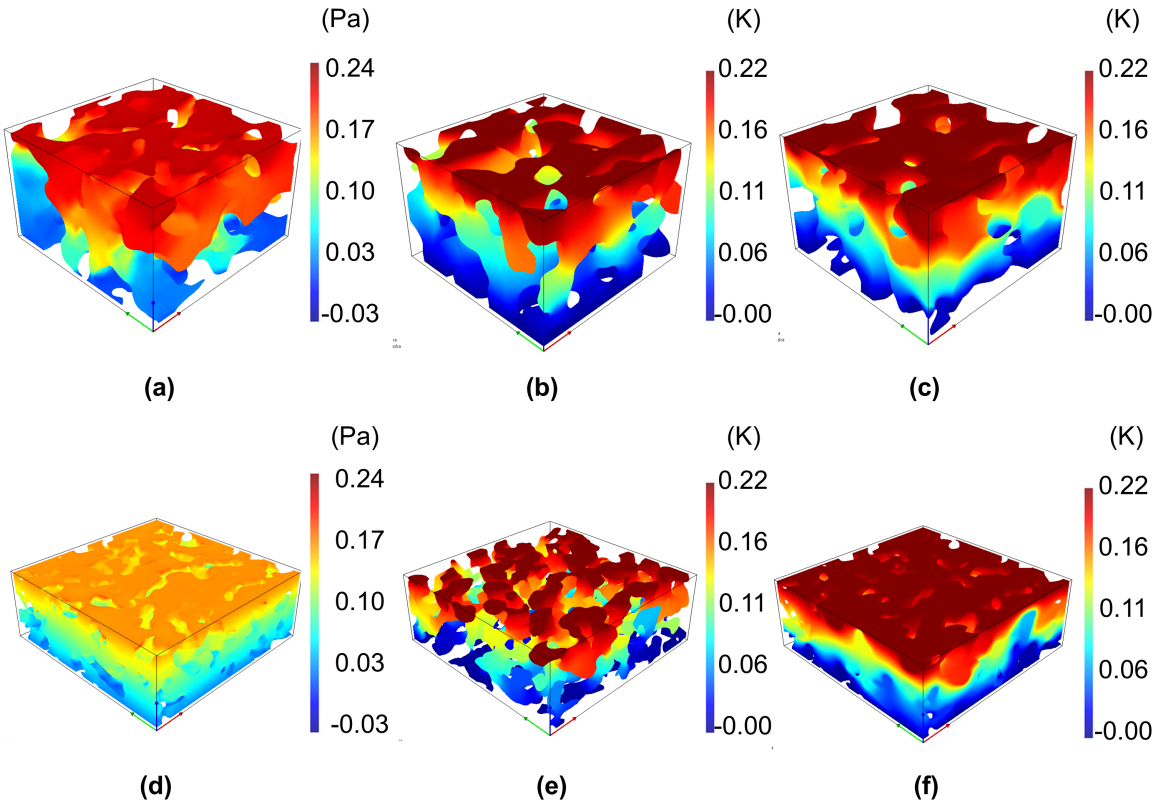

Figure 4.9. Representative contours of (a) pressure field in the pore domain, (b) temperature field in the solid domain and (c) temperature field in the pore domain for the spherical particle coating at 39% porosity. The corresponding contours for irregular particle coatings at 66% porosity are shown in (d–f). The contours are obtained from numerical simulation of the effective permeability and effective thermal conductivity.

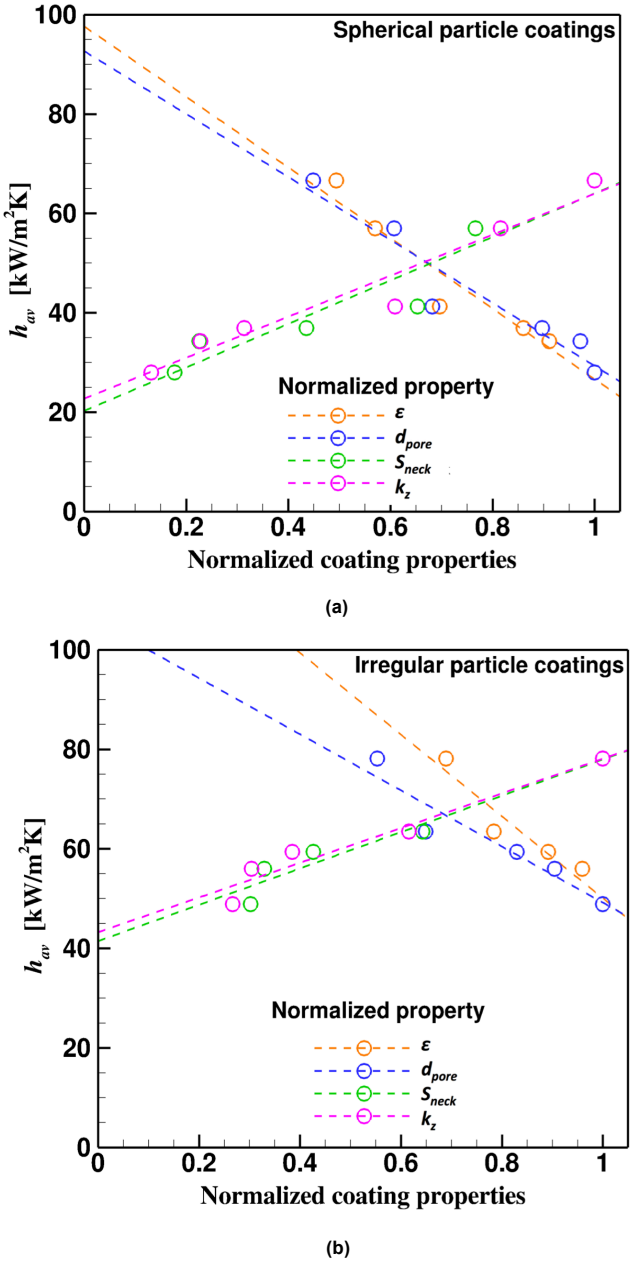

Figure 4.10. Heat transfer coefficient versus normalized critical coating properties for (a) spherical and (b) irregular particle coatings. Each input property is normalized by its maximum value. The markers indicate experimental data points, while the dotted lines indicate a linear fit to the data.

CHAPTER 5. CONCLUSIONS AND FUTURE WORK

The principal objective of this dissertation was to further the understanding of pool boiling heat transfer from enhanced surfaces, so as to target increased heat transfer performance. A wide range of experimental investigations and subsequent quantitative analysis was performed, resulting in both practical and fundamental conclusions regarding characterization of pool boiling heat transfer and effect of coating properties, which were yet to be reported in the literature. This chapter summarizes the primary conclusions from each study in this work, followed by an outline of potential investigations for future work in the field of pool boiling heat transfer enhancement.

5.1 Conclusions

In Chapter 3, an experimental investigation of pool boiling heat transfer enhancement is presented. The effect of particle size on boiling heat transfer performance was analyzed for free-particle and sintered-coating techniques, with all other coating parameters fixed.

- For both free-particle and sintered-coating techniques, the coatings formed by particles in the size range 90-106 μm were observed to exhibit the best boiling heat transfer coefficient at high heat fluxes.

- The 90-106 μm free particles reached 32% lower surface superheat compared to polished surface at 112 kW/m^2, while a 95% reduced wall superheat was observed for sintered particles of the same size range.
- The maximum CHF (161 kW/m^2) was obtained for 45-53 μm free particles, which was 44% higher than that of polished surfaces, while sintered coatings of the same size range reached the same CHF as polished surface.
- A qualitative study of the flow visualizations revealed the differences in bubble behavior that led to the observed difference in boiling performance of sintered coatings, compared to free particles. The higher CHF for free particles was attributed to the actively deformable particle layer that allows escape of trapped vapor bubbles from the surface, while the simultaneous lower heat transfer coefficient was attributed to the reduction in number of active nucleation sites available for pool boiling due to dynamic entrainment of particles into the fluid.
- Despite the differences in the boiling behavior between the two techniques, the trends observed with particle size were notably similar. Since the free-particle technique is easier to implement, it can serve as an efficient indicator of expected parametric trends in boiling performance from sintered surfaces.

In Chapter 4, the analysis of dependence of pool boiling heat transfer performance metrics on sintered coating characteristics, obtained from an experimental investigation followed by a quantitative analysis, is presented. Sintered coatings are fabricated with two different particle morphologies, *viz.*, spherical and irregular, over a wide range of porosities (~40% - 80%), with all other coating parameters fixed. The pool boiling experiments are conducted to study the boiling heat transfer enhancement achieved with

the sintered particle coatings. Image characterization is performed using SEM images and μ-CT to obtain geometric coating properties and numerical simulations are performed to obtain their thermophysical properties.

- The coatings with higher porosities or spherical particles show smaller heat transfer coefficients along the boiling curve compared to coatings with lower porosities or irregular particles.
- The nature of the boiling curve as well as the CHF shows a sharp change at an intermediate porosity, which is clearly explained in terms of the critical coating properties such as pore size distribution, interfacial area, necking area, effective permeability and effective thermal conductivity.
- The coating porosity, pore diameter, unit interfacial area, unit necking area, effective permeability and effective thermal conductivity are observed to be the most significant coating properties affecting the heat transfer coefficient and CHF reached during pool boiling.
- The quantitative dependence of the heat transfer performance metrics on each of the critical coating properties is derived based on regression analysis.
- The high-fidelity characterization of the pore statistics is demonstrated to provide essential insight into the dependence of heat transfer coefficient and CHF on critical coating properties.

5.2 Suggested Future Work

Plans for potential future work are proposed in this section. The overall goal of the proposed investigations is to further augment our understanding of pool boiling heat transfer from enhanced particle-based surfaces, and to analyze the dependence of the boiling performance metrics on parametric coating properties. Future work stemming from each area of this thesis is proposed.

1. From the boiling curves discussed in Chapter 3, clear differences in the heat transfer mechanisms affecting the boiling heat transfer by free-particle and sintered-particle techniques were observed, and a transition was identified, at which free particles start to behave like fixed particle layers. While qualitative explanations are provided for these comparisons, it is desirable to model the bubble dynamics to better understand the effect of the surface-coating technique on the bubble ebullition characteristics. In order to analyze the bubble dynamics for a free-particle coating technique, the particles may be assumed to form a hexagonally close-packed structure and a force balance model may be analyzed between the buoyancy, surface tension, pressure forces, and an opposing weight force on the bubble until it is neutrally buoyant. For free-particle coated surfaces, for ultimate departure of the bubble from the surfaces, the bubble formed in the cavity may be much smaller than the pore size when the force balance predicts departure from the surface without interaction of the vapor embryo with the particles; or, the bubble may grow to a size where it touches the particles before departure. In the second case, the particles will exert an additional resistance

force, such that the net upward force on the particle determines whether the bubble can dislodge the particle form the surface and be entrained into the fluid. The understanding of these bubble dynamics will be crucial to predicting the threshold particle size at which free particles start behaving as fixed.

2. To corroborate the findings from the analytical modeling study, supporting flow visualization experiments need to be performed for a monolayer of free-particle coatings and sintered-particle coatings of different particle sizes to view the single-bubble departure dynamics. The flow visualizations and modeling would enable us to explain the fundamental difference between boiling from free-particle and fixed-particle coatings, predict the particle size at which the transition occurs and understand the wide variation in heat transfer coefficients for the two coating techniques.
3. In Chapter 4, a detailed quantitative regression study was performed to analyze the dependence of the heat transfer coefficient and CHF on the geometric and thermophysical properties of sintered particle coatings, and to identify critical input properties. The combined effect of 3 critical inputs as individual terms in a polynomial model was presented for each output. To further extend the quantitative characterization analysis, it is necessary to study the codependence of the input properties with each other. Using a higher order model other than the polynomial regression used in the present study due to the limited number of data points available, would enable us to then combine the effect of several critical input properties in a single term and thus formulate a predictive correlation of the dependence of heat transfer performance metrics on the critical inputs. Such a

correlation would be very useful in future design of sintered surfaces, tailored to meet the desired heat transfer needs.

LIST OF REFERENCES

LIST OF REFERENCES

[1] A. Z. Mesquita, A. L. Costa, C. Pereira, M. A. F. Veloso and P. A. L. Reis, N. Prabhu, N. Kobasko and S. W. Dean, Experimental investigation of the onset of subcooled nucleate boiling in an open-pool nuclear research reactor, Journal of ASTM International 8 (6) (2011) 103193.

[2] S. J. Thiagarajan, W. Wang, R. Yang, S. Narumanchi and C. King,Enhancement of heat transfer with pool and spray impingement boiling on microporous and nanowire surface coatings, Proceedings of 14th International Heat Transfer Conference, (2010) 13.

[3] Lord Rayleigh, On the pressure developed in a liquid during the collapse of a spherical cavity, Philosophical Magazine 34 (1917) 94-98.

[4] R.L. Webb, Donald Q. Kern Lecture Award Paper: Odyssey of the enhanced boiling surface, Journal of Heat Transfer 126 (2004) 1051-1059.

[5] K. Nishikawa, T. Ito, and K. Tanaka, Enhanced heat transfer by nucleate boiling on a sintered metal layer, Heat Transfer - Japanese Research 8 (2) (1979) 65-81.

[6] R. L. Webb, Nucleate boiling on porous coated surfaces, Heat Transfer Engineering 4 (3-4) (1981) 71-82.

[7] W. Chi, S. Sampath and H. Wang, Ambient and high-temperature thermal conductivity of thermal sprayed coatings, Journal of Thermal Spray Technology 15 (4) (2006) 773-778.

[8] C. T. Hsu and K. W. Wong, Effects of particle shape and configuration on the thermal conductivity of a porous medium, Proceedings of the 10th International Heat Transfer Conference, Vol 6: Heat Transfer Augmentation-Two Phase Flow With and Without Phase Change-Conduction and Insulation, 135 (1994) 367-372.

[9] Y. J. Lin and K. S. Hwang, Effects of powder shape and processing parameters on heat dissipation of heat piper with sintered porous wicks, Materials Transactions, 50 (10) (2009) 2427-2434.

[10] K. K. Bodla, J. Y. Murthy and S. V. Garimella, Direct simulation of thermal transport through sintered wick microstructures, Journal of Heat Transfer 134 (1) (2012) 012602.

[11] H. O' Hanley, C. Coyle, J. Buongiorno, T. McKrell, M. Rubner and R. Cohen, Separate effects of surface roughness, wettability, and porosity on the boiling critical heat flux, Applied Physics Letters 103 (2013) 024102.

[12] C. Y. Han and P. Griffith, The mechanism of heat transfer in nucleate pool boiling—Part I, International Journal of Heat and Mass Transfer 8 (6) (1965) 887-904.

[13] J. Barber, D. Brutin, and L. Tadrist, A review on boiling heat transfer enhancement with nanofluids, Nanoscale Research Letters 6 (1) (2011) 280.

[14] S. J. Kim, I. C. Bang, J. Buongiorno, and L. W. Hu, Effects of nanoparticle deposition on surface wettability influencing boiling heat transfer in nanofluids, Applied Physics Letters 89 (15) (2006) 3107.

[15] S. J. Kim, I. C. Bang, J. Buongiorno, and L. W. Hu, Surface wettability change during pool boiling of nanofluids and its effect on critical heat flux, International Journal of Heat and Mass Transfer 50 (19–20) (2007) 4105–4116.

[16] S. M. You, J. H. Kim, and K. H. Kim, Effect of nanoparticles on critical heat flux of water in pool boiling heat transfer, Applied Physics Letters 83 (16) (2003) 3374.

[17] P. Vassallo, R. Kumar, and S. D'Amico, Pool boiling heat transfer experiments in silica–water nano-fluids, International Journal of Heat and Mass Transfer 47 (2) (2004) 407-411.

[18] G. Hetsroni, J. Zakin, Z. Lin, A. Mosyak, E. Pancallo, and R. Rozenblit, The effect of surfactants on bubble growth, wall thermal patterns and heat transfer in pool boiling, International Journal of Heat and Mass Transfer 44 (2) (2000) 485-497.

[19] S. B. White, A. J. Shih, and K. P. Pipe, Effects of nanoparticle layering on nanofluid and base fluid pool boiling heat transfer from a horizontal surface under atmospheric pressure, Journal of Applied Physics 107 (11) (2010) 4302.

[20] P. J. Berenson, Experiments on pool-boiling heat transfer, International Journal of Heat and Mass Transfer 5 (10) (1962) 985–999.

[21] M. G. Kang, Effect of surface roughness on pool boiling heat transfer, International Journal of Heat and Mass Transfer 43 (22) (2000) 4073–4085.

[22] B. J. Jones, J. P. McHale, and S. V. Garimella, The influence of surface roughness on nucleate pool boiling heat transfer, Journal of Heat Transfer 131 (12) (2009) 1009.

[23] J. P. McHale and S. V. Garimella, Bubble nucleation characteristics in pool boiling of a wetting liquid on smooth and rough surfaces, International Journal of Multiphase Flow 36 (4) (2010) 249-260.

[24] S. M. You, T. W. Simon, and A. Bar-Cohen, A technique for enhancing boiling heat transfer with application to cooling of electronic equipment, IEEE Transactions on Components, Hybrids, and Manufacturing Technology 15 (5) (1992) 823-831.

[25] J. P. O'Connor and S. M. You, A painting technique to enhance pool boiling heat transfer in saturated FC-72, Journal of Heat Transfer 117 (2) (1995) 387.

[26] M. S. El-Genk and J. L. Parker, Enhanced boiling of HFE-7100 dielectric liquid on porous graphite, Energy Conversion and Management 46 (15-16) (2005) 2455-2481.

[27] J. L. Parker and M. S. El-Genk, Enhanced saturation and subcooled boiling of FC-72 dielectric liquid, International Journal of Heat and Mass Transfer 48 (18) (2005) 3736–3752.

[28] A. E. Bergles and M. C. Chyu, Characteristics of nucleate pool boiling from porous metallic coatings, Journal of Heat Transfer 104 (2) (1982) 270.

[29] V. I. Borzenko and S. P. Malyshenko, Mechanisms of phase exchange under conditions of boiling on surfaces with porous coatings, High Temperature 39 (5) (2001) 714–721.

[30] I. H. Chaudhri and I. R. McDougall, Ageing studies in nucleate pool boiling of isopropyl acetate and perchloroethylene, International Journal of Heat and Mass Transfer 12 (6) (1969) 681-688.

[31] C. Li and G. P. Peterson, Parametric study of pool boiling on horizontal highly conductive microporous coated surfaces, Journal of Heat Transfer 129 (11) (2007) 1465.

[32] S. M. Lu and R. H. Chang, Pool boiling from a surface with a porous layer, AIChE Journal 33 (11) (1987) 1813-1828.

[33] L. Chien and C. C. Chang, Experimental study of evaporation resistance on porous surfaces in flat heat pipes, Proceedings of 8th IEEE Intersociety Conference on Thermal and Thermomechanical Phenomena in Electronic Systems (ITherm), San Diego, CA, (2002) 236–242.

[34] J. Y. Chang and S. M. You, Boiling heat transfer phenomena from microporous and porous surfaces in saturated FC-72, International Journal of Heat and Mass Transfer 40 (18) (1997) 4437-4447.

[35] Y. Y. Hsu, On the size range of active nucleation cavities on a heating surface, Journal of Heat Transfer, 84 (3) (1962) 207.

[36] R. Ranjan, J. Y. Murthy, and S. V. Garimella, Bubble dynamics during capillary-fed nucleate boiling in porous media, Proceedings of 13th IEEE Intersociety Conference on Thermal and Thermomechanical Phenomena in Electronic Systems (ITherm), San Diego, CA, (2012) 1114–1126.

[37] T.Y. Kim and S.V. Garimella, Investigation of boiling heat transfer in water using a free-particles-based enhancement technique, International Journal of Heat and Mass Transfer 71 (2014) 818-828.

[38] T.Y. Kim, J.W. Weibel, and S.V. Garimella, A free-particles-based technique for boiling heat transfer enhancement in a wetting liquid, International Journal of Heat and Mass Transfer 71 (2014) 808-817.

[39] A. G. Dixon, Wall and particle-shape effects on heat transfer in packed beds, Chemical Engineering Communication 71 (1988) 217–237.

[40] D. Deng, Y. Tang, H. Shao, J. Zeng, W. Zhou and D. Liang, Effects of structural parameters on flow boiling performance of reentrant porous microchannels, Journal of Miromechanics and Microengineering 24 (6) (2014).

[41] J. Bear, Dynamics of Fluids in Porous Media, Dover Publications, New York, (1988).

[42] K. Vafai, Handbook of porous media, Third edition Taylor & Francis Group, CRC Press, Boca Raton, FL (2015).

[43] R. Ranjan, J. Y. Murthy, S. V. Garimella and U. Vadakkan, A numerical model for transport in flat heat pipes considering wick microstructure effects, International Journal of Heat and Mass Transfer 54 (1-3) (2011) 153–168.

[44] K. K. Bodla, J. A. Weibel and S. V. Garimella, Advances in fluid and thermal transport property analysis and design of sintered porous wick microstructures, Journal of Heat Transfer 135 (6) (2013) 061202.

[45] A. A. Aziz, C. Saury, V. B. Xuan and P. Young, On the material characterization of a composite using micro CT image based finite element modeling, Journal of Biomechanics 38 (1) (2005).

[46] I. G. Watson, P. D. Lee, R. J. Dashwood and P. Young, Simulation of the mechanical properties of an aluminum matrix composite using X-ray microtomography, Metallurical and Materials Transactions A 37 (3) (2006) 551–558.

[47] G. Tabor, P. G. Young, T. B. West and A. Benattayallah, Mesh construction from medical imaging for multiphysics simulation: Heat transfer and fluid flow in complex geometries, Engineering Applications of Computational Fluid Mechanics 1 (2) (2007) 126–135.

[48] K. K. Bodla, J. Y. Murthy and S. V. Garimella, Microtomography-based simulation of transport through open-cell metal foams, Numerical Heat Transfer Part A 58 (7) (2010) 527–544.

[49] K. K. Bodla, J. Y. Murthy and S. V. Garimella, Direct simulation of thermal transport through sintered wick microstructures, Journal of Heat Transfer 134 (1) (2012) 012602.

[50] S. Sarangi, J. A. Weibel and S. V. Garimella, Effect of particle size on surface coating-based enhancement of pool boiling heat transfer, International Journal of Heat and Mass Transfer 81 (2015) 103-113.

[51] 3M Corporation, Fluorinert Electronic Liquid FC-72 Product Information 98-0212-2308-0 (HB), Specialty Materials Division, (2000).

[52] G. W. Burns, M. G. Scroger, G. F. Strouse, M. C. Croakin and W. F. Guthrie, NIST Monograph 175, Temperature-Electromotive Force Reference Functions and Tables for the Letter-Designated Thermocouple Types Based on the ITS-90, (1993).

[53] K. Brown, H. Coleman, and W. Steele, Estimating uncertainty intervals for linear regression, Proceedings of the 33rd Aerospace Science Meeting and Exhibit, Reno, NV, (1995).

[54] J. Ospina and E. Canuto, Uncertainty on differential measurements and its reduction using the calibration by comparison method, Metrologia 45 (4) (2008) 389-394.

[55] J. A. Weibel, S. Sarangi and S. V. Garimella, Pool boiling heat transfer from deformable particulate beds, Journal of Heat Transfer 135 (8) (2013) 080908.

[56] H. D. Kim and M. H. Kim, Effect of nanoparticle deposition on capillary wicking that influences the critical heat flux in nanofluids, Applied Physics Letters 91 (1) (2007) 4104.

[57] C. Li and G. P. Peterson, Experimental studies on CHF of pool boiling on horizontal conductive micro porous coated surfaces, AIP Conference Proceedings, 969 (1) (2008) 12-20.

[58] R. G. Scurlock, Enhanced boiling heat transfer surfaces, Cryogenics 35 (4) (1995) 233–237.

[59] S. Sarangi, J. A. Weibel and S. V. Garimella, Quantitative evaluation of the dependence of pool boiling heat transfer enhancement on sintered-particle coating characteristics, Journal of Heat Transfer (in review).

[60] J. R. Davis, Copper and Copper Alloys (ASM Specialty Handbook), Materials Park, Ohio: ASM International, (2001) 222-241.

[61] G. S. Upadhyaya, Powder Metallurgy Technology, Cambridge, England: Cambridge International Science Publishing, (2002) 18-21.

[62] Y. Y. Zhao, T. Fung, L. P. Zhang and F. L. Zhang, Lost carbonate sintering process for manufacturing metal foams, Scripta Materialia 52 (2005) 295–298.

[63] ScanIP, ScanFE, and ScanCAD Tutorial Guide for SIMPLEWARE 7.0, Simpleware Ltd., Exeter, UK, (2009).

[64] MATLAB 8.3, The MathWorks Inc., Natick, Massachusetts, 2014a.

[65] J. L. Devore, Probability and Statistics for Engineering and the SciencesBrooks/Cole Cengage Learning, Brooks/Cole Cengage Learning, Belmont, CA, (2009).

[66] K. H. Esbensen, D. Guyot, F. Westad and P. Lars, Multivariate Data Analysis - in Practice: An Introduction to Multivariate Data Analysis and Experimental Design, CAMO, Oslo, Norway, (2002).

[67] J. P. McHale, S. V. Garimella, T. S. Fisher and G. A. Powell, Pool boiling performance comparison of smooth and sintered copper surfaces with and without carbon nanotubes, Nanoscale and Microscale Thermophysical Engineering 15 (3) (2011) 133–150.

[68] Y. V. Polezhaev and S. A. Kovalev, Modeling heat transfer with boiling on porous structures, Thermal Engineering 37 (12) (1990) 617–620.

[69] E. C. Childs and N. Collis-George, The permeability of porous materials, Proceedings of the Royal Society A: Mathematical, Physical and Engineering Sciences 201 (1066) (1950) 392–405.

[70] R. J. Millington and J. P. Quirk, Permeability of porous solids, Transactions of the Faraday Society 57 (1961) 1200.

[71] T. J. Marshall, A relation between permeability and size distribution of pores, Journal of Soil Science 9 (1) (1958) 1–8.

[72] Z. Hashin and S. Shtrikman, A variational approach to the theory of the effective magnetic permeability of multiphase aterials, Journal of Applied Physics 33 (10) (1962) 3125.

[73] R. Landauer, The electrical resistance of binary metallic mixtures, Journal of Applied Physics 23 (7) (1952) 779.

[74] S. Kirkpatrick, Percolation and conduction, Reviews of Modern Physics 45 (4) (1973) 574–588.

[75] D. Liu and Garimella S.V., Analysis and optimization of the thermal performance of microchannel heat sinks, International Journal of Numerical Methods for Heat and Fluid Flow 15 (1) (2004) 7–26.

[76] K. K. Bodla, J. Y. Murthy, and S. V. Garimella, Optimization under uncertainty applied to heat sink design, ASME Journal of Heat Transfer 135 (2013).

[77] D. Xiu and G. E. Karniadakis, The Wiener-Askey polynomial chaos for stochastic differential equations, SIAM Journal on Scientific Computing 24 (2) (2002) 619–44.

[78] S. Sarangi, K. K. Bodla, S. V. Garimella and J. Y. Murthy, Manifold microchannel heat sink design using optimization under uncertainty, International Journal of Heat and Mass Transfer 69 (2014) 92-105.

[79] D. B. Tuckerman and R.F.W. Pease, High-performance heat sinking for VLSI, IEEE Electron Device Letters 2 (1981) 126–129.

[80] S. V. Garimella and T. Harirchian, Microchannel Heat Sinks for Electronics Cooling, Vol. 1 in the Encyclopedia of Thermal Packaging, World Scientific, Singapore, (2013), pp. 248.

[81] K. Vafai and L. Zhu, Analysis of two-layered microchannel heat sink concept in electronic cooling, International Journal of Heat and Mass Transfer 42 (1999) 2287–2297.

[82] J. H. Ryu, D.H. Choi, and S.J. Kim, Numerical optimization of the thermal performance of a microchannel heat sink, International Journal of Heat and Mass Transfer 45 (2002) 2823–2827.

[83] P. S. Lee and S. V. Garimella, Thermally developing flow and heat transfer in rectangular microchannels of different aspect ratios, International Journal of Heat and Mass Transfer 49 (17) (2006) 3060–3067.

[84] T. C. Hung, W. M. Yan, X. D. Wang, and Y. X. Huang, Optimal design of geometric parameters of double-layered microchannel heat sinks, International Journal of Heat and Mass Transfer 55 (2012) 3262–3272.

[85] T. C. Hung and W. M. Yan, Optimization of a microchannel heat sink with varying channel heights and widths, Numerical Heat Transfer-Part A 62 (2012) 722–741.

[86] G. M. Harpole and J. E. Eninger, Micro-channel heat exchanger optimization, in Proceedings of the 7th IEEE Semiconductor Thermal Measurement and Management Symposium, (1991), pp. 59–63.

[87] E. Kermani, Manifold micro-channel cooling of photovoltaic cells for high efficiency solar energy conversion, M.S. Thesis, University of Maryland, (2008).

[88] E. Kermani, S. Dessiatoun, A. Shooshtari, and M. M. Ohadi, Experimental investigation of heat transfer performance of a manifold microchannel heat sink for cooling of concentrated solar cells, Proceedings of the 59th Electronic Components and Technology Conference, (2009), 453–459.

[89] D. Copeland, H. Takihara, and W. Nakayama, Manifold microchannel heat sinks: theory and experiments, Thermal Science and Engineering 3 (2) (1995) 9–15.

[90] Y. I. Kim, W.C. Chun, J.T. Kim, B.C. Pak, and B.J. Baek, Forced air cooling by using manifold microchannel heat sinks, KSME International Journal 12 (4) (1998) 709–718.

[91] D. Copeland, M. Behnia, and W. Nakayama, Manifold microchannel heat sinks: isothermal analysis, IEEE Transactions on Components, Packaging, and Manufacturing Technology: Part A 20 (1997) 96–102.

[92] J. Ryu, D. Choi, and S. Kim, Three-dimensional numerical optimization of a manifold microchannel heat sink, International Journal of Heat and Mass Transfer 46 (2003) 1553–1562.

[93] M. S. Eldred, A. A. Giunta, S. F. Wojtkiewicz Jr, and T. G. Trucano, Formulations for surrogate-based optimization under uncertainty, in Proceedings of the 9th AIAA/ISSMO Symposium on Multidisciplinary Analysis and Optimization, (2002) 4–6.

[94] F. P. Incropera and D. P. De Witt, Fundamentals of Heat and Mass Transfer, Singapore: John Wiley & Sons (Asia).

[95] W. Escher, B. Michel, and D. Poulikakos, A novel high performance, ultra thin heat sink for electronics, International Journal of Heat and Fluid Flow 31 (4) (2010) 586–598.

[96] T. CUBIT, CUBIT 10.0 User's Manual, Sandia National Laboratories, Albuquerque, NM, (2005).

[97] User's Guide for ANSYS FLUENT 14.0. Fluent Inc., (2011).

[98] M. Kaviany, Principles of Heat Transfer in Porous Media, 1st ed. New York: Springer-Verlag, (1991).

[99] S. J. Kim and D. Kim, Forced convection in microstructure for electronic equipment cooling 121 (1999) 639–45.

[100] M. S. Eldred, Recent advances in non-intrusive polynomial chaos and stochastic collocation methods for uncertainty analysis and design, in 50th AIAA/ASME/ASCE/AHS/ASC Structures, Structural Dynamics and Materials Conference, Palm Springs, CA, United States, May (2009).

[101] I. M. Sobol and S. Kucherenko, Derivative based global sensitivity measures and their link with global sensitivity indices, Mathematics and Computers in Simulation 79 (10) (2009) 3009–3017.

[102] M. S. Eldred, A. A. Giunta, B. G. van Bloemen Waanders, S. F. Wojtkiewicz, W. E. Hart, and M. P. Alleva, DAKOTA, a multilevel parallel object-oriented framework for design optimization, parameter estimation, uncertainty quantification, and sensitivity analysis: version 4.1 reference manual, Sandia National Laboratories Albuquerque, NM, (2007).

[103] G. N. Vanderplaats, CONMIN, a FORTRAN program for constrained function minimization: user's manual 62282. Ames Research Center and US Army Air Mobility R&D Laboratory, 1973.

[104] P. R. Bevington and D. K. Robinson, Data Reduction and Error Analysis for the Physical Sciences, 2nd. ed. McGraw-Hill: New York, (1992).

[105] S. Sarangi, J. A. Weibel and S. V. Garimella, Effect of particle morphology on pool boiling from surfaces coated with sintered particles, Proceedings of the ASME International Mechanical Engineering Congress and Exposition 8A (2015), Houston, Texas.

APPENDICES

APPENDIX A. MANIFOLD MICROCHANNEL HEAT SINK DESIGN USING OPTIMIZATION UNDER UNCERTAINTY

This chapter presents the study of optimization under uncertainty for manifold microchannel (MMC) heat sinks. The objective of the present study is to optimize the geometry of a manifold microchannel heat sink based on a probabilistic approach to account for the inherent uncertainties in fabrication and operating conditions. A 3-D numerical unit-cell model for the MMC heat sink is first developed and validated by comparing against previous experimental results in the literature. The geometric parameters and input conditions for the model are similar to those used in the experiments. Further, a 3-D porous-medium model is also developed to perform a system level analysis and optimization. In this model, the microchannel heat sink is represented as a porous medium with equivalent porosity and permeability [75], so as to reduce computational complexity. After validating the numerical model, an OUU analysis is performed by using a nested approach as discussed in detail in [76]. In this approach, uncertainty quantification is performed in an inner loop, which is nested within an outer optimization loop, as described in Section A.3.2.

The cost incurred by multiple CFD simulations is alleviated by using a generalized polynomial chaos (gPC) based response surface approach for the inner loop UQ [77]. Robust optimal designs, restricting the standard deviation of the output – the heat transfer coefficient – are obtained for a variety of cases. Further, the computed results are compared against those obtained via a traditional deterministic approach, *i.e.,* an optimization study with mean values assumed for the uncertain variables. The OUU analysis is also performed for the porous-medium model using the same geometric

parameters and optimization conditions and constraints, and the results are compared against those obtained from the probabilistic optimization using the unit-cell model. The material presented in this chapter was published in the *International Journal of Heat and Mass Transfer* [78].

A.1 Introduction

Forced convection cooling in microchannels is widely used as a heat transfer enhancement technology for electronics cooling. Conventional microchannel heat sinks are characterized by long microchannels that run parallel to the base of the heat sink, as proposed by Tuckerman and Pease [79], and shown in Figure A.1 (a). These microchannel heat sinks have been successfully investigated for use in electronics cooling applications [80]. Several analytical and numerical models for predicting pressure drop and heat transfer through such heat sinks have been proposed in the literature [81-83]. Although conventional microchannels provide substantial heat transfer augmentation, they are also associated with very high pressure drops. Microchannel heat sinks with various modified configurations have been previously studied for improved performance over conventional single-layered rectangular microchannels. Deterministic optimization studies have been performed on microchannel heat sinks with double-layered channels [84] and tapered channels [85] to obtain optimum geometric parameters. An alternative configuration that has been proposed to lower the incurred pressure drop while simultaneously increasing the heat transfer is the manifold microchannel (MMC) heat sink, as shown in Figure A.1 (b). An MMC heat sink consists of a manifold system,

which distributes the coolant via multiple inlet-outlet pairs, thereby reducing the flow length of the coolant through the microchannels, as shown in Figure A.2 (a). Such an arrangement results in a significant reduction in the pressure drop, while also reducing the thermal resistance by interrupting the growth of thermal boundary layers. This design was originally proposed by Harpole and Eninger [86], who demonstrated a significant reduction in thermal resistance relative to conventional microchannel heat sinks at a constant pumping power. Their MMC system consisted of 10 to 30 manifolds spanning the entire flow length. Kermani [87] and Kermani *et al.* [88] performed experiments to demonstrate the use of MMC heat sinks to cool concentrated solar cells, and reported a significant increase in heat transfer coefficient as compared to conventional microchannel heat sinks of similar dimensions. Experimental investigations were also reported by Copeland *et al.* [89] who observed the thermal resistance to be inversely proportional to the volume flow rate of the coolant. Kim *et al.* [90] demonstrated a 35% reduction in thermal resistance relative to a conventional arrangement for forced air cooling. Copeland *et al.* [91] conducted a simplified 1D analysis to predict the pressure drop and thermal resistance of MMC heat sinks based on correlations for a straight rectangular channel. This analytical model was reasonably accurate at high flow rates, but was found to be inadequate for the geometry under consideration at low flow rates. The thermal resistance obtained using the analytical model was found to be about 50 – 70% lower than that predicted using a simplified 3-D isothermal numerical model. Ryu *et al.* [92] performed a detailed 3-D numerical analysis for quantifying the thermal performance of an MMC heat sink configuration, and included a consideration of the manifold depth and the bottom solid wall which were previously excluded from analysis [91]. Further, an

optimization study was also performed using the steepest-descent method for arriving at the optimal design that would yield the minimum thermal resistance at different pumping powers. It was observed that the optimal geometric parameters as well as the optimal thermal resistance had a power-law dependence on the pumping power.

Microchannel-based heat sinks involve uncertainties in a number of parameters, such as those due to inherent limitations of the fabrication technique, and in the operating conditions such as the inlet flow rate and the input heat fluxes. In the presence of such uncertainties, a conventional, deterministic optimization approach may not provide a truly optimized design that is also robust. The challenge is to quantify these uncertainties and include them in the optimization procedures to produce designs meeting the desired reliability and robustness levels. The typical approach in the presence of such uncertainties is to perform an optimization by considering the uncertain variables as design parameters fixed at their mean values (or at bounds), and then include a post-design factor of safety to produce a conservative design that accounts for uncertainties heuristically. However, in the presence of large uncertainties or when there are strict constraints (such as expensive design parts, designs with constraints on overall mass, etc.), this approach fails to produce a truly optimal design. Instead, it merely provides a heuristic, conservative estimate and does not involve explicit quantification of the output uncertainties relative to input uncertainties.

An improved alternative strategy is to adopt a probabilistic optimization approach using the optimization under uncertainty (OUU) method, which combines the optimization procedure with uncertainty quantification (UQ) [76]. Optimization under uncertainty is a powerful approach that ensures reliable design of systems by considering the input

uncertainties as part of the design process. The OUU approach may be used for "design for reliability" and for "design for robustness" [93]. The goal of the former problem is to produce an optimized design with a reduced probability of failure, while in the latter case, the objective is to produce designs that are less sensitive to variable inputs. As discussed by Eldred *et al.* [93], the latter problem is often the simpler one to address and does not always require UQ. However, non-UQ-based approaches rely on local derivatives to assess robustness and are hence not recommended. In the design for reliability problem, UQ is performed and design parameters are estimated based on the tail (end) statistics of the output probability density function (PDF). This problem places a greater demand on the UQ and is often computationally more expensive compared to the design for robustness problem.

In summary, manifold microchannel heat sinks provide an efficient alternative to conventional microchannel heat sinks by distributing flow in a manner that drastically reduces the flow lengths and associated pressure drop. The inherent uncertainties associated with fabrication of microchannels affect the output performance of such heat sinks. In order to optimize the MMC heat sinks to yield the maximum heat transfer coefficients and minimum pressure drop, it is essential to account for the effects of the uncertainties adequately, so as to obtain a robust and reliable optimal design.

A.2 Numerical Modeling

This section describes the numerical modeling approach employed in the current work. The models are described only briefly here, and a detailed discussion on the UQ

and OUU methodology employed may be found in Bodla *et al.* [76]. In the present study, two sets of computations are performed. In the first, a unit-cell domain is employed for a detailed numerical analysis of the fluid-flow and heat transfer, and the results are compared with past experiments; the performance of the unit cell is optimized using traditional deterministic as well as the probabilistic (OUU) approaches discussed above. Following this, a complete system-level analysis is also performed using a porous-medium model, wherein the simulations are performed over several microchannels throughout the length of one manifold. A porous-medium treatment of the microchannel heat sink is employed in this analysis using a two-temperature non-thermal equilibrium model. The two kinds of computations are discussed below.

A.2.1 Unit-Cell Model

A schematic diagram of the MMC heat sink considered in the present work is shown in Figure A.2 (a). The manifold distribution system is placed on top of the microchannels, in a direction transverse to the main flow direction. The coolant is pumped in through a common inlet port, which branches out into parallel manifold inlet channels. Upon entering the microchannel, the fluid undergoes a 90-degree turn, traverses along the microchannel length removing heat from the substrate, and subsequently flows through another 90-degree turn and then exits upward through the outlet manifold channels and into the common outlet port. Exploiting symmetry and periodicity, only a unit cell of the MCC heat sink is considered for detailed numerical analysis. Figure A.2 (b) shows the unit cell employed, along with the applicable boundary conditions. The continuity,

momentum, and energy equations for steady-state, laminar, incompressible flow with constant thermophysical properties may be written as [94]:

$$\frac{\partial}{\partial x_j}\left(\rho u_j\right)=0 \tag{A.1}$$

$$\frac{\partial}{\partial x_j}\left(\rho u_j u_i\right)=-\frac{\partial P}{\partial x_i}+\frac{\partial}{\partial x_j}\left(\mu_f \frac{\partial u_i}{\partial x_j}\right) \tag{A.2}$$

$$\frac{\partial}{\partial x_j}\left(\rho u_j C_p T_f\right)=\frac{\partial}{\partial x_j}\left(k_f \frac{\partial T_f}{\partial x_j}\right)(liquid) \tag{A.3}$$

$$0=\frac{\partial}{\partial x_j}\left(k_s \frac{\partial T_s}{\partial x_j}\right) \qquad (solid) \tag{A.4}$$

Here u_j, P, and T represent the velocity, pressure and temperature fields, while the subscripts s and f refer to the solid and fluid medium, respectively. Without loss of generality, water is used as the coolant in the current study and the walls of the microchannel and manifold are assumed to be made of silicon. The low Reynolds numbers considered for the flow justify the assumption of laminar, steady flow.

At the inlet, a constant mass flow condition is specified with the fluid entering at a constant temperature of T_{in} = 300 K, while a constant pressure condition is imposed at the outlet. Symmetry conditions are specified for both velocity and temperature at the four outer boundary planes, *i.e.*, at $x = 0$, $x = x_{max}$, and at $z = 0$, and z = z_{max}. A uniform heat flux of q_w" = 100 W/cm^2 [92] is specified on the bottom wall of the substrate, while the top wall of the manifold is assumed to be adiabatic. Also, as the problem involves conjugate heat transfer, continuity of temperature and heat flux is employed at all the solid-fluid interfaces, as given by [95].

$$T_{s,\text{int}} = T_{f,\text{int}} \tag{A.5}$$

$$-k_s\left(\frac{\partial T_s}{\partial n}\right)_{\text{int}} = -k_f\left(\frac{\partial T_f}{\partial n}\right)_{\text{int}} \tag{A.6}$$

The geometry is modeled and meshed using the mesh generation package CUBIT [96] . The governing equations along with the boundary conditions described are solved using the commercial CFD package FLUENT [97]. Pressure-velocity coupling is addressed via the SIMPLE algorithm, along with an algebraic multigrid algorithm (AMG) for solving the linearized system of governing equations. The governing equations are solved using a first-order upwind scheme to obtain an approximate solution that is employed as the initial condition for a more accurate, second-order upwind scheme analysis. The number of iterations for this initial first-order solution were chosen by observing the overall time reduction achieved relative to a purely second-order scheme without a precursor first-order solution. Allowing the scaled residuals with the initial first-order scheme to converge close to the final convergence criteria employed reduced the number of second-order iterations required. As a comparison, the overall solution time with this approach was observed to be approximately 60% of that required with just the second-order scheme employed from the beginning. Employing the flow and temperature fields so obtained as the initial conditions, the equations are then solved using a second-order upwind scheme until convergence, to obtain more accurate converged solutions. The use of the initial conditions obtained from the first-order scheme reduces the computational time required for second order convergence. The equations are also suitably under-relaxed, and convergence criteria of 10^{-6} for scaled residuals of continuity and momentum equations, and 10^{-9} for energy equation are specified. In addition, the average

pressure at the inlet and the average temperature of the bottom wall are also monitored to check for convergence of the flow and energy equations.

A.2.2 Porous-Medium Model

Unit-cell models, though accurate, have certain limitations. First, owing to the underlying assumptions of periodicity, non-uniform heat fluxes such as those encountered in a realistic scenario cannot be incorporated. Second, modeling the entire heat sink using such an approach is not computationally feasible. In lieu of these limitations, a porous-medium model was developed for a system level flow and heat transfer analysis and optimization of the manifold microchannel heat sink.

Microchannel heat sinks have previously been modeled as equivalent porous medium successfully [75]. In this approach, the hydrodynamic performance of the heat sink is modeled via an equivalent permeability and porosity, without the need to resolve the heat sink geometry down to scale of individual fins and channels. For the current configuration, shown in Figure A.2 (c), we employ the following parameters described in Liu and Garimella [75]:

$$\varepsilon = \frac{W_c}{W_c + W_{fin}}$$
$$\kappa_{y,z} = \frac{\varepsilon W_c^2}{12} \; ; \; \kappa_x = \frac{\kappa_{y,z}}{100} \tag{A.7}$$

In these definitions, ε denotes the porosity of the microchannel and W_{fin} is the width of the fin, which in this study is assumed equal to the width of the microchannel, W_c. The permeability is anisotropic and is denoted by κ. The permeability in the x-direction,

transverse to the main flow direction, is assumed to be lower by two orders of magnitude relative to the value in the flow direction (y and z) so as to account for the impermeable walls of the microchannel. Further, the complexity of the problem is reduced by excluding the bottom wall of the heat sink (included in the unit-cell model) from the computational domain for the porous-medium model. The implications of this change are described in Section A.4.1.2. The hydrodynamic performance of such a porous medium may be modeled using Navier-Stokes equations in conjunction with Darcy's equation, as discussed in Escher *et al.* [95]:

$$\frac{\partial}{\partial x_j}\left(\rho_f u_j u_i\right) = -\frac{\partial P}{\partial x_i} + \frac{\partial}{\partial x_j}\left(\mu_f \frac{\partial u_i}{\partial x_j}\right) - \frac{\mu_f}{\kappa_i} u_i \tag{A.8}$$

Here, μ_f is the viscosity of the fluid. The last term on the right hand side of Eq (A.8) denotes the additional viscous pressure drop (Darcy pressure drop), owing to the presence of the solid microchannel walls.

The thermal performance of the porous medium can be modeled using the two-temperature model as discussed by Kaviany [98] and Kim and Kim [99]. In this work, we employ this two-temperature model to account for the local thermal non-equilibrium between the solid and fluid phases within the control volume of the porous medium. The energy equations for the solid and fluid phases of the porous medium are thus modeled as follows:

$$k_{se}\frac{\partial^2\left\langle T\right\rangle_s}{\partial y^2}=h_{sf}a_{sf}\left(\left\langle T\right\rangle_s-\left\langle T\right\rangle_f\right) \tag{A.9}$$

$$\varepsilon\rho_f C_{p,f}u_f\frac{\partial\left\langle T\right\rangle_f}{\partial x}=h_{sf}a_{sf}\left(\left\langle T\right\rangle_s-\left\langle T\right\rangle_f\right)+k_{fe}\frac{\partial^2\left\langle T\right\rangle_f}{\partial y^2} \tag{A.10}$$

$$k_{se}=\left(1-\varepsilon\right)k_s;\ k_{fe}=\varepsilon k_f \tag{A.11}$$

Here, a_{sf} is the wetted surface area per unit volume, while k_{se} and k_{fe} are the effective thermal conductivities of the solid and fluid phases, respectively [75]. The volume-averaged temperatures of the solid and fluid phases are represented by $<T>_s$ and $<T>_f$, respectively. The right hand side of Eq (A.10) represents the interfacial heat transfer and may be modeled via a suitable value for the interfacial heat transfer coefficient, h_{sf}. In this study, we employ a developing flow correlation for single-phase heat transfer in microchannels proposed by Lee and Garimella [83]. The interfacial heat transfer coefficient and the Nusselt number are dependent on location in the flow direction, and are given as follows:

$$\begin{aligned} h_{sf,z}&=\frac{Nu_z k_f}{D_h}\\ Nu_z&=\frac{1}{C_1\left(z^*\right)^{C_2}+C_3}+C_4 \end{aligned} \tag{A.12}$$

In this equation, z^* denotes the non-dimensional axial distance from the inlet, and C_1, C_2, C_3 and C_4 are empirical constants. The values of the empirical constants, and details on limitations and applicability of the correlation may be found in Lee and Garimella [83].

The computational domain shown in Figure A.2 (c) is meshed using the mesh generation package CUBIT [96] . Again, exploiting symmetry, the computational domain consists

of one half each of an inlet and outlet manifold in the flow direction, while the entire heat sink length is considered in the transverse direction. The use of such a porous-medium model allows a system-level analysis with reduced geometrical complexity, thereby providing greater flexibility at significantly reduced computational cost, as will be discussed in Section A.4.1.2. A constant mass flux boundary condition is applied at the inlet, while a constant pressure condition is imposed at the outlet. Further, a constant heat flux boundary condition is applied on the bottom wall of the microchannel section, simulating the heat source. All other interfaces are assumed to have a no-slip boundary condition along with temperature and heat flux continuity between the solid and fluid zones of the porous medium, as appropriate. The governing equations, along with the boundary conditions as described above, are solved to convergence, using the built-in porous-medium non-equilibrium thermal model in the commercial CFD package FLUENT [97]. Pressure-velocity coupling is addressed via the SIMPLE algorithm, along with an algebraic multigrid algorithm (AMG) for solving the linearized system of governing equations. For monitoring convergence, we employ a solution procedure similar to that employed for the unit-cell model, whereby the governing equations are first solved using a first-order upwind scheme for a few iterations. Employing the flow and temperature fields so obtained as the initial conditions, the equations are then solved using a second-order upwind scheme until convergence is achieved. The governing equations are also suitably under-relaxed to ensure proper convergence. Moreover, the average pressure at the inlet and the average temperature of the bottom wall are also monitored to check for convergence of the flow and energy equations, respectively.

A.3 Solution Methodology

The optimization methodology and the uncertainty quantification (UQ) procedure are described briefly. Further details may be found in Eldred [100] and Xiu and Karniadakis [77].

A.3.1 Uncertainty Quantification

The first step in the optimization under uncertainty procedure is uncertainty quantification (UQ). This procedure entails determination of uncertainties in outputs for given input uncertainties. Uncertainties are commonly categorized as being aleatoric or epistemic. The aleatoric uncertainties (also known as statistical uncertainties) in inputs result from an inherent randomness which occurs every time an experiment is run, while the epistemic uncertainties (also known as systematic uncertainties) result from limited data and knowledge [100]. In the present work, the analysis is restricted to aleatorically uncertain variables, for which probabilistic methods such as polynomial chaos expansions (PCEs) may be used to determine the output statistics.

The most common UQ methods used are random sampling techniques. Random sampling methods employ standard algorithms such as Monte Carlo or Latin Hypercube sampling, for randomly drawing samples based on input probability distribution functions. In this method, the simulation is performed for each sample drawn, and when the entire range of input variations is covered, response statistics and PDFs of outputs are computed [93]. This entails performing thousands of simulations to cover the entire the range of input variations. For complicated problems, this becomes untenable owing to the large

number of simulations involved. Other methods such as the sensitivity method based on moments of samples are also used for UQ, but these methods are less robust and depend on the model assumptions.

For moderate numbers of input random variables, the polynomial chaos expansion (PCE) method is more efficient and computationally tractable than random sampling methods. In the present work, the generalized polynomial chaos (gPC) approach is used with the Wiener-Askey scheme [77]. In this approach, uncertain variables, represented by normal, uniform, exponential, beta, and gamma PDFs, are modeled by Hermite, Legendre, Laguerre, Jacobian and generalized Laguerre orthogonal polynomials, respectively. It has been shown that these orthogonal polynomials are optimal for the corresponding distribution types since the inner product weighting function and its support range correspond to the PDFs of these distributions [77]. In theory, this selection of the optimal basis allows for exponential convergence rates. The gPC method may be either intrusive or non-intrusive. The stochastic collocation method is a non-intrusive method based on gPC [77]. In this method, the polynomials mentioned above are used as an orthogonal basis to estimate the dependence of the stochastic form of the output on each of the uncertain inputs. Deterministic simulations are performed at the collocation points in random space. The coefficients in the polynomial expansion are determined by making use of the orthogonality properties of the polynomial basis function. Further details may be found in [77] and in the comprehensive review by Eldred [100]. The utility of such a non-intrusive gPC approach in the design of electronics cooling equipment such as pin-fin heat sinks, and its advantages compared to an intrusive approach, were demonstrated recently by Bodla *et al.* [76].

The polynomial chaos expansion for a response R is expressed as

$$R = \sum_{j=0}^{\infty} \alpha_j \psi_j(\xi) \tag{A.13}$$

Each of the terms $\psi_j(\xi)$ consists of multivariate polynomials obtained from the products of the corresponding one-dimensional polynomials. Neglecting the higher-order terms in Eq (A.13) results in a finite number of evaluations needed to compute the response function R. The Smolyak sparse grid technique can be used to select the specific evaluation points. This sparse grid technique has proven to be computationally more efficient than other methods such as quadrature grids for each random variable (which gives a tensor product grid when there are more than one random variables) [100]. The Smolyak sparse grid requires fewer computations than the tensor product grid when there are a large number of uncertain parameters. Hence, the Smolyak grid has been used for the present work.

Deterministic simulations are performed at the points selected by this method, and the response surface of the outputs is generated. This response surface is then used as a surrogate model for the dependence of the output on inputs. The PDFs of the response R may be computed by sampling the space of input random variables using random sampling algorithms such as Monte Carlo or Latin Hypercube sampling. Output response statistics, such as PDFs, and the mean and standard deviation of the outputs, may then be readily computed [76].

The gPC-based UQ analysis also provides other useful information such as Sobol's indices [101]. Sobol's indices indicate the sensitivity of output parameters to the various uncertain input parameters; such information is valuable in identifying critical input

parameters. The sensitivity information obtained from the Sobol indices from a coarse UQ analysis may be used to exclude some of the parameters which do not affect the outputs significantly. The subsequent refined UQ analysis can then be performed with fewer uncertain variables, thereby reducing the computational effort significantly. In the present study, the open source UQ and optimization toolkit, DAKOTA (Design Analysis Kit for Optimization and Terascale Applications) [102], is used for performing the UQ analysis as well as the corresponding optimization.

A.3.2 Optimization Under Uncertainty

Optimization under uncertainty (OUU) refers to probabilistic optimization, which involves optimization of a design by taking into consideration the uncertainties in inputs and the corresponding output response statistics. The optimization toolkit DAKOTA used in the present study consists of various OUU formulations, as described in detail by Eldred *et al*. [102] . In this work, the nested approach is used for the probabilistic optimization in which the UQ performed in the inner loop is nested within an outer optimization loop [77]. DAKOTA consists of various gradient and non-gradient based optimization algorithms; we choose the gradient-based Fletcher-Reeves conjugate gradient method for unconstrained optimization, and the method of feasible directions for constrained optimization. These tools are available in the CONMIN library [103] of the DAKOTA package.

The nested OUU approach employed in the present work is shown schematically in Figure A.3. The initial guesses for the various design variables are provided by the user.

Starting with these values, the gPC-based method described earlier is used to perform the complete UQ analysis in the inner loop for the specified uncertainties in the input parameters. The uncertain design variables generated from the outer optimization loop are mapped into the inner UQ loop as required, using nested model controls available in DAKOTA [76]. The output response metrics from the UQ loop are used to evaluate the statistics of the objective function such as the mean and standard deviation. These output statistics are then passed on to the optimizer in the outer loop. The optimizer verifies if the objective function is maximized (minimized), in addition to satisfying the various constraints that are imposed, such as those to restrict the standard deviation in an output. If the convergence criteria are not met, *i.e.*, if a constraint is violated, or if the objective function is not at its maximum (or minimum), a new set of design variables is selected and the whole procedure is repeated. Thus, at convergence, the set of design variables that optimizes the objective function and simultaneously satisfies the specified constraints is obtained [76].

For performing probabilistic optimization effectively, the entire process involved in the nested loops as described above must be automated. This is achieved by using DPREPRO, the built-in pre-processor available in DAKOTA [102] . A simple Python script is written to automate the entire process shown in Figure A.3. The geometry is parameterized for meshing, and the journal features of the meshing package CUBIT [96] are utilized for generating meshes at the Smolyak collocation points. Once the computational model is parameterized, actual values of the parameters for individual evaluations are obtained using DPREPRO with little or no manual intervention. The governing equations are solved using the commercial CFD package FLUENT [97]. To

increase computational efficiency, the parallel CFD capabilities of FLUENT are employed. The various inner loop UQ evaluations at the Smolyak collocation points are also performed in parallel to reduce the overall computational time. The outputs from the FLUENT evaluations are generated in the format required by DAKOTA by the use of suitable user-defined functions. After the first outer-loop iteration, the results are passed back to the optimizer, which then decides the next set of design variables. The process is repeated until the convergence criterion and the constraints are satisfied. The OUU process described here has been validated for a simple heater block design and used for pin-fin heat sink optimization by Bodla *et al.* [76].

With the available computational resources and with the use of parallelized CFD solvers, each simulation (one complete inner loop evaluation) required approximately 90 minutes of real time for the unit-cell model and about 45 minutes of real time for the porous-medium model. The simulations were performed using 4 Intel E5410 processors in parallel. The Smolyak grid determines the number of inner loop simulations required for each outer loop set of design variables. A sparse grid of level 1 was used for the inner uncertainty loop for the probabilistic optimization, which resulted in 7 inner loop evaluations for 3 uncertain variables. The computational time can be reduced by first performing a deterministic optimization and then using the optimized values obtained as initial guess values for the probabilistic optimization. The optimization under uncertainty is first carried out for the unit-cell model and then repeated for the porous-medium model.

A.4 Results and Discussion

We now present results for OUU of manifold microchannel heat sinks obtained via the unit-cell and the porous-medium models, respectively. The optimal designs obtained through deterministic and probabilistic optimizations, performed using the unit-cell model, are compared. Further, results of probabilistic optimization, obtained using the porous-medium model, are discussed.

A.4.1 Verification and Validation

Before performing the optimization, the numerical models are first verified by comparing against experimental results performed in the literature on geometrically-similar heat sinks. A mesh-independence study is also performed prior to parameterizing the model for use in the automated OUU study.

A.4.1.1 Unit-Cell Model

For assessing mesh independence of the unit-cell model, the average pressure difference between the inlet and outlet ports is computed and compared for different grid sizes for a test case. The meshing is performed in CUBIT [96] employing the *tetmesh* scheme. Also, for lowering the overall mesh count, a graded mesh with a gradually increasing mesh size ratio, finer at the solid-fluid interface and coarser towards the bulk volume, is employed. The mesh size ratio is defined as the ratio of the cell size furthest from the heated boundary wall to that of the cell nearest to the boundary wall. By this means, the

level of mesh refinement for which the percentage error with respect to the finest grid size falls below an acceptable value is selected as the optimum mesh size for all the subsequent evaluations. The results of the mesh independence study for the unit-cell model are shown in Figure A.4 (a), performed for an MMC heat sink with parameters, W_c = 80 μm, D_c = 200 μm, D_m = 300 μm, L_{out} = 120 μm, r = 0.5, at a fixed inlet mass flow rate of 0.5 g/s. For this case, a mesh size of 655,360 (40 x 64 x 256) cells, corresponding to a mesh size ratio of 6.25, is observed to result in a pressure drop value which is within 0.3% of that obtained employing the finest grid size, consisting of about triple the number of mesh elements. Hence, results obtained via this mesh size may be deemed mesh-independent and this mesh is used for the results presented in this work.

To characterize flow and heat transfer phenomena and to validate the unit-cell model, simulations are first performed for fixed geometric parameters. Fluid is pumped through the inlet manifold of an MMC heat sink with fixed dimensions at varying mass flow rates, and a heat flux of 75 W/cm^2 is applied to the bottom surface. Figure A.5 (a) shows the velocity vectors obtained at the center plane of microchannel. As the fluid enters the microchannel, due to the sudden contraction, it accelerates rapidly. The fluid turns through 90 degrees and travels through the channel. At the end of the manifold, the fluid again turns through 90 degrees and exits via the outlet. Figure A.5 (b) and Figure A.5 (c) show the thermal contours at the center plane for two different inlet mass flow rates of 0.5 g/s and 5.0 g/s. It is observed that the maximum cooling effect is seen at the channel inlet region, where the thermal boundary layer is thinnest. Figure A.5 (c) also shows the enhanced heat transfer obtained at higher flow rates.

In order to validate the numerical procedure, the heat transfer coefficient for various flow rates is compared with experimental results from Kermani [87] . The heat transfer coefficient is calculated as [87]:

$$h = \frac{q_w^{"}}{T_w - 0.5\left(T_{in} + T_{out}\right)} \tag{A.14}$$

Figure A.6 shows the heat transfer coefficient values as a function of the flow rate, for the case of a channel with an aspect ratio (W_c/D_c) of 0.1. It may be observed that as the flow rate of the coolant increases, the heat transfer coefficient increases as expected. Further, the results from the present computations are found to be in close agreement with the experimental results of Kermani [87], within limits of the experimental uncertainties reported. This validates our numerical unit-cell model.

Having verified and validated the numerical model, simulations are performed to observe the effects of varying geometric parameters. For all subsequent simulations, fluid is pumped through the inlet manifold at an overall mass flow rate of 0.5 g/s [87], and a heat flux of 100 W/cm^2 [92] is applied on the bottom wall, unless otherwise mentioned.

A.4.1.2 Porous-Medium Model

A mesh-independence study, similar to that for the unit-cell model, is also performed for the porous-medium model. For the inlet and outlet fluid volumes, a graded mesh, made finer near the solid-fluid and porous-fluid boundary interface walls and coarser away from these boundaries, is used, similar to the unit-cell model. The comparatively simple microchannel porous medium volume is meshed with coarse grids. A manifold length of 1000 μm (equal to the heat sink size in the transverse direction) and a coolant

flow rate of 0.5 g/s is considered. Figure A.4 (b) shows the results obtained from the mesh-independence study. The computed inlet-to-outlet pressure drop with a mesh size of 309,000 cells, corresponding to a mesh size ratio of 6.1, was found to be within 0.3% of that obtained employing the finest mesh size, consisting of approximately 1,600,000 cells. For all the subsequent simulations, a mesh size of approximately 309,000 cells is used. For the unit-cell model, this manifold length of 1000 μm corresponds to 25 microchannels of width W_c = 20 μm each, with a mesh size of 655,360 cells per microchannel unit cell. The porous-medium model not only reduces the required mesh size by half, but also represents the full array of microchannels, unlike the single microchannels considered in the unit-cell model.

Numerical computations with the porous-medium model are performed for same values of coolant flow rates and heat fluxes as in the case of the unit-cell model, to facilitate a one-to-one comparison of the models. Table A.1 shows the pressure drop obtained with the unit-cell and porous-medium models, for different inlet flow rates and a constant channel width of 20 μm. Similarly, Table A.2 (a) shows a comparison of pressure drops obtained by these models, computed for a variety of microchannel widths at a constant inlet mass flow rate of 0.5 g/s. As may be noted from Table A.1 and Table A.2 (a), the results obtained via the porous-medium model are within 8% of those obtained via the detailed unit-cell model. Nusselt number values at an imposed heat flux of 100 W/cm^2 are also computed and compared. Table A.2 (b) shows the variation of the average Nusselt number *Nu* with width of the microchannel for the porous-medium model, computed at a constant mass flow rate of 0.5 g/s. The average Nusselt number values match the results from the unit-cell model to within 6%. This further validates the

porous-medium model. It may be mentioned here that the porous-medium model is based upon assumed values for porosity, permeability as well as interstitial heat transfer coefficient, representative of regular microchannels, wherein the flow enters normal to the cross-section of the microchannel and travels along its length. However, in MMC heat sinks, the flow enters in a direction normal to the top of the microchannel, undergoes a 90-degree turn at the inlet, travels through the length of the microchannel, again undergoes a 90-degree turn, and then exits through the manifold outlet. Due to this complex flow path which is not accounted for in the inputs to the model, we see a slight discrepancy in the output hydrodynamic and thermal performance of the porous-medium model. Further, the bottom solid substrate which is a part of the unit-cell model, is not included in the porous-medium model in order to reduce complexity. This also contributes to the discrepancy in thermal performance results, since any conduction heat loss through the bottom substrate has been neglected. However, since the variation in outputs obtained from the porous-medium model are within 8% of those obtained from the unit-cell model, these differences in model conditions are neglected in the rest of this analysis.

After validating and verifying both models, the unit-cell model is employed for assessing the effect of various input parameters on friction factor and Nusselt number. The model is then employed for uncertainty quantification and optimization. Optimization results obtained for the probabilistic optimization using the porous-medium model are also reported and compared with those from the unit-cell model in Section A.4.5, so as to demonstrate the utility of the approach for performing a system-level optimization, as against the single unit cell discussed earlier.

A.4.2 Effect of Parameters

As a first step, the effect of microchannel width and depth and manifold depth on the outputs is assessed. Each input geometric parameter is individually varied and the outputs – the hydrodynamic and thermal performance of the heat sink – are studied. The non-dimensional Nusselt number, Reynolds number and friction factor for the different cases are defined as:

$$Nu = \frac{hD_h}{k_f}$$
$$\mathrm{Re} = \frac{uD_h}{\upsilon} \qquad \text{(A.15)}$$
$$f = \frac{\Delta P\left(D_h / L\right)}{0.5\rho u^2}$$

where u is the velocity at the inlet of the microchannel, D_h the hydraulic diameter of the microchannel, and L is the total length of flow through the channel. The hydraulic diameter of the microchannel is calculated as [92]:

$$D_h = \frac{2D_c W_c}{\left(D_c + W_c\right)} \qquad \text{(A.16)}$$

The effect of the aspect ratio of the microchannel (W_c/D_c) and the manifold depth (D_m) on the non-dimensional outputs is shown in Figure A.7 computed for a fixed inlet coolant mass flow rate of 0.5 g/s. It may be observed that as the channel aspect ratio increases, both *Nu* and *fRe* increase. This may be attributed to the increase in the hydraulic diameter of the channel, which results in a higher Reynolds number. An increase in the manifold depth is seen to increase the value of *fRe* due to increased pressure drop. However, as may be observed from Figure A.7 (a), a change in the

manifold depth does not have a significant effect on *Nu*. This may be attributed to the definition of the heat transfer coefficient which uses the base area of the heat sink, and is therefore not significantly affected by the manifold depth. Hence, a smaller value of D_m would lead to a better overall performance. For the optimization procedure in this study, D_m is fixed at a small value of 100 μm, and is not included as an optimization parameter.

A.4.3 Response Surfaces

Representative response surfaces capturing the effects of the input parameters on the output parameters of interest – pressure drop and heat transfer coefficient – are shown in Figure A.8 (a) and (b), respectively, for a fixed overall inlet mass flow rate of 0.5 g/s. With all other parameters remaining constant, a fixed overall inlet mass flow rate results in fixed flow speed at the inlet of each microchannel, independent of microchannel, for a base heat sink of fixed dimensions. The influence of individual input parameters, W_c and r, computed at the mean values of the fixed input parameters, is also shown in the insets of Figure A.8. As expected, the pressure drop decreases as the microchannel width increases due to the lower flow resistance. Similarly, as the manifold ratio ($r=L_{in}/L_{out}$) increases at a constant flow speed for each microchannel, ΔP increases due to the increased inlet area, leading to an increased contraction area ratio at the inlet. Similarly, the heat transfer coefficient h decreases as the microchannel width increases. However, it is observed to have an optimum value relative to the manifold ratio r which may be explained as follows. As the manifold ratio increases, the inlet length L_{in} increases while the manifold length L_m decreases so as to keep the overall flow length L constant. Hence,

as the manifold ratio increases, there is an increase in mass flow rate at the inlet, leading to an increase in h. However, the decrease in length of manifold L_m also leads to a reduction in area available for heat transfer, thereby leading to a reduction in the heat transfer coefficient. Owing to these competing factors, the heat transfer coefficient displays an optimum value relative to the manifold ratio, which for this case was found to be at approximately $r = 3$.

A.4.4 Uncertainty Quantification Results

The first step in the solution procedure is to perform uncertainty quantification to study the variation of the outputs relative to uncertainties in the various input parameters. For the purpose of demonstration, without loss of generality, geometric parameters such as channel width W_c, channel depth D_c, manifold depth D_m, manifold inlet length L_{in} and manifold outlet length L_{out} are assumed to be uniformly distributed random variables. The wide range of variation considered in the input parameters is summarized in Table A.3. The uncertainty quantification is performed using the Smolyak sparse grid of second order. For this case of 5 uniformly distributed uncertain variables, 71 evaluations are necessary for constructing the response surface. All the simulations are performed at an overall inlet mass flow rate of 0.5 g/s and temperature $T_{in} = 300$ K. Once the explicit gPC representation of the response surface is obtained, 10,000 samples are randomly drawn to calculate the output response characteristics. The PDFs of the heat transfer coefficient and pressure drop obtained for the range of uncertain inputs considered are shown in Figure A.9 (a) and (b), respectively. The corresponding mean and standard

deviation of the outputs are computed and compared against the deterministic values obtained by fixing the uncertain variables at their mean values. The results of both the probabilistic and deterministic simulations are reported in Table A.3. For the probabilistic runs, the mean values are reported along with the standard deviation σ_s.

Due to the wide range of variation of inputs under consideration, we obtain a widely spread-out PDF for the variation in outputs. Also, there is a significant difference between the mean values of pressure drop obtained from the UQ study and that from the deterministic study obtained by fixing the uncertain variables at their mean values. We also note the large observed standard deviations of the outputs, h and ΔP. This demonstrates the importance of using a probabilistic approach for design and optimization of MMC heat sinks.

Apart from UQ, a sensitivity analysis is also performed employing DAKOTA. In order to assess the sensitivity of outputs to various inputs under consideration, uncertainty quantification analysis is performed by varying a single input parameter for which the sensitivity is being assessed, while keeping all the other inputs fixed at their mean values. The inputs relative to which a higher standard deviation is obtained in the outputs are identified as the more sensitive variables. The standard deviations of the outputs, heat transfer coefficient and pressure drop, obtained as the various input parameters are varied are listed in Table A.4. Of all the variables considered, the outputs are most sensitive to variations in the width of the microchannel W_c and the length of the inlet manifold L_{in}. This information is valuable for design of experiments [93], since the primitive UQ results can be used to obtain an estimate of the most sensitive parameters, and the uncertainties in these parameters can then be resolved by a finer UQ analysis. Also, the

insensitive parameters may be assumed as deterministic, thereby enhancing computational efficiency [93].

A.4.5 Optimization

The results of the deterministic and probabilistic optimization obtained by employing the unit-cell model are presented here, along with results of probabilistic optimization from the system-level porous-medium model.

A conventional, deterministic optimization study is first performed to arrive at the optimum geometry without considering the effect of uncertainties. In order to validate the optimization process, a simple case is considered. For this case, a single-objective optimization is performed, so as to find the optimum width for maximizing heat transfer coefficient at an overall inlet mass flow rate of 0.5 g/s. The mass flow rate at the inlet of the unit cell is calculated from the overall mass flow rate by considering the number of manifolds and microchannels appropriately. The microchannel width W_c is allowed to take values between 10 μm and 100 μm for the optimization. Starting with an initial guess value of W_c = 80 μm, the optimum width of W_c = 10 μm is predicted within about 7 iterations. As expected, the minimum microchannel width results in the maximum heat transfer coefficient and hence, the optimization process is validated.

As the mass flow rate at the inlet is increased, although the thermal performance improves, the pressure drop also increases significantly. Hence, a multi-objective optimization is performed. The following objective function that takes into account the effect of both h and ΔP with appropriate scaling is considered:

$$OF = w_1\left(h/h_{\max}\right) - w_2\left(\Delta P/\Delta P_{\max}\right) \tag{A.17}$$

Here h_{max} and ΔP_{max} are the maximum values of heat transfer coefficient and pressure drop, respectively, for the range of variation of inputs considered. This scaling of the outputs ensures that both thermal and flow characteristics are of the same order of magnitude, for comparison. Weight functions w_1 and w_2 sum up to a value of 1, with their individual values depending on the relative importance ascribed to the two performance metrics. Thus, for an assumed set of weight functions, maximizing this objective function ensures an optimized geometry with maximum heat transfer coefficient and minimum pressure drop.

The geometric parameters of the manifold are taken into account by a non-dimensional manifold ratio r given by:

$$r = L_{in} \Big/ L_{out}$$
$$L_m = L - L_{in} - L_{out} \tag{A.18}$$

In this study, it may be noted that the length of the outlet manifold is fixed at L_{out} = 72 μm, while the length of the inlet manifold L_{in} is computed from Eq (A.18) for various values of r. Also, the total flow length is fixed at L = 400 μm, and the length of the manifold is computed from Eq (A.18), as indicated. The input geometric parameters considered for the optimization are the microchannel width W_c and the manifold ratio r. Beginning with initial guess values, the optimizer iteratively varies the values of these variables until convergence is achieved. The optimization is performed for two different input conditions, $\dot{m}$ = 0.5 g/s and $\dot{m}$ = 1.5 g/s, and for different weighting functions, w_1 = 0.5, w_2 = 0.5 and w_1 = 0.7 and w_2 = 0.3, respectively.

Besides this deterministic optimization, we also perform a probabilistic optimization using the nested OUU approach described previously. The OUU is performed to predict the design variables that maximize the objective function, taking into account uncertainties in the geometric parameters, while also restricting the standard deviation of the objective function to a prescribed value, thus resulting in a robust design. In this case, the microchannel width W_c and manifold ratio r are considered as design variables with specified uncertainties. Thus, for each set of values of W_c and r obtained from the optimizer, the uncertainties are imposed in the inner UQ loop. This is achieved by appropriate mapping of the outer loop variables into the inner loop [103]. The depth of the microchannel D_c is also considered as an uncertain variable with specified uncertainty. From Eq (A.18), the uncertainty in manifold ratio translates to uncertainties in the manifold lengths L_{in} and L_m. Table A.5 lists the values of the normal uncertain variables with the standard deviation considered for this analysis. It may be noted that the uncertainties considered in the present study are based on approximate tolerances specified by the manufacturers. The output – the scaled heat transfer coefficient ratio – is subjected to a constraint, bounding its standard deviation. The OUU problem statement is formally defined as:

$$\begin{aligned} &\textbf{Maximize} \quad OF = w_1\left(h/h_{\max}\right) - w_2\left(\Delta P/\Delta P_{\max}\right) \\ &\textbf{such that} \quad \sigma_s\left(h/h_{\max}\right) \le 0.02, \quad \dot{m} = 0.5g/s \\ &\qquad\qquad \sigma_s\left(h/h_{\max}\right) \le 0.035, \quad \dot{m} = 1.5g/s \end{aligned} \tag{A.19}$$

Figure A.10 shows the convergence history of the optimization procedure for two representative cases with Figure A.10 (a) corresponding to deterministic optimization with $\dot{m}$ = 1.5 g/s and $w_1 = w_2 = 0.5$, and Figure A.10 (b) to probabilistic optimization with

$\dot{m}$ = 1.5 g/s, w_1 = 0.7 and w_2 = 0.3. For the case of probabilistic optimization, the variation in standard deviation of the output (h/h_{max}) is also shown. For the different input conditions and weighting functions considered in this work, the corresponding converged values of the design parameters are shown in Table A.6 for deterministic as well as probabilistic optimization cases, with the first column describing the condition for which the optimization is performed, *i.e*, the input mass flow rate, the objective function weights and the values of h_{max} and ΔP_{max}. It may be observed from Table A.6 that for both deterministic and probabilistic optimization, as the value of w_1 is increased, the value of optimum width decreases and that of manifold ratio increases. This is due to the fact that a higher value of w_1 means that the objective function is dominated by the heat transfer coefficient, the value of which increases as the width decreases and manifold ratio increases. Also, for the case of probabilistic optimization, the imposed constraint restricting the standard deviation of the scaled output results in more conservative values for the geometric parameters, as also observed by Bodla *et al*. [76] for the case of pin-fin heat sinks. Hence, the use of this approach allows us to quantify precisely how conservative the design needs to be in order to account for the uncertainties. Furthermore, owing to the conservative nature of the design, the output objective function is lower for the probabilistic case than that obtained with the deterministic counterpart. At the same time, by accounting for uncertainties as part of the optimization procedure, the probabilistic design ensures a more predictable and robust design. The convergence history shown in Figure A.10 (a) and (b) may also be used to gain a first estimate of the expected value of the output when values for the design variables other than the final converged value are chosen. Such history data may also be used to assess whether a

tighter or looser convergence criterion may be employed for obtaining better converged results quickly [76].

System-level optimization under uncertainty is demonstrated with an OUU study employing the porous-medium model. The analysis considers the same set of input parameter variations and constraints and an inlet mass flow rate of 0.5 g/s as used above with the unit-cell model. The results obtained from the porous-medium model are shown in Table A.7 along with those from the unit-cell model. It may be observed that the optimum microchannel width and manifold inlet length obtained with both models are in close agreement with each other. This further validates the porous-medium model and demonstrates its utility for performing a system-level optimization analysis. Such a model may be used for analysis of complex, realistic cases such as those involving non-uniform heat fluxes. As described in Section A.4.1.1, the optimum mesh size required for the porous-medium model for the entire manifold length (25 unit cells) is about half that of the unit-cell model for a single microchannel, which results in a corresponding reduction in computational time for the porous-medium model.

The OUU analysis in this study is performed using a Smolyak sparse grid of level 1, which results in 7 inner loop evaluations for each outer loop evaluation, for the case of 3 uncertain variables. A complete OUU evaluation converges in approximately 20 outer loop evaluations. A complete optimization study in this case therefore requires 140 overall evaluations. Using the parallelized CFD capabilities of FLUENT, and available computational resources, *i.e.*, Quad-Core Intel E5410 processors, all the inner loop evaluations were run in parallel, so that each outer loop evaluation of the unit-cell model required roughly 90 minutes of real time. Similarly, each outer loop evaluation

employing the porous-medium model required around 45 minutes. Thus, the total time required for one complete probabilistic optimization study was approximately 30 and 15 hours for the unit-cell (single channel) and porous-medium (multiple channels) models, respectively. The porous-medium model offers a cost-effective, alternative approach that is useful for system-level optimizations.

A.5 Conclusions

A 3-D numerical model for manifold microchannel (MMC) heat sinks is developed and validated. Further, an Uncertainty Quantification (UQ) analysis is performed to demonstrate the effect of input uncertainties on the output parameters of interest. A cumulative objective function is defined for considering the two outputs of interest in the design of heat sinks*, i.e.*, heat transfer coefficient and pressure drop. A unit-cell geometry of the MMC heat sink is optimized by taking into account the effect of inherent uncertainties present in the various input parameters. A framework for performing such probabilistic optimization is developed in DAKOTA, an open-source optimization and uncertainty quantification toolkit. The corresponding results obtained via the Optimization Under Uncertainty (OUU) approach are compared with those obtained with a conventional deterministic counterpart, and the conservative nature of the probabilistic design approach is quantified. Based on sensitivity information, the critical input parameters to which the output quantities are most sensitive are also identified. In addition, a cost-effective porous-medium model for the MMC heat sinks is presented and validated, and subsequently used for optimization under uncertainty. This model

provides a system-level optimization of the geometry taking all the microchannels in the heat sink into account, as against a single microchannel considered in the unit-cell approach, thereby allowing the designer to consider complex, realistic cases of non-uniformly applied heat fluxes. A representative case is considered and the utility of the model is demonstrated by comparing against the detailed unit-cell model.

Table A.1. Effect of mass flow rate and comparison of hydrodynamic performance of MMC heat sink, as predicted by the unit-cell and porous-medium models. The present case corresponds to W_c = 20 μm, D_c = 200 μm, D_m = 500 μm, L_{in} = 60 μm, and L_{out} = 120 μm.

Mass Flow Rate (g/s)	ΔP (Pa) Unit-Cell Model	ΔP (Pa) Porous-Medium Model	% Difference (±)
0.5	352.7	331.1	6.1
1.0	693.5	675.3	2.6
1.5	1041.3	1032.6	0.8
2.0	1390.6	1403.1	0.9
2.5	1741.6	1786.7	2.6

Table A.2. Effect of channel width and comparison of (a) hydrodynamic and (b) thermal performance, as predicted by the unit-cell and porous-medium models. The present case corresponds to a fixed mass flow rate of 0.5 g/s.

(a) (b)

Channel Width W_c (μm)	ΔP (Pa) Unit-Cell Model	ΔP (Pa) Porous-Medium Model	Difference (± %)	Nu Unit-Cell Model	Nu Porous-Medium Model	Difference (± %)
20	341.3	315.2	7.6	2.10	2.11	0.4
40	106.1	98.4	7.2	3.87	3.79	2.1
60	58.7	55.3	5.8	5.32	5.05	5.0
80	41.1	39.9	2.9	6.39	6.02	5.8

Table A.3. Uncertainty quantification for MMC heat sinks.

Parameter	Deterministic approach	Probabilistic approach, Uniform random distribution of inputs
Inputs		
D_c (μm)	200	Minimum = 100 Maximum = 300
W_c (μm)	260	Minimum = 20 Maximum = 500
D_m (μm)	260	Minimum = 100 Maximum = 300
L_{in} (μm)	60	Minimum = 20 Maximum = 200
L_{out} (μm)	120	Minimum = 20 Maximum = 200
Outputs		
h (W/m^2K)	29120	Mean = 30120 σ_s = 10703
ΔP (Pa)	32	Mean = 56 σ_s = 27

Table A.4. Sensitivity analysis for MMC heat sinks.

Variable input	Range of variation in input	Std. deviation in h (W/m^2K)	Std. deviation in ΔP (Pa)
W_c (μm)	Uniform random, min. = 40 max. = 80	419	23.7
L_{in} (μm)	Uniform random, min. = 50 max. = 80	5325	2.7
D_c (μm)	Uniform random, min. = 180 max. = 220	234	1.2
L_{out} (μm)	Uniform random, min. = 100 max. = 140	35	2.7

Table A.5. Input parameters for deterministic and probabilistic optimization of an MMC heat sink: $W_{c,\,det}$ and r_{det} are the mean values of the variables obtained from each iteration of the outer optimization loop.

Parameter	Deterministic optimization	Probabilistic optimization
L_{out} (μm)	72	72
D_c (μm)	200	Mean = 200 σ_s = 10
W_c (μm)	Minimum = 10 Maximum = 100	Minimum = 10 Maximum = 100 Mean = $W_{c,\,det}$ σ_s = 10
r	Minimum = 0.5 Maximum = 4	Minimum = 0.5 Maximum = 4 Mean = r_{det} σ_s = 0.1
L_{in} (μm)	Minimum = 36 Maximum = 288	Minimum = 36 Maximum = 288 σ_s = 7.2
L_m (μm)	Minimum = 40 Maximum = 292	Minimum = 40 Maximum = 292 σ_s = 7.2

Table A.6. Comparison of deterministic and probabilistic optimization results for different mass flow rates and weighing functions.

(a) $\dot{m} = 0.5$ g/s

Condition	Parameter	Deterministic optimization	Probabilistic optimization (Mean values)
$\dot{m}$ = 0.5 g/s h_{max} = 120,000 W/m^{2}K ΔP_{max} = 3000 Pa w_1 = 0.5 w_2 = 0.5 OF= 0.5(h/h_{max})- 0.5($\Delta P/\Delta P_{max}$)	**Inputs**		
	W_c (μm)	33.3	26.5
	r	3.25	2.5
	L_{in} (μm)	234	180
	L_m (μm)	94	148
	Outputs		
	h (W/m^{2}K)	92185	85,766
	ΔP (Pa)	382	532
	OF	0.3204	0.2686
$\dot{m}$ = 0.5 g/s h_{max} = 120,000 W/m^{2}K ΔP_{max} = 3000 Pa w_1 = 0.7 w_2 = 0.3 OF = 0.7(h/h_{max})- 0.3($\Delta P/\Delta P_{max}$)	**Inputs**		
	W_c (μm)	27.6	24.2
	r	3.4	2.9
	L_{in} (μm)	245	209
	L_m (μm)	83	119
	Outputs		
	h (W/m^{2}K)	95940	93,257
	ΔP (Pa)	520	689
	OF	0.5076	0.475

(b) $\dot{m} = 1.5$ g/s

Condition	Parameter	Deterministic optimization	Probabilistic optimization
$\dot{m}$ = 1.5 g/s h_{max} = 180000 W/m^{2}K ΔP_{max} = 10000 Pa w_1 = 0.5 w_2 = 0.5 OF= 0.5(h/h_{max})-0.5($\Delta P/\Delta P_{max}$)	**Inputs**		
	W_c (μm)	27	25.6
	r	2.47	1.8
	L_{in} (μm)	178	115.2
	L_m (μm)	150	212.8
	Outputs		
	h (W/m^{2}K)	148314	123964
	ΔP (Pa)	1565	836
	OF	0.3337	0.3025
$\dot{m}$ = 1.5 g/s h_{max} = 180000 W/m^{2}K ΔP_{max} = 10000 Pa w_1 = 0.7 w_2 = 0.3 OF = 0.7(h/h_{max})-0.3($\Delta P/\Delta P_{max}$)	**Inputs**		
	W_c (μm)	22	21.3
	r	2.76	2.4
	L_{in} (μm)	199	173
	L_m (μm)	129	155
	Outputs		
	h (W/m^{2}K)	156832	154511
	ΔP (Pa)	2283	2567
	OF	0.5414	0.5238

Table A.7. Comparison of OUU results obtained via the unit-cell and porous-medium models. The predicted geometry is found to match reasonably well.

Condition	**Unit-Cell Model**		**Porous-Medium Model**	
u **= 0.03 m/s**	W_c (μm)	L_{in} (μm)	W_c (μm)	L_{in} (μm)
$\mathbf{0.7(h/h_{max}) + 0.3(-\Delta P/\Delta P_{max})}$	24	209	30	212
$\mathbf{0.5(h/h_{max}) + 0.5(-\Delta P/\Delta P_{max})}$	27	180	32	184

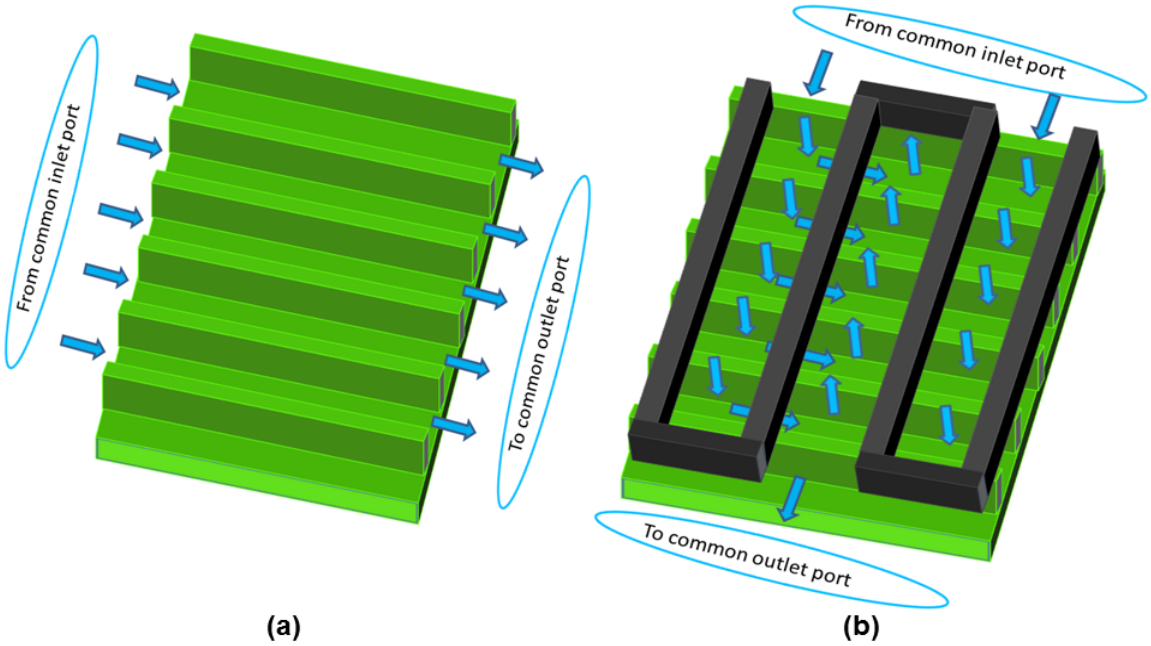

Figure A.1. Schematic figure showing fluid flow path through a (a) conventional microchannel heat sink, and (b) manifold mcirochannel heat sink.

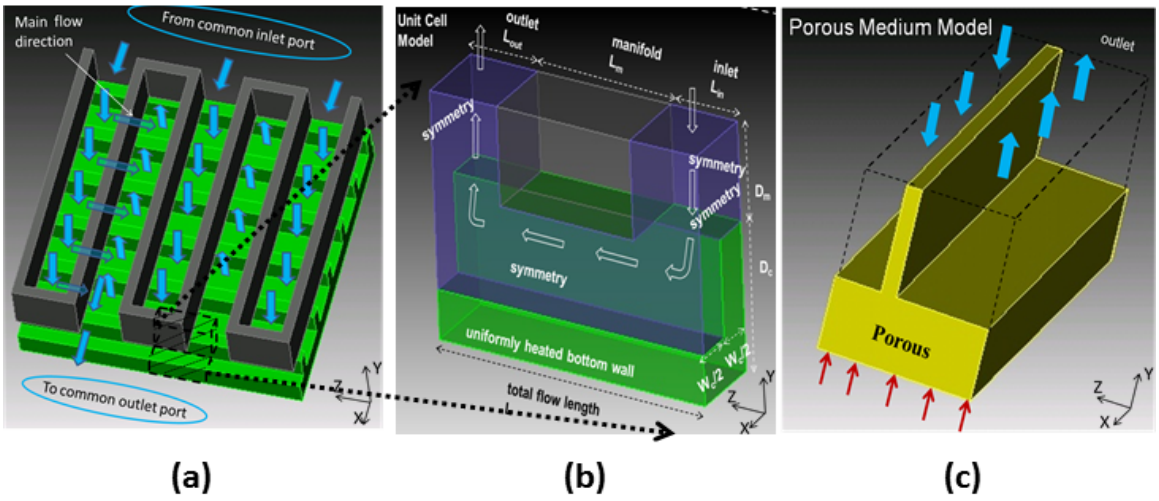

Figure A.2. Computational domains for the MMC heat sink: (a) complete heat sink with coolant path, (b) unit-cell model used for direct simulation, showing geometric parameters and boundary conditions and (c) computational domain for the porous-medium model along with boundary conditions.

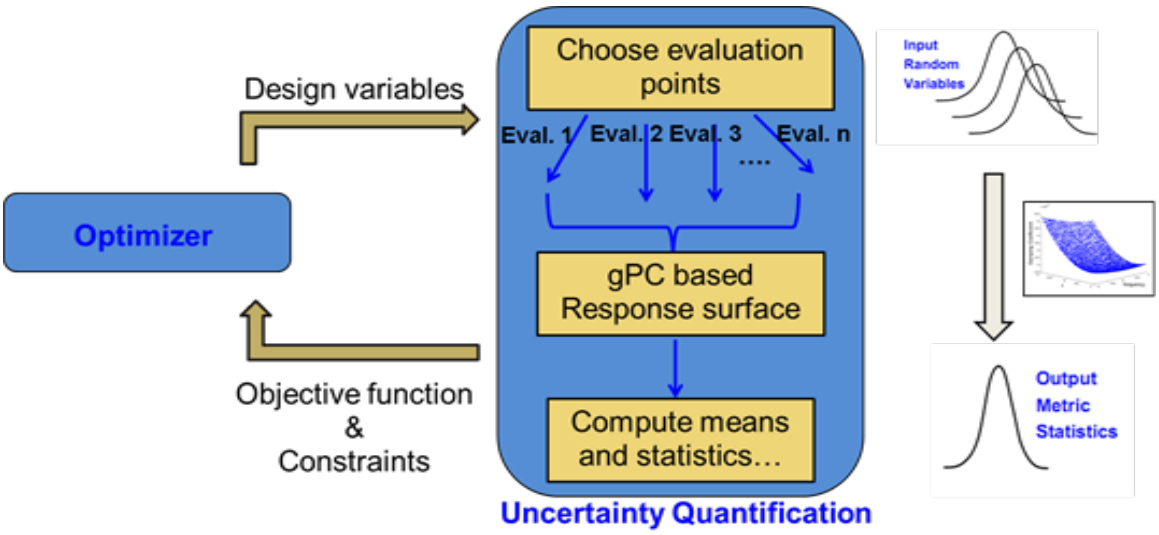

Figure A.3. OUU approach employed in the present work, adapted from [76].

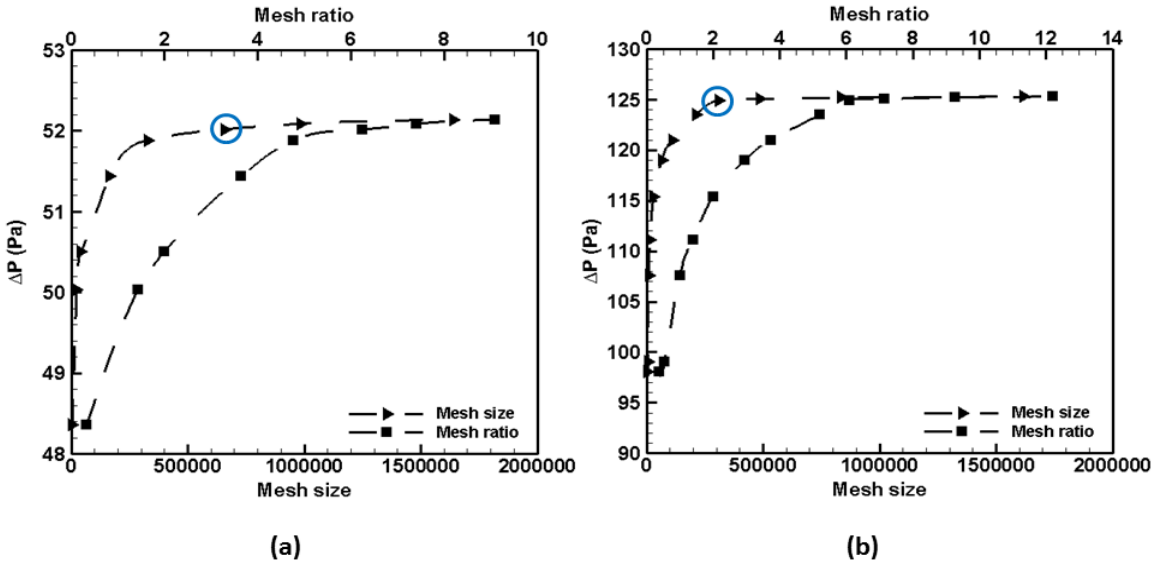

Figure A.4. Mesh-independence study, performed for an overall inlet mass flow rate of 0.5 g/s: (a) unit-cell model with channel dimensions W_c = 80 μm, D_c = 200 μm, D_m = 300 μm, L_{out} = 120 μm, r = 0.5, and L = 160 μm, and (b) porous-medium model with channel dimensions W_c = 80 μm, D_c = 200 μm, D_m = 300 μm, L_{out} = 72 μm, r = 4.0, and L = 1000 μm. The optimum mesh size for which the pressure drop matches to within 0.3% of the value with the finest mesh size considered is highlighted.

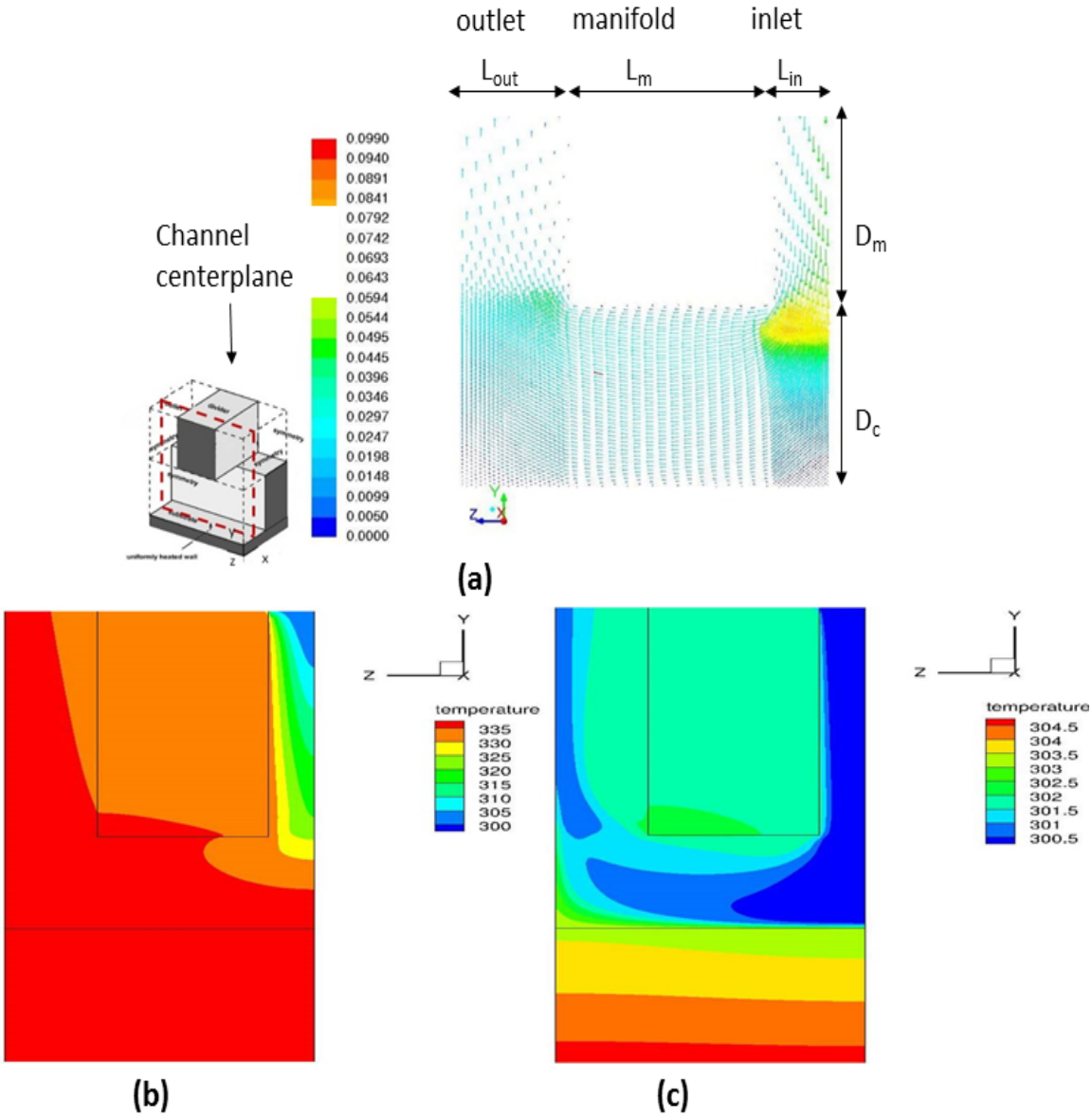

Figure A.5. Velocity vectors and temperature contours for channel dimensions W_c = 40 µm, D_c = 200 µm, D_m = 500 µm, L_{in} = 60 µm, L_{out} = 120 µm: (a) Velocity vectors at center plane of microchannel (plane shown in red dashed lines in the inset) for overall inlet mass flow rate = 0.5 g/s; (b) Temperature contours at center plane of microchannel for overall inlet mass flow rate of 0.5 g/s; and (c) Temperature contours at center plane of microchannel for overall inlet mass flow rate of 5.0 g/s. Velocity values are in m/s and temperature values are in Kelvin.

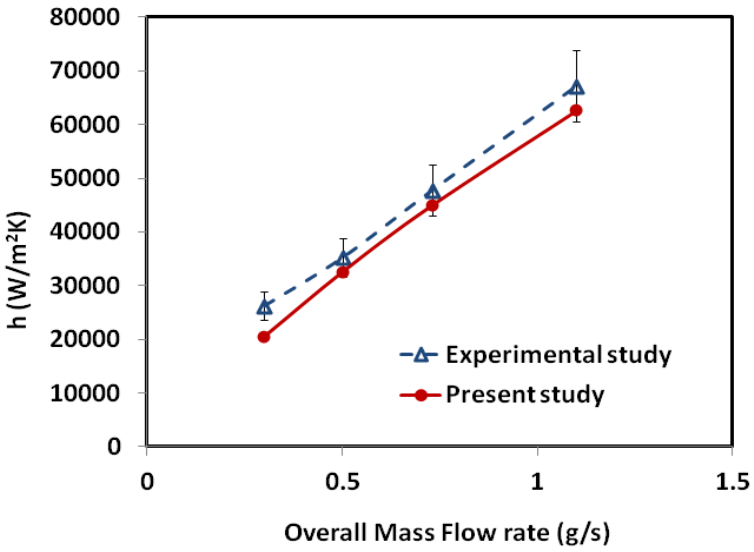

Figure A.6. Heat transfer coefficient as a function of flow rate for a channel aspect ratio = 0.1. Also shown are experimental results along with reported uncertainties from Kermani [87].

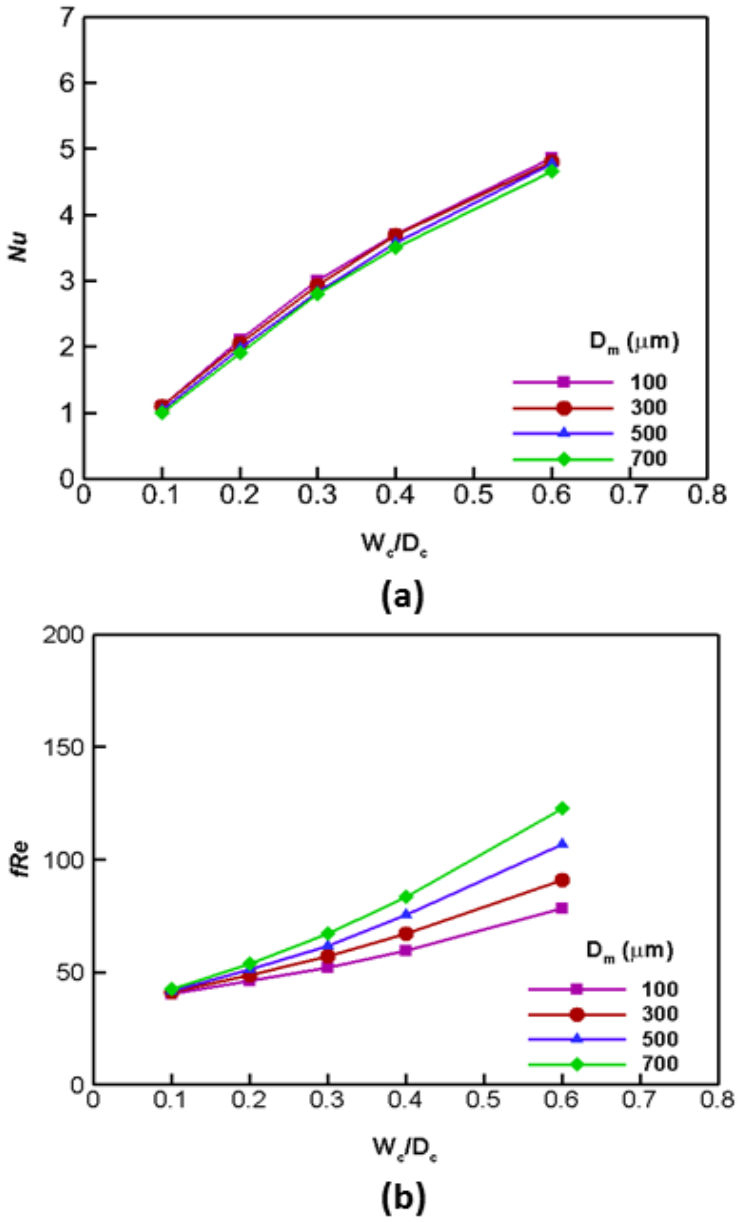

Figure A.7. Effect of the geometric parameters on outputs: (a) Nu, and (b) fRe, computed for the case of fixed coolant mass flow rate of 0.5 g/s.

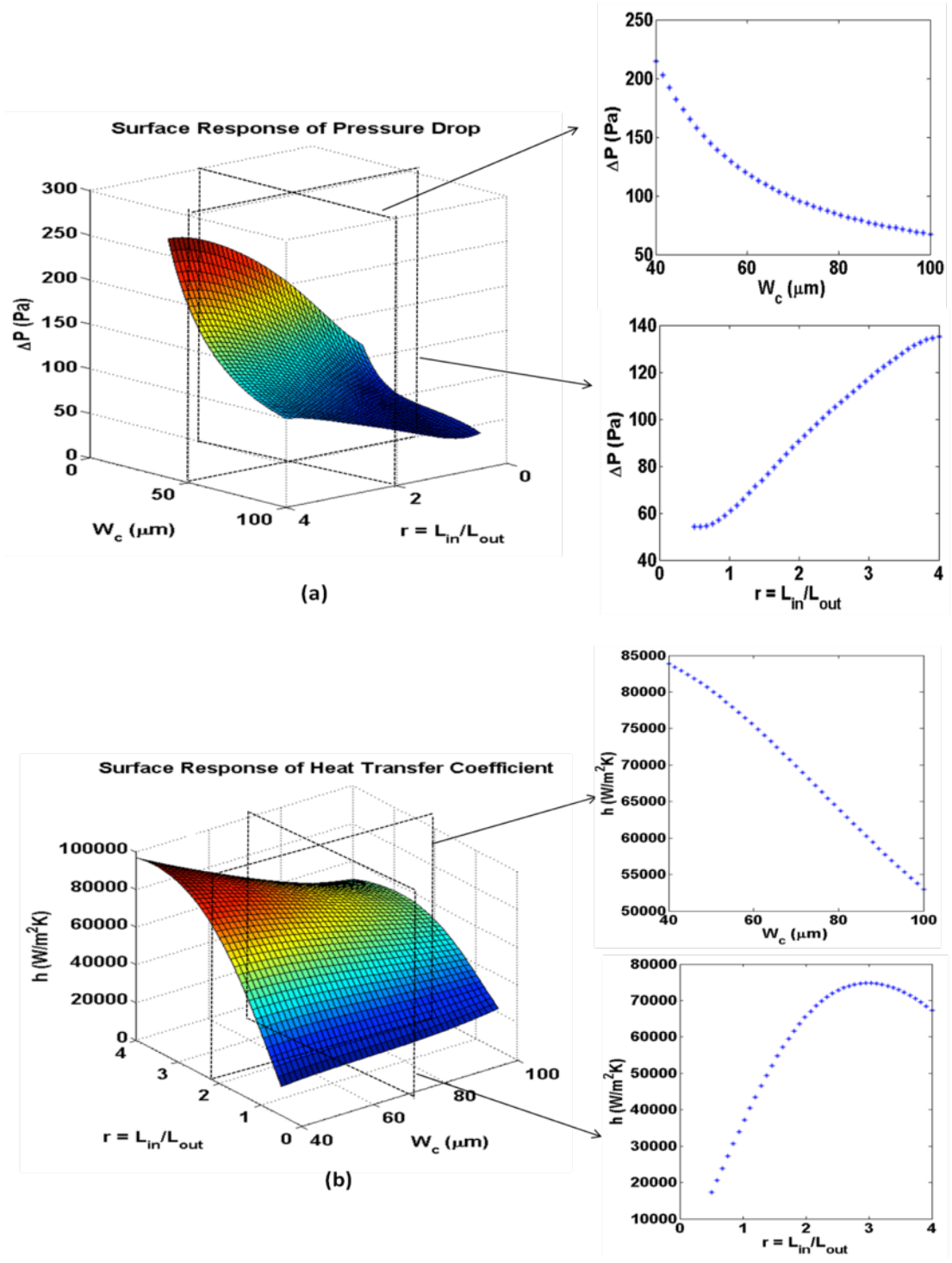

Figure A.8. Representative response surfaces of (a) pressure drop, and (b) heat transfer coefficient, shown as a function of variation in channel width and manifold ratio. The insets show variation of the outputs relative to variation in each input parameter, obtained by holding the other input parameter at its mean value as indicated.

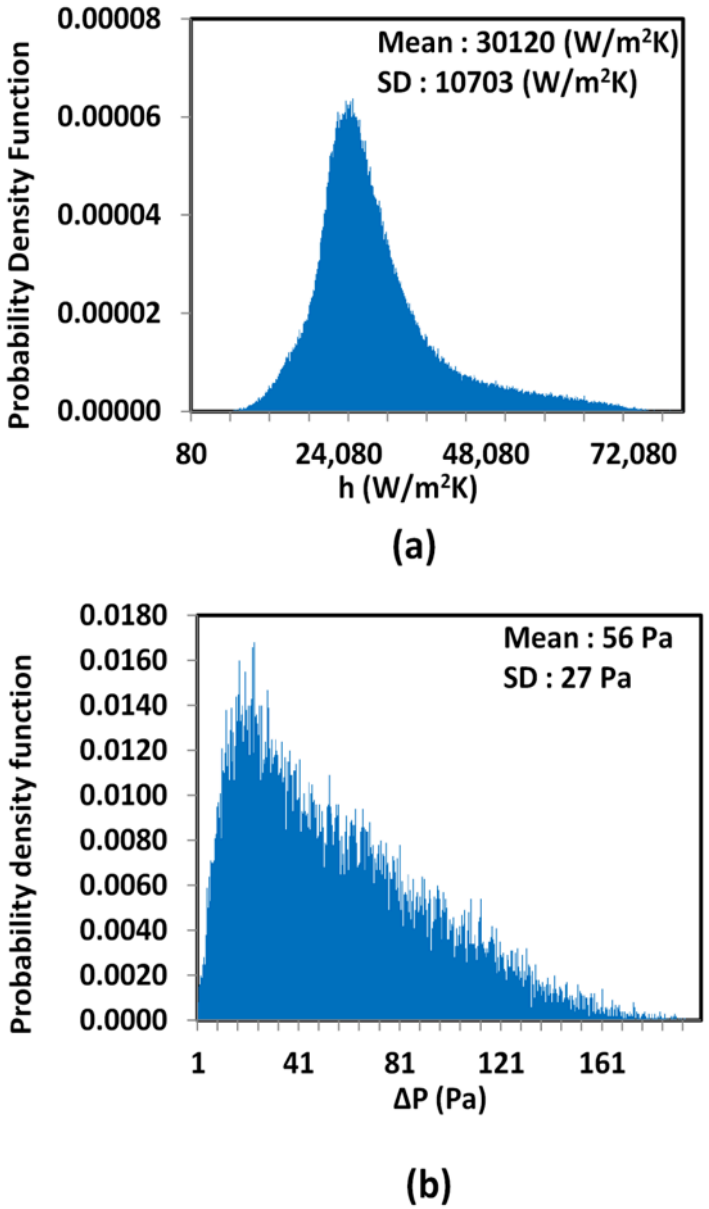

Figure A.9. PDF of (a) heat transfer coefficient, and (b) pressure drop for uniformly distributed input parameters in Table A.3.

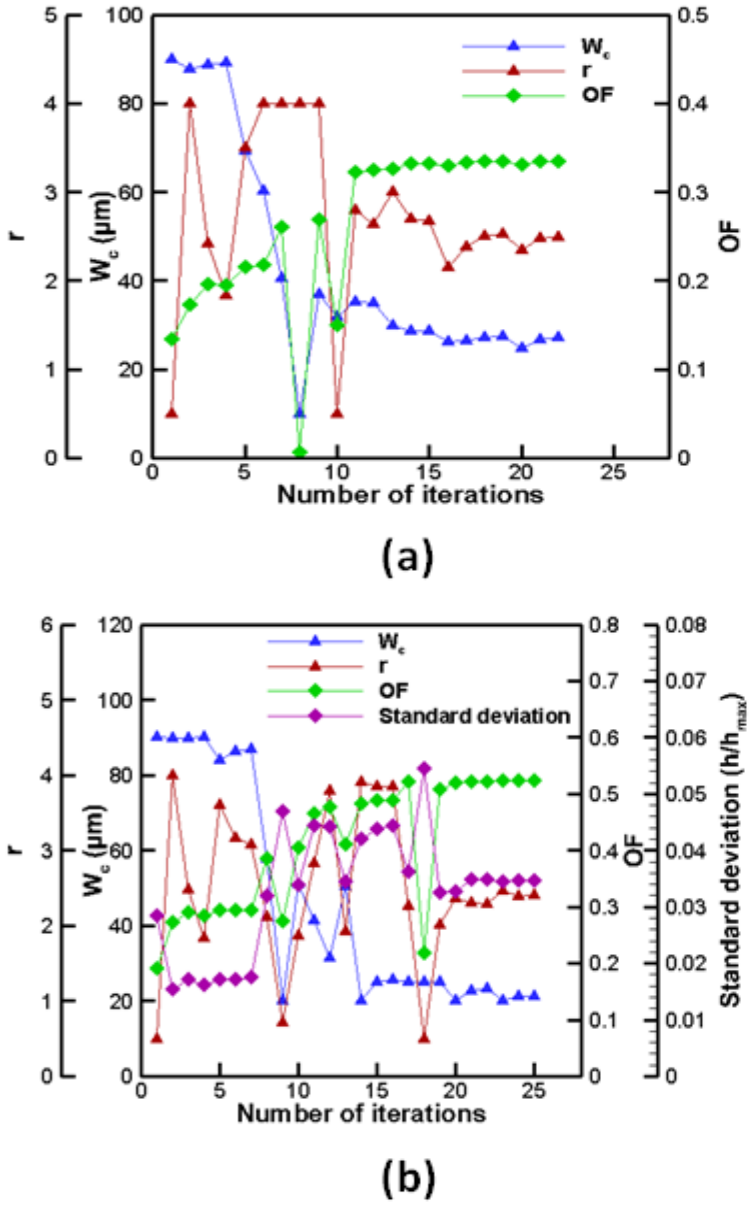

Figure A.10. Convergence history of (a) deterministic optimization for $w_1 = w_2 = 0.5$, and (b) probabilistic optimization for $w_1 = 0.7$ and $w_2 = 0.3$.

APPENDIX B. CALCULATION OF POROSITY AND ELECTRICAL HEAT INPUT

This appendix provides a description of the estimate of porosity of the free-particle and sintered-particle coatings, and a description of the electrical circuit providing heat input to the copper heater block.

B.1 Estimation of Porosity

Estimation of porosity of the free-particle and sintered-particle coatings is crucial for the present study, since the porosity is expected to affect the heat transfer performance of the coating. In order to measure the porosity of free-particles, a graduated cylinder (±0.05 cc accuracy) is zero-weighted and placed on a high-accuracy electronic scale (Voyager, Ohaus). The particles are carefully added to the graduated cylinder by a funnel, and tapped down lightly to avoid sticking to the sides. The weight (W_{por}) and volume (V_{por}) of the particles are measured and plotted as shown in Figure B.1 (a), to calculate the density (ρ_{por}) of the free particles. This is then used to calculate the porosity (ε) as given by Eq (B.15), where ρ_{Cu} is the density of copper.

$$\rho_{por} = \frac{W_{por}}{V_{por}}; \varepsilon = 1 - \frac{\rho_{por}}{\rho_{Cu}} \tag{B.15}$$

For sintered particles, the weight of the copper block is measured before and after the sintering process, to obtain the weight of particles sintered. The height of the coating is

measured after sintering by collecting images against a 50 micron grid under an optical microscope, as shown in Figure B.1 (b). This is then used to obtain the estimated volume of the coating and compared against the known weight of particles used to obtain the porosity, as given by Eq (B.15) above.

The inherent uncertainty in the measuring devices and procedure lead to an uncertainty in the calculated porosity, which is estimated as discussed below. The uncertainty in density of the free-particle coating is obtained from the uncertainty in linear regression fit from Figure B.1 (a), as described in [53], where the uncertainty in weight and volume are U_w = 0.01 g and U_v = 0.05 cc, respectively, owing to the uncertainty of the measurement devices. For the 90-106 μm spherical particles, this uncertainty is 0.06 g/cc, which is 1.2% of the apparent density of 5.098 g/cc. The calculated porosity from Eq (B.15) is 43.1±0.5%, as presented in Table 4.1. For the sintered coating, the height of the sintered sample is measured at 5 different locations along the edge of the sample, and the average sample height is calculated, with an uncertainty of ± 0.025 mm, owing to the uncertainty in reading from the micron grid. The averaging uncertainty of the measurement calculated from the root-mean-square deviation is much lower than ± 0.025 mm and is hence neglected. For the 90-106 μm spherical sintered coating, the average sample height is calculated to be 0.4 mm, and following the same procedure as described for free-particle coatings, this results in a porosity of 23.7±1.5%.

B.2 Power Input to Test Block

Figure B.2 shows a schematic diagram of the electrical circuit used for heating the copper block and measuring the relevant parameters. The cartridge heaters inserted in the copper block are connected to a power supply to provide the desired heat input. Each heater is connected to a 2A/250V fuse in series, and all the heaters are connected in parallel and the voltage across is measured. A shunt resistor connected in series with the system provides the current reading as shown in Figure B.2, which thus provides the heat input to the test block as shown in Eq (B.16)

$$P_{in} = \frac{V_s}{R_s} \times V_h \tag{B.16}$$

Here, V_h is the voltage across the heater, while V_s and R_s are the voltage and resistance of the shunt resistor (R_s = 0.01 Ω).

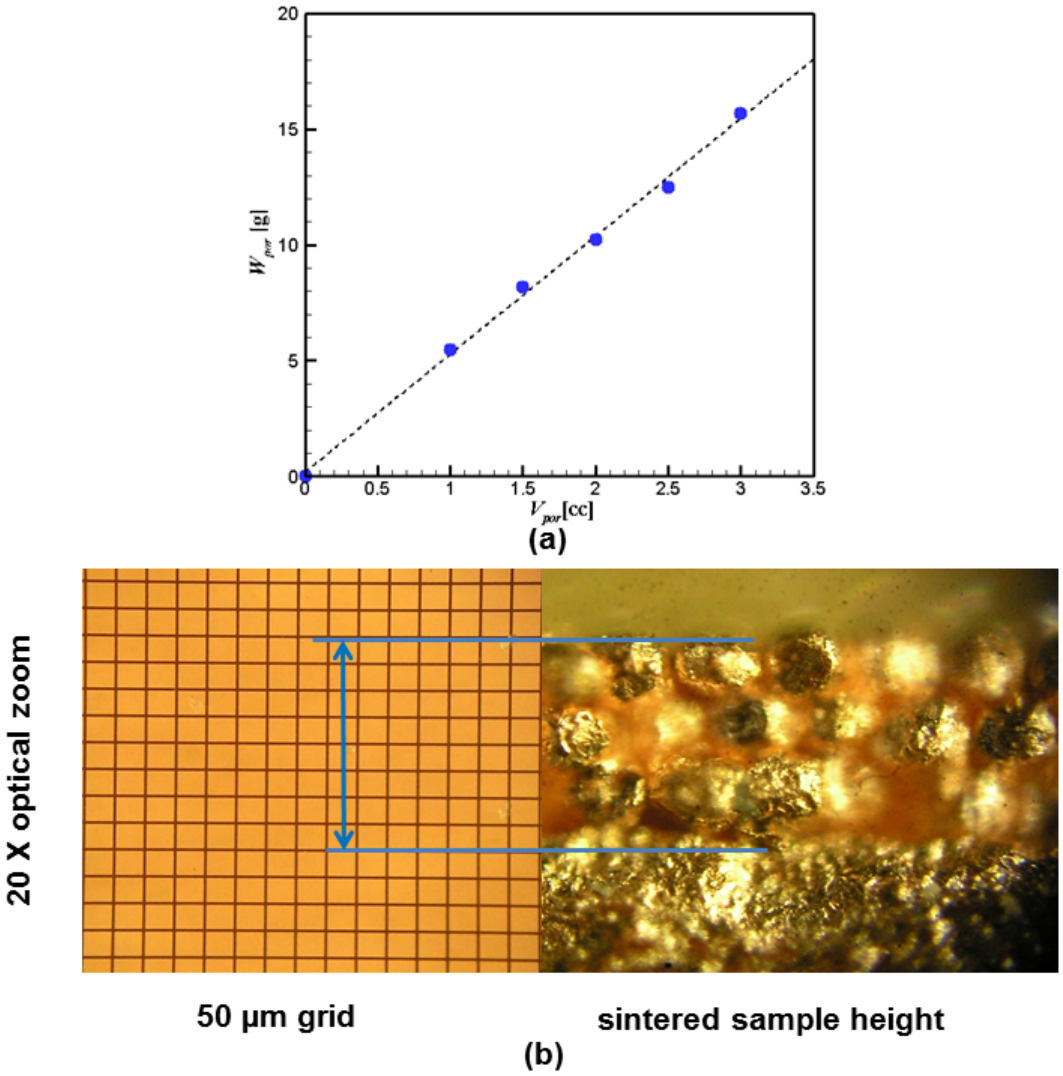

Figure B.1. Porosity calculation for (a) free-particle coating by density calculation from weight-volume measurements and (b) sintered-particle coating by calculation of height for volume and hence density measurement.

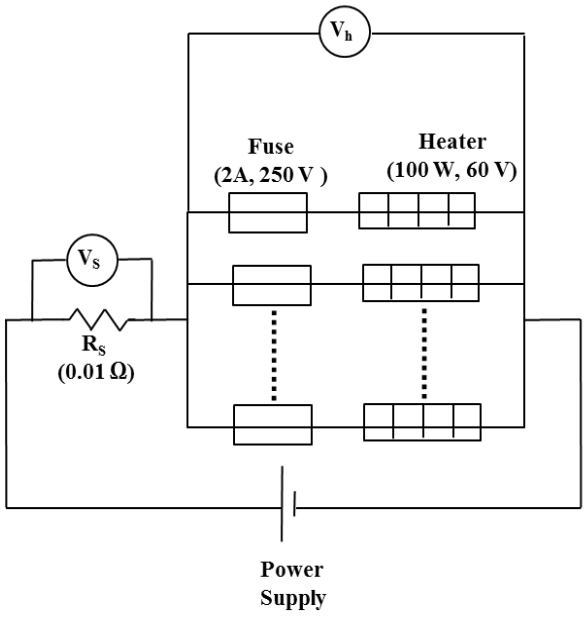

Figure B.2. Schematic diagram of the electrical circuit for power input to the heater block.

APPENDIX C. FABRICATION OF SINTERED PARTICLE COATINGS

This appendix provides a detailed description of the method of fabrication of sintered particle coatings for the pool boiling heat transfer experiments.

C.1 Preparation of Test Block and Particles

To prepare the copper block for direct testing or sintering, a smooth finish on the copper is first achieved with a standardized smoothing procedure. The larger-scale roughness on the surface, resulting from the manufacturing process, is first removed by polishing with rough sandpaper of 16 μm (600 grit) in circular motion for ~30 s, followed 9 μm (1000 grit) microfinish diamond sheet for 1 min. Further smoothing is achieved by polishing with 3 μm (1500 grit) and 0.1 μm (2500 grit) microfinish sheets for 2 min each. For removal of any residual material and to achieve a mirror-smooth finish, Happich Simichrome polish is applied to the surface with a soft touch cotton pad. The copper block is then rinsed with acetone, followed by methanol. This procedure results in a mirror-finish surface with roughness R_{RMS} = 20 nm, as measured by a non-contact 3D scanning white light interferometer (NewView 6200, Zygo Corp.). The copper particles used for testing are first sieved into the desired size range, and then cleaned by soaking in acetone, followed by a methanol rinse.

C.2 Sintering Procedure

To produce the sintered-particle coatings with reduced porosity, a graphite mold is fabricated, as shown in Figure C.1 (a). The mold dimensions are 1.1875" x 1.1875" x 0.020", with a .093" radius in each corner. The thickness of the coating required and the native packing density of the particles determine the depth of the groove cut in the mold. To fabricate a sintered sample, loose copper powder is poured into the groove in the graphite mold and leveled off to the desired height with a straight edge. The copper substrate is then gently placed on top of the copper powder. The mold, with the copper substrate, is placed into a Watlow bell jar heater (120 V/650 W) ceramic fiber furnace with ceramic end plugs, as shown in Figure C.1 (b) and (c). The ceramic end plugs hold the block and particles in place, and provide additional top weight to facilitate the sintering process. The assembly is evacuated down to ~10^{-2} torr (~1.33 Pa) over 4 hours using a mechanical pump, after which a diffusion pump is turned on to pull a high vacuum of ~10^{-6} torr (~1.33×10^{-4} Pa) over approximately 12 hours. The temperature is steadily ramped for 2.5 hours up to 950 °C as shown in Figure C.2 (a) and held at this temperature for the desired time under vacuum conditions of ~9.8×10^{-5} torr (~0.01 Pa). The time required for regular sintering is ~1 h for most cases. Coatings with largest particle size of 850-1000 μm used in Chapter 3, and coatings with lowest porosity in Chapter 4 (spherical at 39% and irregular at 51%) require higher sintering time of ~2 h at 950 °C. During the process of ramping up the temperature, there might be some loss of vacuum pressure, due to outgassing. The furnace power supply is then turned off. The assembly is allowed to cool gradually to room temperature under vacuum (~5.5×10^{-5} torr or 0.007 Pa) so as to avoid oxidation, and immediately placed in an airtight container

until it is tested. The cool-down time shown in Figure C.2 is an approximate estimate and may vary for each individual sample.

For fabricating the sintered particle coatings with increased porosity, the Lost Carbonate sintering method is used, as described in Chapter 4. The potassium carbonate powder (Sigma-Aldrich) is first ground and sieved to filter 90-150 μm carbonate particles. The copper particles (90-106 μm) are mixed with potassium carbonate particles (90-150 μm), with a weight ratio as shown in Table 4.1 to achieve the desired porosity. A small amount of ethanol is added to act as a binder in the mold, and the particles are mechanically stirred to ensure uniform mixing. This mixture is then poured into the mold to the desired height, and placed in the evacuated furnace, as described above. The temperature of the furnace is steadily ramped up to 850 °C and then held for ~2 hr to initiate the sintering process, as shown in Figure C.2. The temperature is then ramped up to 950 °C for ~30 min to decompose the carbonate particles (melting point of 891 °C), leaving behind open pores. The assembly is then allowed to cool gradually. This sintering recipe was selected because it has been shown to produce a clean and well-bonded porous structure for the desired porosity range, and does not require any post-processing to remove the potassium carbonate from the sintered matrix.

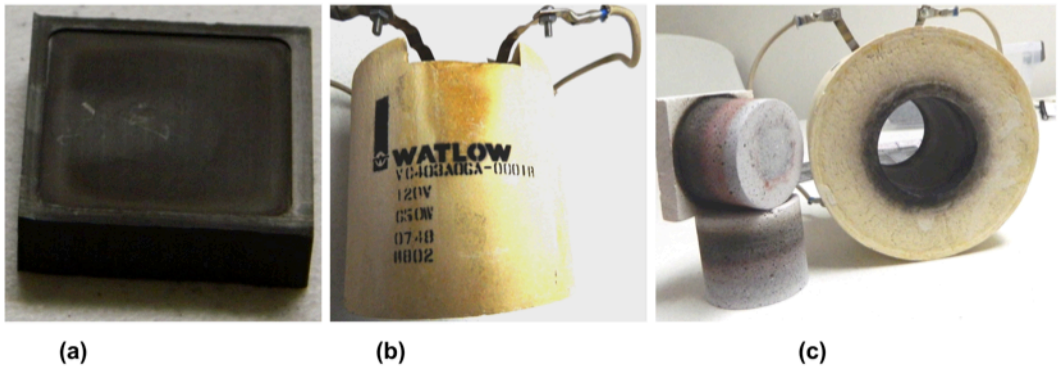

Figure C.1. Components used for sintering copper blocks, showing: (a) graphite mold (b) bell jar heater furnace and (c) ceramic end plugs for furnace.

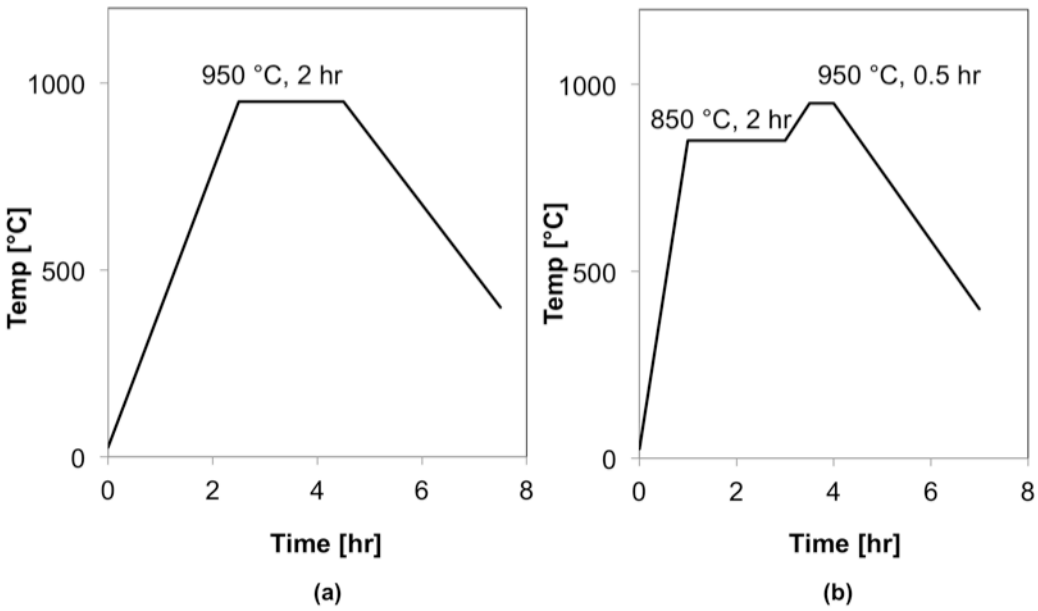

Figure C.2. Temperature ramps for (a) regular sintering and (b) lost carbonate sintering processes.

APPENDIX D. UNCERTAINTY ANALYSIS FOR TEMPERATURE AND HEAT FLUX MEASUREMENTS

This appendix provides a detailed description of the uncertainty analysis for the temperature and heat flux measurements presented in Section 3.1.3. Ice-point referenced T-type thermocouples were used for all heater block temperature measurements, and were calibrated using a temperature calibrator bath. For calibration, the sensing junction was placed in the bath, which was allowed to reach a steady-state temperature over a calibration range of 40 °C to 110 °C at intervals of 10 °C, as monitored by an auxiliary RTD. The ice-point reference junction was placed in a dry-block calibrator set to a constant 0 °C, also monitored using an RTD. A least-squares linear regression fit offset from the NIST ITS-90 [52] higher-order polynomial T-type thermocouple standard calibration curve was used to obtain a new calibration for the thermocouples, as given by

$$\Delta T_{TC,new} = m_1 \Delta T_{ITS-90} + b_1 \tag{D.1}$$

Here, $\Delta T_{TC,new}$ is the temperature differential of the bath measured by an RTD, and ΔT_{ITS-90} is the temperature differential calculated by the standard calibration curve with a 0 °C reference junction temperature, while m_1 and b_1 are the slope and intercept of the linear offset of $\Delta T_{TC,new}$ from ΔT_{ITS-90}. The calibration curve for the ITS-90 reference is represented by:

$$\Delta T_{ITS-90} = c_0 + c_1 \Delta V + (higher\ order\ terms) \tag{D.2}$$

where any offset from 0 °C in the ice-point reference junction temperature T_0 is measured and accounted for as

$$\Delta T_{TC,new} = T_{TC,new} - T_0 \tag{D.3}$$

In these equations ΔV is the voltage difference measured by the thermocouples, T_0 is the ice-point reference junction temperature, $T_{TC,new}$ is the new temperature assigned to the thermocouple, and c_0 and c_1 are constants specified in [52]. Substituting Equations D.1 and (D.2) into Eq (D.3), and neglecting the higher-order terms for uncertainty estimation, yields

$$T_{TC,new} = T_0 + m_1\left(c_0 + c_1 \Delta V\right) + b_1 \tag{D.4}$$

where the constants can be combined to obtain the thermocouple temperature calibration as

$$T_{TC,new} = T_0 + m\Delta V + b \tag{D.5}$$

where m and b and the slope and intercept of the $\Delta T_{TC,new}$ versus ΔV graph. The uncertainties in the measured quantities can be obtained by standard deviation based error propagation method as follows:

$$U_{TC,new} = \sqrt{U_{T_0}^2 + \left(\Delta V\ U_m\right)^2 + \left(mU_{\Delta V}\right)^2 + U_b^2} \tag{D.6}$$

where the uncertainties in the linear fit parameters are obtained according to Brown *et al.* [53] as given by Eq (D.7) and the root temperature uncertainties are given by Eq (D.8).

$$U_{m_a}^2 = \frac{NU_T^2}{N\sum V^2 - \left(\sum V\right)^2}; U_{c_a}^2 = \frac{U_T^2 \sum V^2}{N\sum V^2 - \left(\sum V\right)^2} \tag{D.7}$$

$$U_{T_0}^2 = U_{T_{ice}}^2 + U_{T_{RTD}}^2; U_T^2 = U_{T_{bath}}^2 + U_{T_{RTD}}^2 \tag{D.8}$$

Absolute temperature uncertainties $U_{T,ice}$ = ±0.1 °C, $U_{T,RTD}$ = ±0.1 °C and $U_{T,bath}$ = ±0.05 °C, are specified by the equipment manufacturers. This results in an absolute temperature uncertainty of ±0.23 °C. For differential temperature measurements, on account of simultaneous calibration of all thermocouples, the reduced propagated uncertainty is ±0.06 °C per the uncertainty in calibration slope, as described in [54]. Figure D.1 (a) shows a representative plot of the temperature measured by the thermocouples along the copper heated block, as a function of time. The temperature increases until the incipience of nucleate boiling, as shown during the initial time period. Thereafter, the temperature gradually reaches equilibrium and at steady state, the temperature is averaged over 40 readings. The uncertainty associated with this time-averaging as obtained from the standard deviation [104] is given by Eq (D.9). This uncertainty is calculated to be on the order of 0.002 °C and may be neglected.

$$T_{TC} = \overline{T} = \frac{\sum T_i}{N}; \sigma_s = \sqrt{\frac{1}{N-1}\sum \left(T_i - \overline{T}\right)^2}; U_{T_{TC}} = 2\frac{\sigma_s}{\sqrt{N}} \tag{D.9}$$

Figure D.1 (b) shows a plot of the temperature gradient within the heater block using the average steady state data. The temperature profile, as expected, is fairly linear and the heat flux is obtained from a linear fit to the temperature rake data; the uncertainties in the linear fit by a least-squares regression are obtained as described in [53], and the uncertainties in heat flux and temperature are calculated as given by Eq (D.10-D.12):

$$m = \frac{N\sum x_i y_i - \sum x_i \sum y_i}{N\sum (x_i)^2 - \left(\sum x_i\right)^2},\ b = \frac{\sum (x_i)^2 \sum y_i - \sum x_i \sum x_i y_i}{N\sum (x_i)^2 - \left(\sum x_i\right)^2} \tag{D.10}$$

$$\begin{aligned} U_m^2 &= \sum \left(\frac{\partial m}{\partial T_i}\right)^2 U_{T_i}^2 + \sum \left(\frac{\partial m}{\partial x_i}\right)^2 U_{x_i}^2 = U_{q"}^2 \\ U_b^2 &= \sum \left(\frac{\partial b}{\partial T_i}\right)^2 U_{T_i}^2 + \sum \left(\frac{\partial b}{\partial x_i}\right)^2 U_{x_i}^2 \end{aligned} \tag{D.11}$$

$$\begin{aligned} \left(\frac{\partial m}{\partial x_i}\right) &= \frac{NT_i - \sum T_i}{N\sum x_i^2 - \left(\sum x_i\right)^2} - \frac{\left(N\sum x_i T_i - \sum x_i \sum T_i\right)\left(2Nx_i - 2\sum x_i\right)}{\left(N\sum x_i^2 - \left(\sum x_i\right)^2\right)^2} \\ \left(\frac{\partial b}{\partial x_i}\right) &= \frac{2x_i \sum T_i - \sum x_i T_i - T_i \sum x_i}{N\sum x_i^2 - \left(\sum x_i\right)^2} - \frac{\left(\sum x_i{}^2 \sum T_i - \sum x_i \sum x_i T_i\right)\left(2Nx_i - 2\sum x_i\right)}{\left(N\sum x_i^2 - \left(\sum x_i\right)^2\right)^2} \\ \left(\frac{\partial m}{\partial T_i}\right) &= \frac{Nx_i - \sum x_i}{N\sum x_i^2 - \left(\sum x_i\right)^2};\left(\frac{\partial b}{\partial T_i}\right) = \frac{\sum x_i{}^2 - x_i \sum x_i}{N\sum x_i^2 - \left(\sum x_i\right)^2} \end{aligned} \tag{D.12}$$

The linear-fit data from the central and side rakes are then area-averaged to obtain the heat flux and extrapolated surface temperature. The wall surface temperature from each rake is measured by extrapolating the slopes of the temperature rakes, and the uncertainty is given by

$$U_{T_s}^2 = U_{T_0}^2 + U_{q"}^2 \left(\frac{\Delta x}{k_{Cu}}\right)^2 + U_x^2 \left(\frac{q"}{k_{Cu}}\right)^2 \tag{D.13}$$

The uncertainties associated with area-averaging of the heat flux and surface temperature are given by

$$U_{q''}^2 = \left(\frac{A_c}{A_{tot}} U_{q_c''}\right)^2 + \left(\frac{A_a}{A_{tot}} U_{q_a''}\right)^2 + \left(\frac{A_b}{A_{tot}} U_{q_b''}\right)^2$$
$$U_{T_w}^2 = \left(\frac{A_c}{A_{tot}} U_{(T_w)_c}\right)^2 + \left(\frac{A_a}{A_{tot}} U_{(T_w)_a}\right)^2 + \left(\frac{A_b}{A_{tot}} U_{(T_w)_b}\right)^2 \quad \text{(D.14)}$$

For these uncertainty calculations, the random uncertainty in one temperature reading is assumed to be ±0.23 °C for absolute temperature and ±0.06 °C for temperature differential, while the systematic uncertainty of temperature readings is assumed to be zero. Since the thermocouple locations are fixed, the random uncertainty in the axial location is assumed to be zero, while the systematic uncertainty U_x is taken as the maximum clearance between the thermocouple bead diameter and the diameter of the tapped holes in the copper block, 40 μm. The uncertainty in location and temperature of each thermocouple is assumed to be independent of the location and reading of other thermocouples. The uncertainties in areas are assumed to be zero.

Following the analysis described above, the uncertainty in area-averaged surface temperature and heat flux are respectively calculated to be ±0.1 °C and ±4.5 kW/m^2 over the range of heat fluxes investigated.

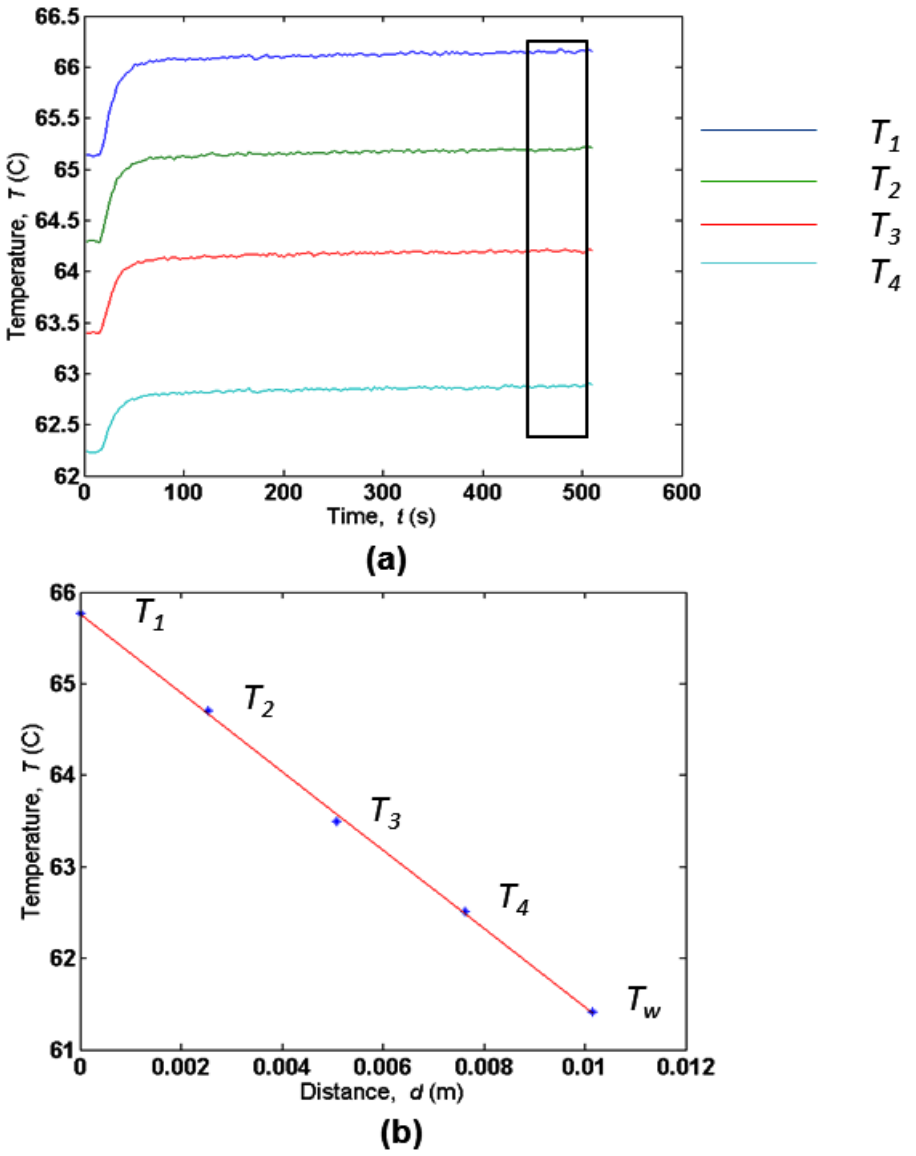

Figure D.1. Representative plots of (a) transient thermocouple temperature measurements and (b) linear fit to average steady state temperature; along the central thermocouple rake of the heater block.

APPENDIX E. POOL BOILING HEAT TRANSFER FROM DEFORMABLE PARTICULATE BEDS

This appendix provides additional images from flow visualization of boiling from free-particle coatings. The material presented in this appendix was published as a photo gallery submission in *Journal of Heat Transfer* [55].

Pool boiling heat transfer is measured from a particulate bed of loose copper particles that are able to freely move on the polished copper surface beneath. The working fluid is FC-72. High-speed microscopic flow visualization at 3000 frames per second (Ultima APX, Photron) enables observation of vapor-particle interactions (VH-Z50L, Keyence). Figure E.1 shows a vapor bubble breaking through the top layer of the loose particle bed, at a heat flux of 4.0 kW/m^2. Particles in its path are displaced and ejected into the liquid. The vapor bubble subsequently detaches from the bed and rises into the fluid. As the heat flux is further increased to 5.9 kW/m^2, stable vapor columns are formed within the particle layer. The free particle layer deforms to allow vapor departure from the surface, which would otherwise be restricted. After the vapor bubble displaces the particles and departs, the suspended particles settle down back into the particle bed. Free particle beds of 98, 196, and 925 μm average particle diameter are directly compared to a baseline polished surface with average roughness < 0.1 μm (top), as discussed in Chapter 3. Layer thickness to particle diameter ratio is held constant. The largest particle size initially improves nucleate boiling performance, but bed deformation is not observed, and

critical heat flux is reduced due to vapor trapping in the porous layer. In comparison, the smaller free particles retain nucleate boiling enhancement, but particles in the path of vapor departing from the surface are displaced and ejected into the liquid (middle). Visualizations confirm that passive deformation of the loose particulate bed eases vapor escape from the surface (bottom), enabling a 32% reduction in surface superheat up to the same critical heat flux as measured for the polished surface.

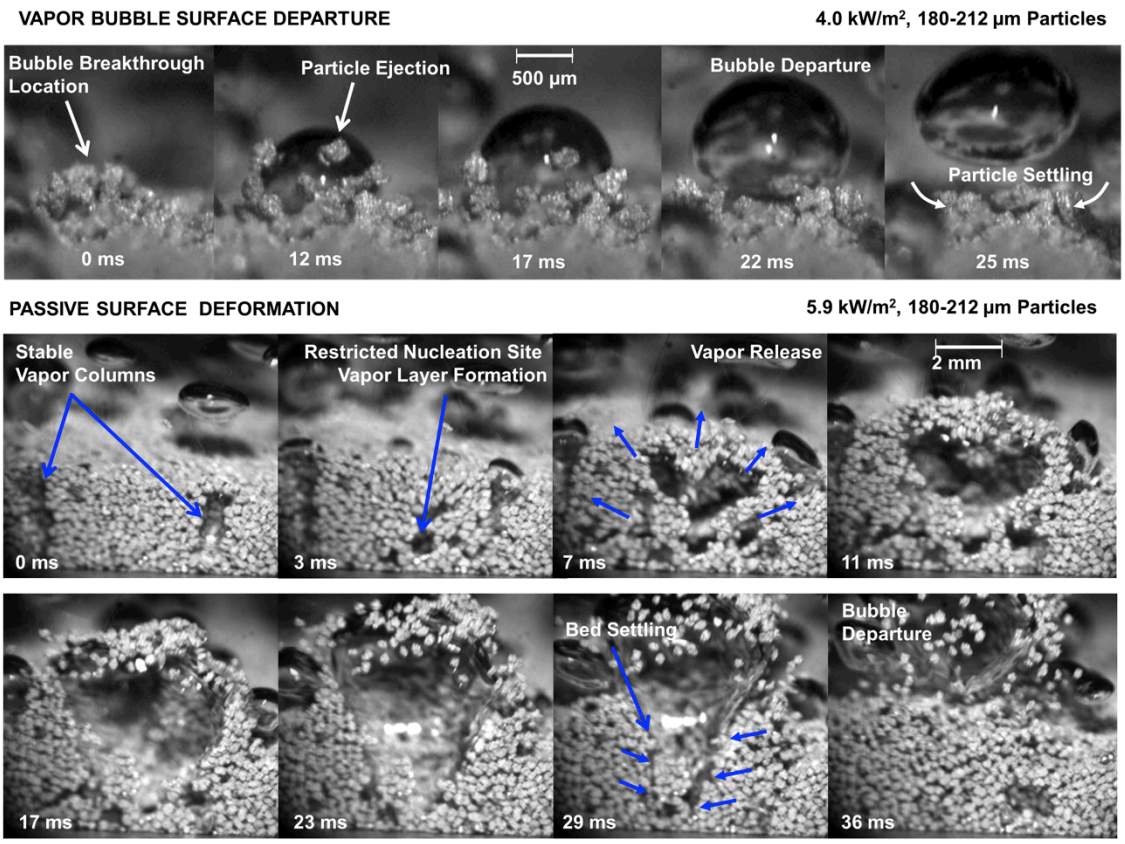

Figure E.1. Flow visualization images during pool boiling from free-particle coatings with 180-212 µm particles. The departure of vapor bubble by passive surface deformation is demonstrated.

APPENDIX F. EFFECT OF PARTICLE MORPHOLOGY ON POOL BOILING FROM SURFACES COATED WITH SINTERED PARTICLES

This appendix provides a summary of an experimental investigation of effects of particle morphology on pool boiling from surfaces with sintered particles. While most of the results are discussed in Chapter 4, some additional tests conducted during this study are presented here. The detailed description of the material presented in this appendix was presented at *International Mechanical Engineering Congress and Exposition 2015*, and is published in [105].

F.1 Fabrication of Test Surfaces

To study the effect of particle morphology on the pool boiling performance, three different kinds of copper particles were used, *viz.*, irregular, dendritic and spherical. The differences in morphology are brought about by the particle fabrication method. Irregular particles are produced by water atomization, dendritic particles are produced by electrolysis, and spherical particles by air atomization. Irregular particles appear as roughened spheroidal shapes, dendritic particles are elongated rod-like structures with rough branches, while spherical particles are smooth and uniformly rounded. Figure F.1 shows representative images of the particle shapes observed using a scanning electron microscope (SEM). Due to the different morphology of the particles, the native packing porosity before sintering varies widely from ~40% to ~70%, as shown in Table F.1. In

order to isolate the effect of particle morphology, the sintered-coating fabrication methods are devised so as to arrive at the same sintered layer porosity (~60%) and coating thickness (~6 particle diameters) for each particle shape. This requires either reducing or increasing the native packing density of the powder, by methods described in Chapter 4.

F.2 Results and Discussion

For porous coatings formed from particles of the same size (90-106 μm) and porosity (~60%), each particle morphology creates pores of unique shapes, thereby leading to differences in the boiling heat transfer performance. Figure F.2 shows the boiling curves obtained for the irregular, dendritic and spherical particle coatings described in Table F.1. Boiling curves for each test piece are obtained in two separate tests to ensure repeatability, as shown in Figure F.2. The two tests for each coating do not show any significant deviation, demonstrating that vigorous boiling leading to CHF in the first test does not degrade the coating performance in the second test. Tests performed for each sample with the heat flux being reduced in steps (not shown in the graph) did not point to any hysteresis in the results.

Compared to a polished surface [50], these sintered surfaces show boiling incipience wall superheat ~80 times lower, heat transfer coefficients ~15-25 times higher and CHF ~2 times higher. At very low heat fluxes (below ~7 kW/m^2), natural convection heat transfer occurs (not shown in the graph). As the heat flux is increased, nucleate boiling incipience occurs at very low wall superheat (<0.4 K). With further increase in heat flux,

the wall superheat consistently increases. The heat transfer coefficient, as shown in Figure F.3, is a function of the wall superheat at any given heat flux, as is typically observed for pool boiling studies, although the exact variation depends on the morphology.

Comparing the boiling curves for the different morphologies, it is observed that boiling incipience occurs for all of the different coatings at a low superheat (0.07 K to 0.34 K) and a heat flux of ~7 kW/m^2; differences between the incipience behaviors of the coatings are within the margin of measurement error. As the heat flux is increased, the wall superheat increases beyond the point of incipience. For a spherical particle coating, the heat transfer coefficient increases as the heat flux increases for low heat flux values, and approaches a more or less constant value (indicated by the relatively constant slope of the boiling curve). However, for the irregular and dendritic coatings, the heat transfer coefficient increases at a faster rate than spherical coatings after incipience, reaches a maximum value and then decreases at higher heat fluxes (indicated by the increasing and then decreasing slope of the boiling curve). The irregular particle coating is observed to show the best heat transfer performance throughout the boiling curve (*i.e.*, a lower superheat at a given heat flux, implying a higher heat transfer coefficient). The spherical particles, on the other hand, yield the lowest heat transfer coefficients throughout the range of heat fluxes after boiling incipience. The trends in boiling performance are analyzed in light of the morphology of the sintered particle coatings revealed by the SEM images in Figure F.4.

It is observed from Figure F.4 that the structure of the open pores and the particle packing arrangement in the sintered coatings strongly depend on the particle morphology.

The pores in the irregular and dendritic particle coatings qualitatively appear smaller and more tortuous than for the spherical particles. Larger pores at the same porosity may also be indicative of lesser surface area between the flooded liquid phase and copper particles, as well as reduced contact between individual copper particles, thereby reducing the effective thermal conductivity of the coating. It can also be noted here that the spherical particles have a notably smoother surface compared to the roughness displayed by both the irregular and dendritic particles. This inherent surface roughness likely leads to an enhancement of the interstitial surface area available for heat transport during boiling at a constant porosity. The heat transfer performance of the coatings above a heat flux of ~20 kW/m^2 is consistent with these qualitative observations regarding the pore size and surface roughness; both irregular and dendritic particles have a higher heat transfer coefficient than spherical particles.

The pore structure may also explain the observed change in slope of the boiling curve for the different morphologies. As the heat flux is increased following incipience, the heat transfer coefficient increases as more nucleation sites become active. For irregular and dendritic particles, this increase is only observed up to an intermediate heat flux (~120 kW/m^2 and ~90 kW/m^2, respectively), after which, further increases in heat flux reduce the heat transfer coefficient (Figure F.3). This behavior may be attributed to inefficient vapor escape and liquid replenishment through these coatings, compared to the more open pores in spherical coatings.

Figure F.5 shows flow visualization images for the irregular-particle coating for heat fluxes increasing from a low value of 18 kW/m^2 to an intermediate heat flux of 68 kW/m^2 and up to a high heat flux of 185 kW/m^2. As the heat flux is increased from low to

moderate values, small bubbles near the surface coalesce into larger bubbles before departure. A similar trend in the bubble departure process with heat flux is observed for all the particle shapes. No clear qualitative differences in the flow behavior were observed across the different coatings. The irregular, dendritic and spherical particle coatings reach similar values of CHF at 224 kW/m^2, 209 kW/m^2, and 229 kW/m^2, respectively. The particle morphology thus appears not to have a significant effect on the CHF. The slightly lower CHF for dendritic particle coatings may be attributed to the slightly larger thickness of the coating that results from a slight variation during the fabrication of the coatings. Previous studies [11, 57] have shown that for surfaces of similar wettability and other coating characteristics, the porosity of the coating determines the CHF during boiling. Li and Peterson [57] also showed that for coatings with similar porosity, CHF increases with an increase in coating thickness. Since both the coating thickness and porosity for all three coatings are similar in the present study, the CHF is expected to be comparable in value, as observed.

F.3 Conclusions

Pool boiling heat transfer performance is investigated from porous coatings formed by sintering three different copper particle morphologies, *viz.* irregular, dendritic and spherical, for particle sizes of 90-106 μm and a coating porosity of ~60%. The boiling heat transfer performance for the coatings is observed to be strongly dependent on the observed differences in roughness of the particles and the structure of the interstitial pores formed. The irregular particles (produced by water atomization) show the largest

heat transfer coefficient along the boiling curve, while the spherical particles (produced by air atomization) show the lowest heat transfer coefficient. The rough particle surfaces and small pores for the irregular and dendritic coatings appear to enhance the boiling performance of these coatings. The maximum CHF is relatively insensitive to particle morphology and ranged from 209 kW/m^2 to 224 kW/m^2. Irregular-shaped particles thus provide the best boiling heat transfer performance. It may be concluded that the heat transfer coefficient of particles along the boiling curve strongly depends on the morphology of particles and pore structure of the coatings, while CHF is primarily independent of the particle morphology, but further characterization of the pore structure of the coatings is essential for these features to be quantitatively compared to the trends observed in the boiling heat transfer performance.

Table F.1. Measured porous coating parameters before and after sintering for the three different particle morphologies.

Particle Shape	Particle Size	Before Sintering	After Sintering	
		ε [%]	δ/d	ε [%]
Irregular	90-106 μm	65	5.8	58 ±1.1
Dendritic		69	6.2	60 ±2.0
Spherical		43	5.7	62 ±1.6

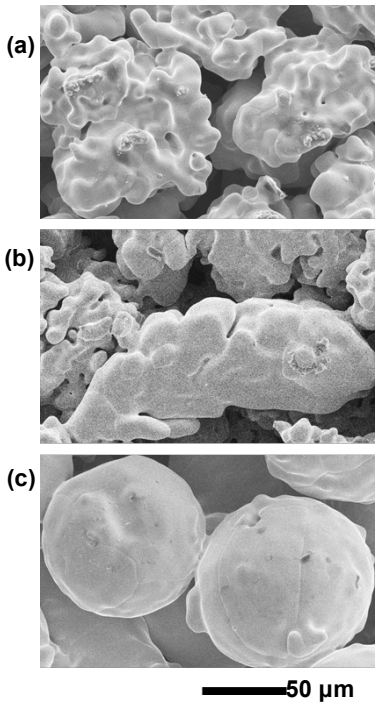

Figure F.1. SEM images of (a) irregular, (b) dendritic and (c) spherical particles after sintering.

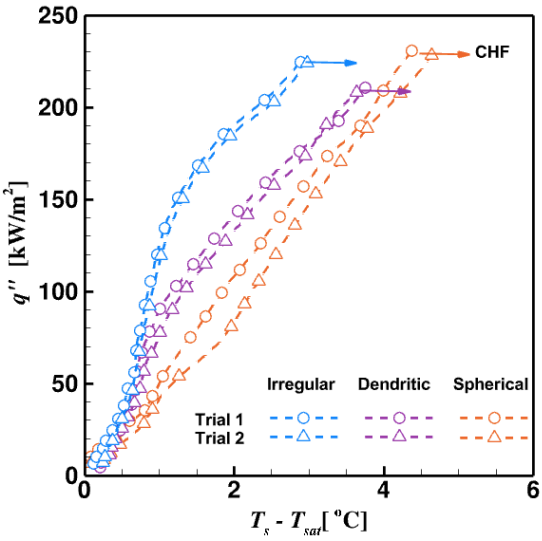

Figure F.2. Boiling curves of area-averaged heat flux versus wall superheat (T_s-T_{sat}) for each sintered particle morphology. CHF is indicated by horizontal arrows.

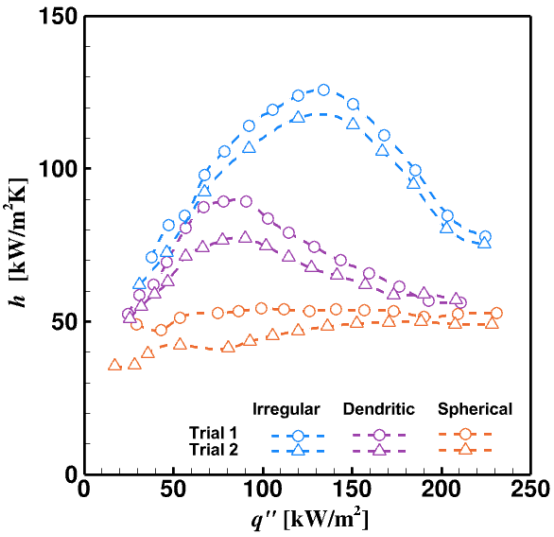

Figure F.3. Heat transfer coefficient for each sintered particle morphology.

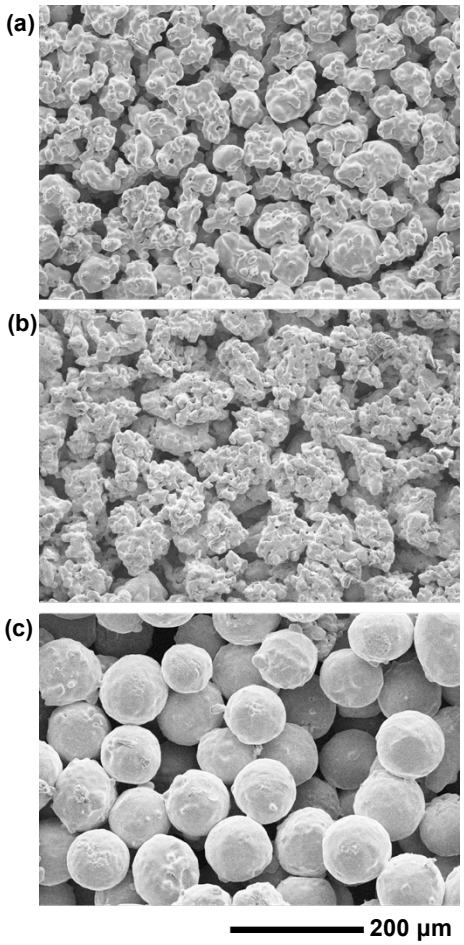

Figure F.4. Top-view SEM images of the sintered coating for (a) irregular, (b) dendritic and (c) spherical particles.

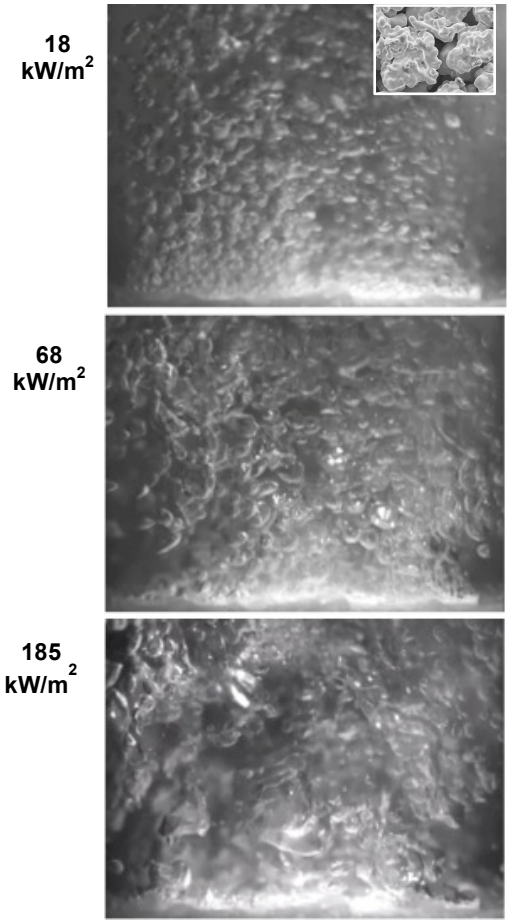

Figure F.5. Flow visualization of pool boiling from the irregular-particle sintered coating at different heat fluxes.

APPENDIX G. IMAGES AND DATA USED FOR POOL BOILING STUDY

This appendix provides additional images of the sintered coatings used in this study. Figure G.1 shows images of the irregular, dendritic and spherical particle coatings described in Appendix F, as observed under an optical microscope. Figure G.2 and Figure G.3 show optical microscope images of spherical and irregular particle coatings respectively, at different porosities, used for pool boiling experiments in Chapter 4. Figure G.4 and Figure G.5 show representative 2D image slices for the same spherical and irregular particle coatings respectively, obtained from μ-CT scans. Figure G.6 and Figure G.7 show the 3D reconstructed copper domain for the spherical and irregular coatings at different porosities, used for numerical simulations. This represents 7 pore diameter lengths, as described in Table 4.2. Figure G.8 shows the Nusselt number calculated for all the samples, based on three different length scales as described below:

$$Nu_{dpore} = \frac{h_{av} d_{pore}}{k_z}$$
$$Nu_{S\,\mathrm{int}} = \frac{h_{av}}{k_z S_{\mathrm{int}}} \qquad \text{(G.1)}$$
$$Nu_{Sneck} = \frac{h_{av}}{k_z S_{neck}}$$

Figure G.9 shows the variation of unit interfacial area with pore diameter for all the samples tested. S_{int} is observed to vary quadratically with d_{pore}.

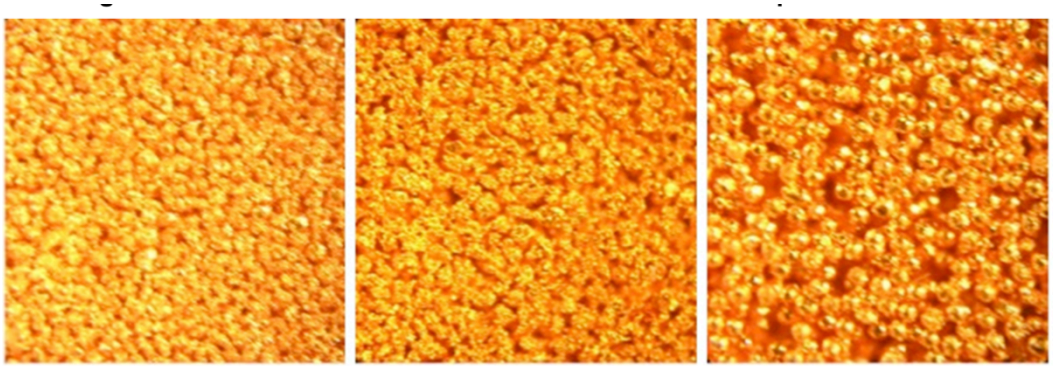

Figure G.1. Images of top surface of sintered (a) irregular (b) dendritic and (c) spherical particle coatings as seen under optical microscope at 10× magnification.

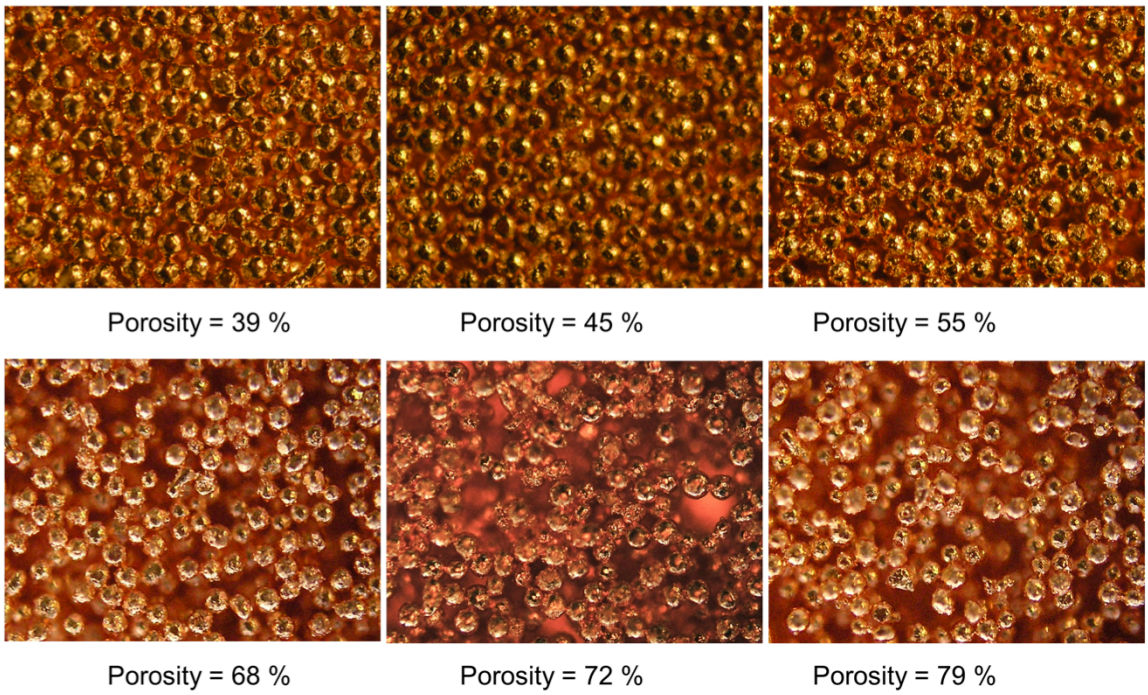

Figure G.2. Images of sintered spherical particle coatings at different porosities as seen under as seen under optical microscope at 10× magnification.

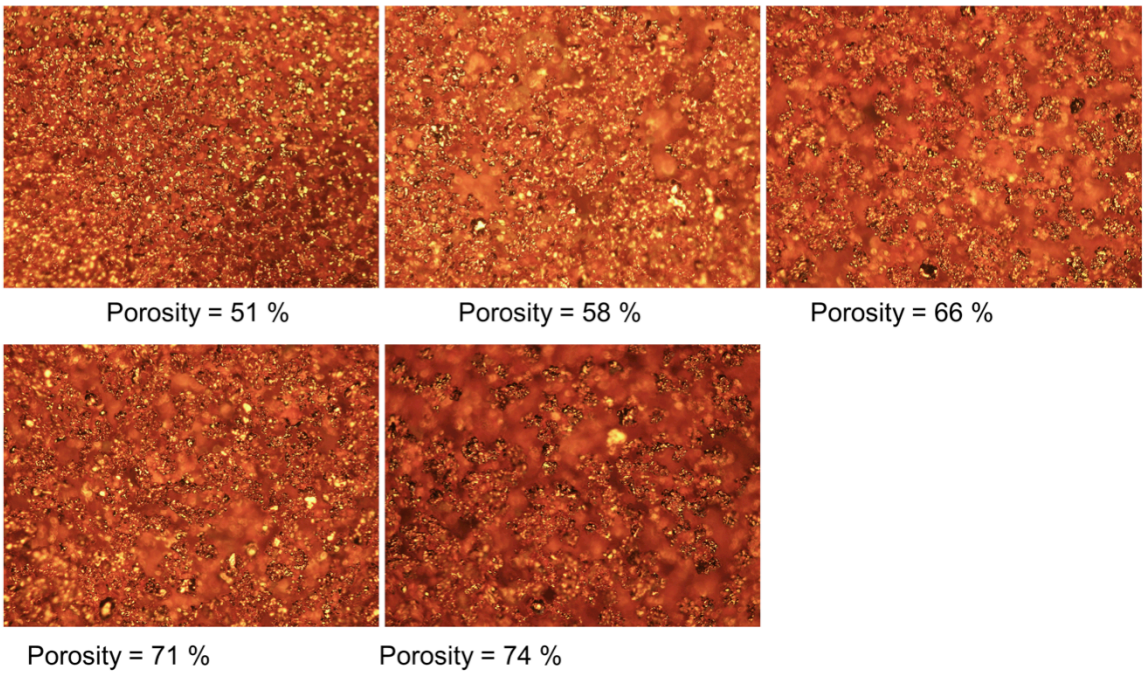

Figure G.3. Images of sintered irregular particle coatings at different porosities as seen under as seen under optical microscope at 10× magnification.

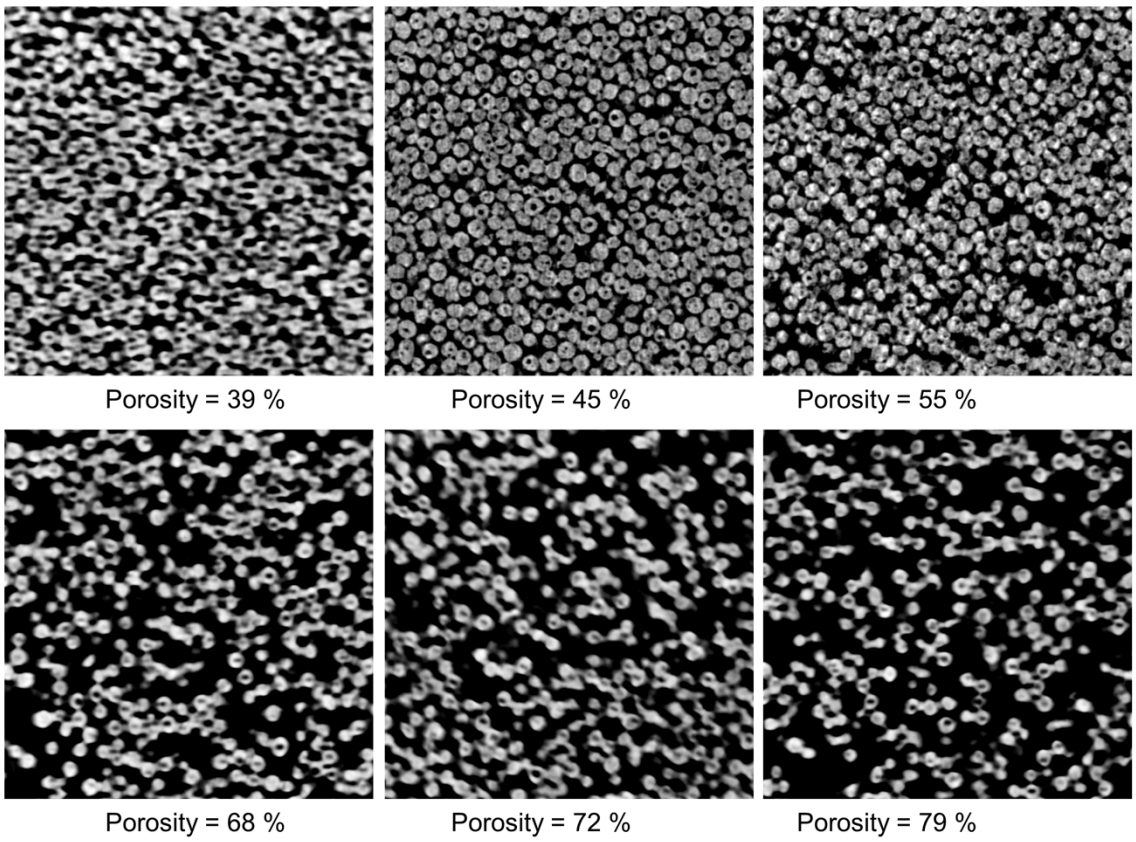

Figure G.4. Representative images of 2D slices from micro-CT scans of sintered spherical particle coatings at different porosities. Domain size is 2000 μm × 2000 μm.

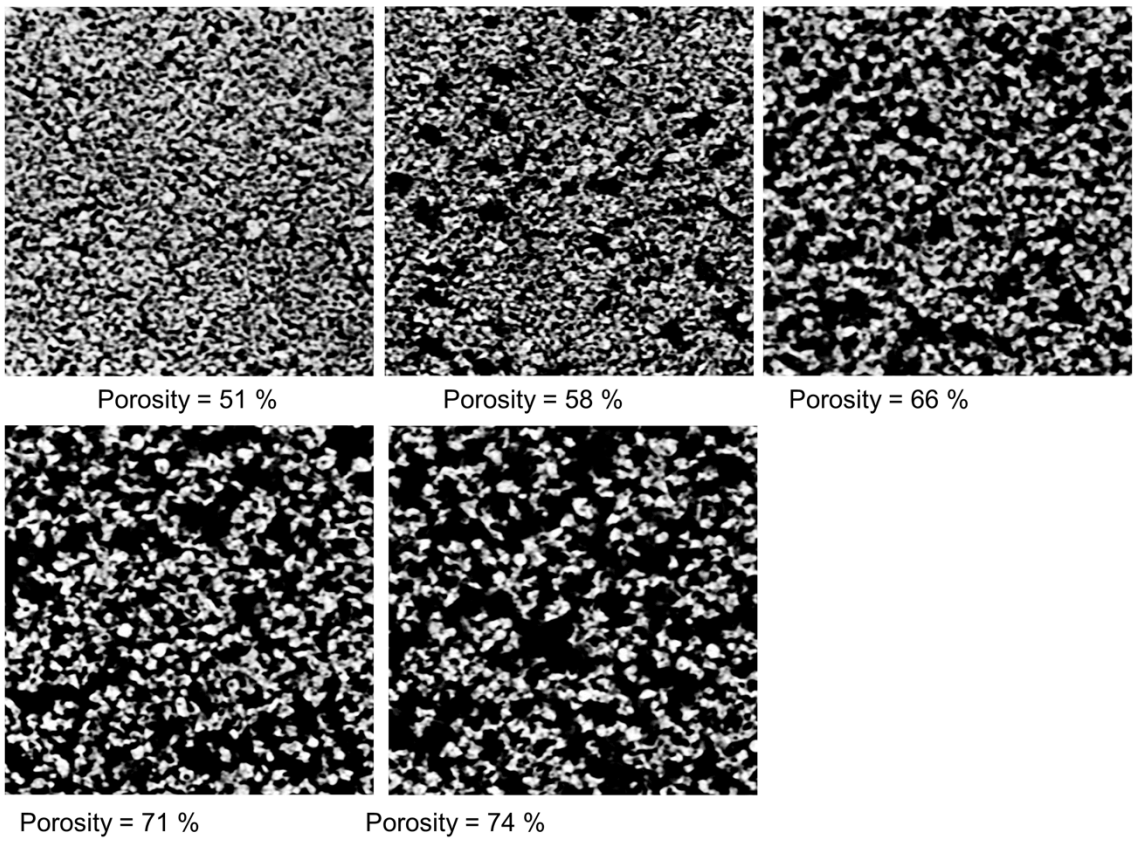

Figure G.5. Representative images of 2D slices from micro-CT scans of sintered spherical particle coatings at different porosities. Domain size is 2000 μm × 2000 μm.

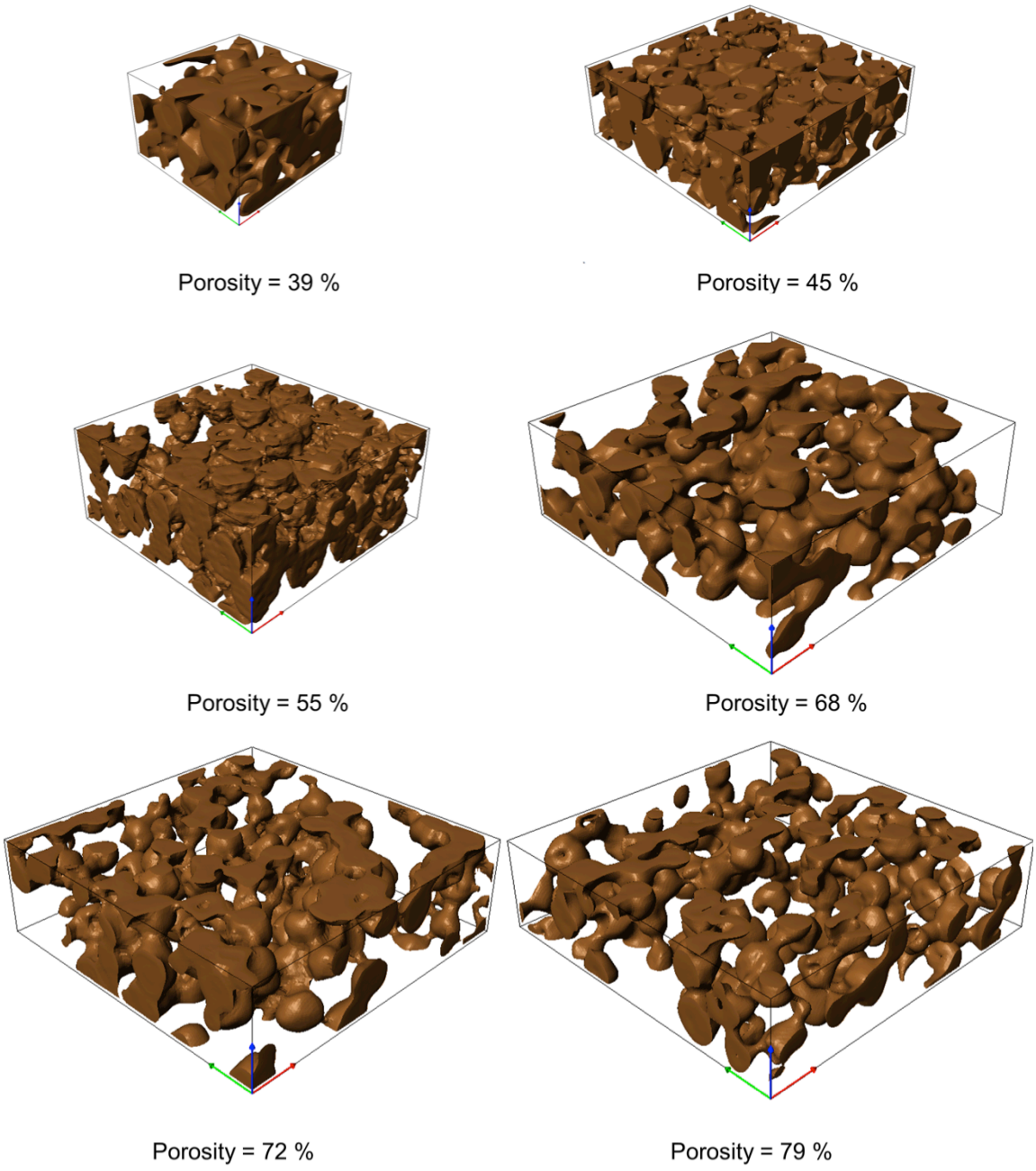

Figure G.6. Images of 3D reconstructed domains of spherical particle coatings at different porosities. The domain size shown represents seven pore lengths used for numerical simulations as shown in Table 4.2.

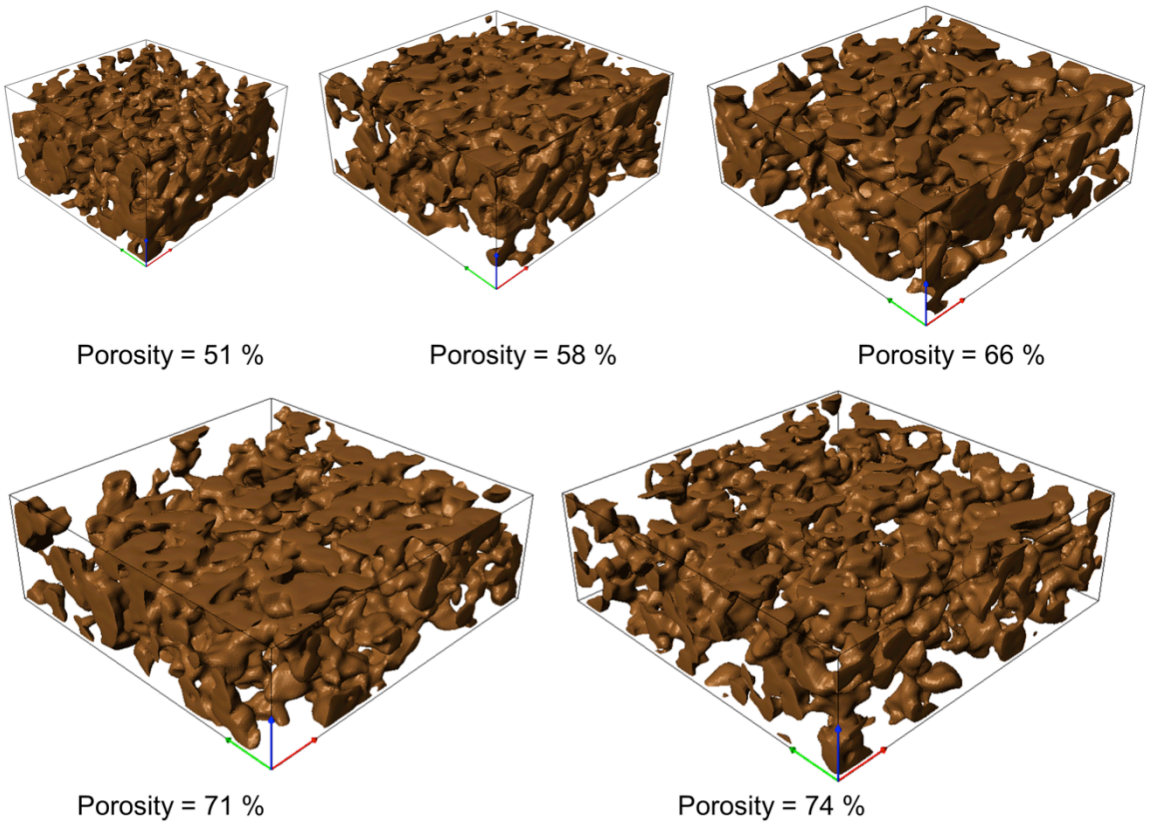

Figure G.7. Images of 3D reconstructed domains of irregular particle coatings at different porosities. The domain size shown represents seven pore lengths used for numerical simulations as shown in Table 4.2.

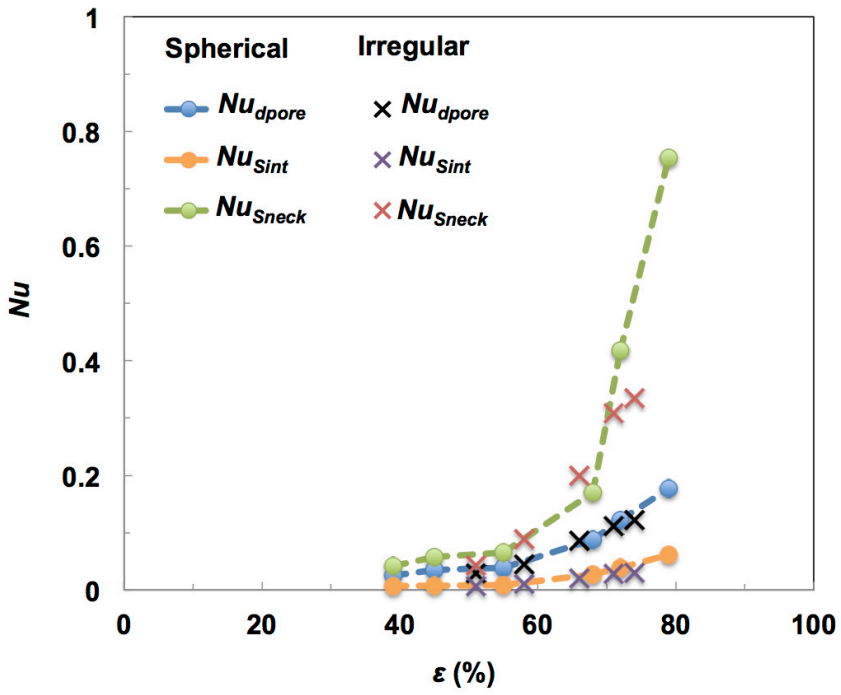

Figure G.8. Variation of Nusselt number with porosity for all spherical and irregular samples tested.

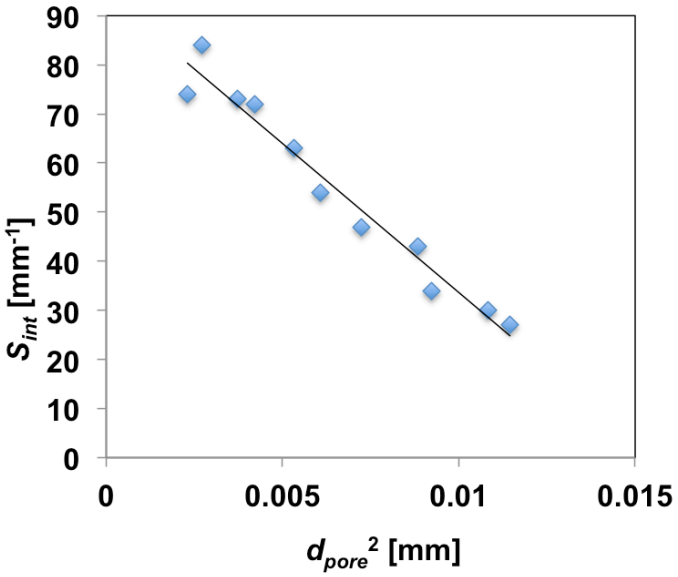

Figure G.9. Variation of unit interfacial area S_{int} with squared pore diameter d_{pore}^2 for all irregular and spherical samples tested.

APPENDIX H. LIST OF EQUIPMENT AND MAJOR COMPONENTS USED IN THE TEST FACILITY

This appendix provides a detailed list of equipment and components used in the experimental test setup, and in imaging. The author would like to thank Steve Titolo, Thermophysical Properties Research Lab (TPRL), for fabricating the components within the test facility. Components that are custom-made are indicated in the following table with TPRL under vendor or manufacturer column.

Table H.1. Equipment and major components of pool boiling test facility.

Part Name	Vendor or Manufacturer	Part Number	Description
Chiller	Neslab	ULT80	Low-temperature chilling unit for condensers
Aluminum helical condenser	McMaster-Carr	5177K62	Easy-bend aluminum tubing, 3/16" OD X 0.132" ID
Cartridge heaters	Watlow	C1A-9612	1/8" diameter, 12" lead, 100 W, 60 V cartridge heaters
Power supply	TDK-Lambda (Purdue ME E-shop)	TCR 40S15	40 V, 15 amp DC power supply
Thermocouple	Omega	TMTSS-032	T-type 0.032” sheathed thermocouple
Thermocouple calibration bath	Fluke	7103	Micro-bath calibrator, Range -30 °C to 200 °C

Table H.1. Continued.

Reference RTD	Omega	PR-11-2-100-1/8-6-E	4-wire reference probe for ice point
Ice point reference block	Omega	TRCIII	0 °C thermoelectric ice point, 6 probe
Data acquisition	Agilent	34970A	Analog data acquisition system
Copper alloy 101	McMaster-Carr	2554T1	Ultra conductive 1" thick copper sheet, for heater block
Copper particles 1	Alfa Aesar	42623	99.9% air-atomized spherical copper powder, 44-149 μm
Copper particles 2	Alfa Aesar	44213	99.5% air-atomized copper powder, 0.8-2 mm
Copper particles 3	ACuPowder	61 A	99% air-atomized copper shot, 105-250 μm
Copper particles 3	ACuPowder	264	99.3% water-atomized copper powder, <149 μm
Copper particles 4	ACuPowder	EL-240	99.8% electrolytic copper powder, >44 μm
Sieves 1	Hogentogler and Co. Inc.	1553, 1554, 1557, 1558, 1561	Brass sieves for screening particles of different size ranges
Sieves 2	Dual Mfg. Co. Inc.	US3-18B, US3-20B, US3-325B	Brass sieves for screening particles of different size ranges
Potassium carbonate	Sigma-Aldrich	P5833	Potassium carbonate powder for LCS
RTV	Momentive	118	Silicone sealant
Epoxy 1	3M	DP 190	Sealant for copper block, used with free particles
Epoxy 2	Elantas PDG	E 5302	High temperature paste epoxy, Epoxylite, used for sintered particles

Table H.1. Continued.

Polycarbonate gasket	McMaster-Carr	85585K17	0.03" thick impact-resistant smooth finish polycarbonate film
Pool components	TPRL	Polycarbonate walls, PEEK and ceramic insulation, aluminum and polycarbonate cover plates	Components used for constructing the pool in the pool boiling test setup

Table H.2. Optical Measurement Equipment.

Part Name	Vendor or Manufacturer	Part Number	Description
High-speed camera	Photron	FastCam Ultima APX	Megapixel camera for visualizations, 2000 fps at full resolution 1024 X 1024 resolution
Sunoptics Xenon light source	JBSMedical	TITAN 300HP	300W Xe arc lamp light source
Linear translation stage	Newport	443	Linear travel translation stage
Linear translation stage	Newport	TSX-1D	Dovetail linear stage
Angular stage	Newport	36	Tilt and rotation stage
Support rail mounts	Newport	UP-1A	Mounting plate for rails supporting test facility
SEM	Hitachi (Purdue Birck Nanotechnology Center labs)	S-4800	Ultra-high resolution scanning microscope

VITA

VITA

Suchismita Sarangi received a Bachelor of Technology in Mechanical Engineering from National Institute of Technology, Rourkela, India in 2008. Following her graduation, she pursued post-graduate studies and received a Master of Science in Mechanical Engineering from Pennsylvania State University in 2010, for her thesis entitled "Scaled Experiment on Gravity Driven Exchange Flow for the Very High Temperature Reactor". She is currently pursuing her PhD in the School of Mechanical Engineering at Purdue University under the advisement of Prof. Suresh V. Garimella. Her research interests include advanced electronics packaging, immersion cooling, nucleate boiling enhancement, boiling characterization, experimental and numerical methods in heat transfer.

Upon graduation from Purdue, she will join as a thermal engineer in the High Performance Computing Product Engineering team at Intel, Hillsboro, OR.

LIST OF PUBLICATIONS

LIST OF PUBLICATIONS

1 S. Sarangi, J. A. Weibel and S. V. Garimella, Quantitative dependence of pool boiling heat transfer enhancement on sintered-particle coating characteristics, Journal of Heat Transfer (in review).

2 S. Sarangi, J. A. Weibel and S. V. Garimella, Effect of particle morphology on pool boiling from surfaces coated with sintered particles, Proceedings of the ASME International Mechanical Engineering Congress and Exposition 8A (2015), Houston, Texas.

3 S. Sarangi, J. A. Weibel and S. V. Garimella, Effect of particle size on surface-coating enhancement of pool boiling heat transfer, International Journal of Heat and Mass Transfer 81 (2015) 103-113.

4 S. Sarangi, K. K. Bodla, S. V. Garimella and J. Y. Murthy, Manifold microchannel heat sink design using optimization under uncertainty, International Journal of Heat and Mass Transfer 69 (2014) 92-105.

5 J. A. Weibel, S. Sarangi and S. V. Garimella, Pool boiling heat transfer from deformable particulate beds, Journal of Heat Transfer Photogallery 135 (8) (2013).

6 S. Sarangi, K. K. Bodla, S. V. Garimella and J. Y. Murthy, Optimization under uncertainty of manifold microchannel heat sinks, Proceedings of the ASME International Mechanical Engineering Congress and Exposition 9 (2012), Houston, Texas.